Joint Parameters Estimation using FMCW UWB Waveform

Xu, Shengzhi

DOI
10.4233/uuid:f9ce79b1-7890-41b4-850b-134dcfbef52e

Publication date
2020

Document Version
Final published version

Citation (APA)
Xu, S. (2020). *Joint Parameters Estimation using FMCW UWB Waveform*. [Dissertation (TU Delft), Delft University of Technology]. https://doi.org/10.4233/uuid:f9ce79b1-7890-41b4-850b-134dcfbef52e

Joint Parameters Estimation using FMCW UWB Waveform

Joint Parameters Estimation using FMCW UWB Waveform

Dissertation

for the purpose of obtaining the degree of doctor
at Delft University of Technology,
by the authority of the Rector Magnificus, Prof. dr. ir. T.H.J.J. van der Hagen,
chair of the Board for Doctorates,
to be defended publicly on
Wednesday, 29 April 2020 at 15:00 o'clock

by

Shengzhi XU

Master of Science in Information and Communication Engineering,
National University of Defense Technology, Changsha, China,
born in Hefei, China.

This dissertation has been approved by the promotor

promotor: Prof. dr. A. G. Yarovoy

Composition of the doctoral committee:

Rector Magnificus,	chairperson
Prof. dr. A. G. Yarovoy,	Delft University of Technology

Independent members:

Prof. dr. ir. A. Stelzer	Johannes Kepler University Linz
Prof. dr. ir. F. M. J. Willems	Eindhoven University of Technology
Prof. dr. D. M. Gavrila	Delft University of Technology
Prof. dr. ir. G. J. T. Leus	Delft University of Technology
Prof. dr. ir. F. Le Chevalier	Delft University of Technology

This research was supported by the China Scholarship Council and the EEMCS faculty of Delft University of Technology.

ISBN 978-94-028-2035-5

An electronic version of this dissertation is available at
http://repository.tudelft.nl/.

To my family and friends

CONTENTS

SUMMARY

As one of the main sensor in autonomous driving, radar has great advantages over other sensors, especially its capabilities during adverse weather condition and Doppler information extraction.

Performance of the radar in terms of accuracy and target resolution strongly depends on radar waveforms transmitted and signal processing algorithms applied. To achieve high range resolution, an ultra-wideband (UWB) signal has to be used for sensing, which introduces difficulties to achieve high Doppler and direction-of-arrival (DOA) estimation simultaneously due to the range migration. To address this problem, in this thesis new signal processing algorithms are proposed, which pave the way to improved performance of the automotive radar sensor.

As the frequency-modulated continuous-wave (FMCW) radar are widely used in short-range and middle-range applications due to its low cost and simplicity, FMCW waveform is the main research subject. The FMCW signal model is derived and analysed in Chapter 2 which for the first time takes both the range migration and wideband DOA problems into account at the same time.

The point-like moving targets are considered in Chapter 3 where their Doppler velocities are within the maximum unambiguous velocity of the radar. A novel improved multiple signal classification (MUSIC) algorithm with the dynamic noise-subspace method is proposed to address both the range migration and wideband DOA problems. The algorithm releases the great potentials of the conventional MUSIC algorithm in the presence of the range migration. Moreover, an efficient algorithm based-on Rayleigh-Ritz step is introduced for the proposed method resulting in a considerable reduction of computational requirements without any performance degradation. Comparison with the conventional narrow-band MUSIC, Keystone-MUSIC, inversion-MUSIC and corresponding Cramér-Rao bounds (CRB) using simulations, reveals the superiority of the method proposed in terms of accuracy, resolution and efficiency.

The problems similar to those considered in Chapter 3 but in the presence of the Doppler ambiguity are considered in Chapter 4. A spectral norm-based algorithm is proposed to address the coupling terms for a single moving point-like target. The algorithm for the first time abandons the integration-based method for ambiguous velocity estimation. The spectral-norm based algorithm provides a new tool to resolve the ambiguity problem which outperforms the conventional integration-based algorithm by avoiding the off-grid problem with limited data size. Moreover, com-

bined with the modified CLEAN techniques and Greedy algorithm, the proposed algorithm can be extended to multiple moving targets. Furthermore, the power iteration algorithm is smartly adopted for an efficient implementation of the proposed method.

After addressing the point-like targets, the moving extended targets are studied in Chapter 5 especially when multiple extended targets cannot be separated both in range and beam profile. The Doppler difference is used to recognise them and inverse synthetic aperture radar (ISAR) concept is adopted to split and image the targets separately. The conventional entropy minimisation approach is applied to the signal model for not only the Fourier spectrum but also the eigenspectrum as well for the first time. The Fourier spectrum has a relatively high resolution in higher-order motion (e.g. acceleration) while eigenspectrum has a better resolution in Doppler separation. The advantages of both spectra are utilised to separate multiple extended targets by a simple but powerful combination. Via numerical simulation, the applicability of the algorithm in the automotive application is demonstrated.

Last in Chapter 6, by processing the experimental data from automotive radar, we present a novel and fast imaging algorithm for slow-moving targets which provides super-resolution on DOA. The range information is processed via fast Fourier transform (FFT) for efficiency while the DOA is estimated by the MUSIC algorithm for super-resolution. Since the MUSIC spectrum is pseudo-spectrum and can not represent the correct dynamic range of the imaging results, a novel normalisation method is introduced to vividly indicate the energies of different targets. In comparison with conventional FFT-BF, a cleaner range-azimuth image is obtained with the proposed algorithm demonstrating higher angular resolution and without strong side-lobes.

Although the research presented in this thesis is served for automotive application, some of the algorithms and ideas can be easily generalised for a broad spectrum of diverse applications.

SAMENVATTING

Als een van de belangrijkste sensoren in autonoom rijden, heeft radar grote voordelen ten opzichte van andere sensoren, met name zijn mogelijkheden gedurende ongunstige weersomstandigheden en Doppler-informatie-extractie.

Prestaties van de radar in termen van nauwkeurigheid en doelresolutie zijn sterk afhankelijk van de uitgezonden radargolfvormen en toegepaste signaalverwerkingsalgoritmen. Om een hoge bereikresolutie te bereiken, moet een ultrabreedbandsignaal worden gebruikt voor waarneming, wat moeilijkheden veroorzaakt als tegelijkertijd een hoge Doppler- en DOA-schatting moet worden verkregen, vanwege de bereikmigratie. Om dit probleem aan te pakken, worden in dit proefschrift nieuwe signaalverwerkingsalgoritmen voorgesteld, die de weg vrijmaken voor verbeterde prestaties van de autoradarsensor.

Aangezien de frequentie-gemoduleerde continue golf (FMCW) -radar vanwege zijn lage kosten en eenvoud op grote schaal wordt gebruikt in toepassingen op korte en middellange afstanden, is de FMCW-golfvorm het belangrijkste onderzoeksonderwerp. Het FMCW-signaalmodel wordt afgeleid en geanalyseerd in hoofdstuk 2, dat voor het eerst tegelijkertijd rekening houdt met zowel de migratie van het bereik als de breedband-DOA-problemen.

De bewegende puntvormige doelen worden in hoofdstuk 3 besproken, waar hun Doppler-snelheden binnen de maximale ondubbelzinnige snelheid van de radar liggen. Een nieuw verbeterd MUSIC-algoritme met de dynamische ruissubruimtemethode wordt voorgesteld om zowel de migratie van het bereik als de breedband-DOA-problemen aan te pakken. Het algoritme maakt de grote gebruiksmogelijkheden van het conventionele MUSIC-algoritme mogelijk in aanwezigheid van de bereikmigratie. Bovendien wordt een efficiënt algoritme gebaseerd op de Rayleigh-Ritz-stap geïntroduceerd voor de voorgestelde methode, wat resulteert in een aanzienlijke vermindering van de computationele vereisten zonder enige prestatievermindering. In vergelijking met de conventionele smalbandige MUSIC, Keystone-MUSIC, inversion-MUSIC en bijbehorende CRB met simulaties, wordt de superioriteit van de voorgestelde methode in termen van nauwkeurigheid, resolutie en efficiëntie getoond.

De problemen die vergelijkbaar zijn met die in hoofdstuk 3, maar in aanwezigheid van de Doppler-ambiguïteit, worden in hoofdstuk 4 besproken. Er wordt een op spectraalnorm gebaseerd algoritme voorgesteld dat zich richt op de koppelingsvoorwaarden voor een enkel bewegend puntvormig doel. Het algoritme laat voor

het eerst de op de integratie gebaseerde methode voor dubbelzinnige snelheidsschatting zien. Het op de spectrale norm gebaseerde algoritme biedt een nieuw hulpmiddel om het dubbelzinnigheidsprobleem op te lossen dat beter presteert dan het conventionele op integratie gebaseerde algoritme, door de off-grid-problemen met beperkte gegevensomvang te vermijden. Bovendien, in combinatie met de aangepaste CLEAN-technieken en het Greedy-algoritme, kan het voorgestelde algoritme worden uitgebreid tot meerdere bewegende doelen. Uiteindelijk wordt het power iteratie-algoritme slim toegepast voor een efficiënte implementatie van de voorgestelde methode.

Na het aanpakken van de puntvormige doelen, worden de bewegende uitgebreide doelen bestudeerd in Hoofdstuk 5, vooral wanneer meerdere uitgebreide doelen niet te splitsen zijn in zowel bereik als straalprofiel. Het Doppler-verschil wordt gebruikt om ze te herkennen en het ISAR-concept wordt gebruikt om de doelen afzonderlijk te splitsen en in beeld te brengen. De conventionele benadering voor het minimaliseren van entropie wordt voor het eerst toegepast op het signaalmodel voor niet alleen het Fourier-spectrum, maar ook voor het eigenspectrum. Het Fourier-spectrum heeft een relatief hoge resolutie bij bewegingen van hogere orde (bijv. versnelling), terwijl het eigenspectrum een betere resolutie heeft bij Doppler-scheiding. De voordelen van beide spectra worden gebruikt om meerdere uitgebreide doelen te scheiden door een eenvoudige maar krachtige combinatie. Via numerieke simulatie wordt de toepasbaarheid van het algoritme in de automotive-applicatie gedemonstreerd.

Als laatste in hoofdstuk 6 presenteren we, door de experimentele gegevens van autoradars te verwerken, een nieuw en snel beeldvormingsalgoritme voor langzaam bewegende doelen dat een superresolutie op DOA biedt. De bereikinformatie wordt voor efficiëntie verwerkt via FFT, terwijl de DOA wordt geschat door het MUSIC-algoritme voor superresolutie. Aangezien het MUSIC-spectrum een pseudo-spectrum is en niet het juiste dynamische bereik van de afbeeldingsresultaten kan vertegenwoordigen, wordt een nieuwe normalisatiemethode geïntroduceerd om de energie van verschillende doelen dynamisch aan te geven. In vergelijking met conventionele FFT-BF wordt met het voorgestelde algoritme een schoner bereik-azimut beeld verkregen met een hogere hoekresolutie zonder sterke zijlobben.

Hoewel het in dit proefschrift gepresenteerde onderzoek wordt gebruikt voor automotive toepassingen, kunnen sommige algoritmen en ideeën gemakkelijk worden gegeneraliseerd voor een divers breed spectrum van toepassingen.

LIST OF SYMBOLS AND NOTATIONS

a, A	Scalars are denoted by normal letters
$\mathbf{a}$	Vectors are denoted by lower-case bold-face letters
$\mathbf{A}$	Matrices are denoted by upper-case bold-face letters
$\boldsymbol{\mathcal{A}}$	Tensors are denoted by bold calligraphic letters
$\mathbf{A}^T$	Transpose of matrix $\mathbf{A}$
$\mathbf{A}^*$	Complex conjugate of matrix $\mathbf{A}$
$\mathbf{A}^H$	Conjugate transpose of matrix $\mathbf{A}$
$\|\|\mathbf{A}\|\|_2$	Spectral norm of matrix $\mathbf{A}$
$\|\|\mathbf{A}\|\|_F$	Frobenius norm of matrix $\mathbf{A}$
$\|\|\mathbf{A}\|\|_{\max}$, $\|\|\mathbf{a}\|\|_{\max}$	Returns the maximum absolute value of the entry in matrix $\mathbf{A}$ or vector $\mathbf{a}$
$\text{abs}(\mathbf{A})$	Returns the matrix with the absolute values of all entries of matrix $\mathbf{A}$
$\sigma(\mathbf{A})$	Spectrum of the matrix $\mathbf{A}$
$[\mathbf{A}]_{p,q}$	Returns the entry of matrix $\mathbf{A}$ at the $(p+1)$th row and $(q+1)$th column
$[\boldsymbol{\mathcal{A}}]_{p,q,r}$	Returns the entry of tensor $\mathcal{A}$ at the $(p+1)$th row, $(q+1)$th column and $(r+1)$th tube
$\mathbf{orth}(\mathbf{A})$	Orthogonisation of the columns of matrix $\mathbf{A}$
$\mathbf{diag}(\mathbf{A})$	Returns the diagonal entries of matrix $\mathbf{A}$
$\mathbf{vec}(\mathbf{A})$	Vectorisation of matrix $\mathbf{A}$ by stacking the columns together
$\text{Tr}(\mathbf{A})$	Returns the trace of a matrix $\mathbf{A}$
$\otimes$	Kronecker product
$\odot$	Hadamard product
$\oslash$	Elementwise division
$\circ$	Outer product
$\times_n$	Tensor n-mode product
$\lfloor x \rfloor$	Gives the nearest integer less than or equal to x
$\lfloor x \rceil$	Gives the nearest integer to x
$\mathbf{I}$	Identity matrix

$\mathscr{F}(\cdot)$	Fourier transform
$\mathbb{E}(\cdot)$	Expectation operation
$\Re(\cdot)$	Real part extraction
$\Im(\cdot)$	Imaginary part extraction
$\delta(\cdot)$	Kronecker delta function
$\mathrm{sinc}(\cdot)$	Sinc function
$\mathrm{corr}(\cdot,\cdot)$	Correlation operation
$\mathcal{O}$	Asymptotic notation
$\mathbb{R}$	Real number field
$\mathbb{C}$	Complex number field

1

INTRODUCTION

1.1. MOTIVATION OF RESEARCH

A new civilisation era is coming with the boom of the technologies. Especially with the rapid development of computer science and sensor techniques, mankind will gradually liberate the labour force and achieve a highly automated industry. Obviously, the road to such a future is not always smooth and a lot of challenges are presented in the path. In addition to superior computing power, sensor science is another significant challenge. With advanced sensors and related signal processing methods, the scope of human activities has been greatly increased, and the ability to perceive and explore the world has been significantly enhanced.

Although many kinds of sensors have been developed for environment sensing, for example, Fig. 1.1 shows the properties of the main sensors in the automotive applications, none of them is omnipotent[1]. Fig. 1.1 also indicates that radar has the most advantages among these sensors. Especially for the Doppler velocity estimation, radar has an absolute advantage over other sensors. Thus, it will play an irreplaceable role in automotive sensors. However, there are some great challenges of radar need to be urgently solved for future application in the complex environment.

There are three main kinds of resolutions in automotive radar, namely, range resolution, Doppler frequency resolution and DOA resolution. To satisfy the requirement of the range resolution, the bandwidth of the waveforms is increased significantly. This subsequently, however, brings several challenges to moving targets detection and corresponding parameters estimation, especially for the fast-moving objects.

[1] Source: https://www.unitedlex.com

1

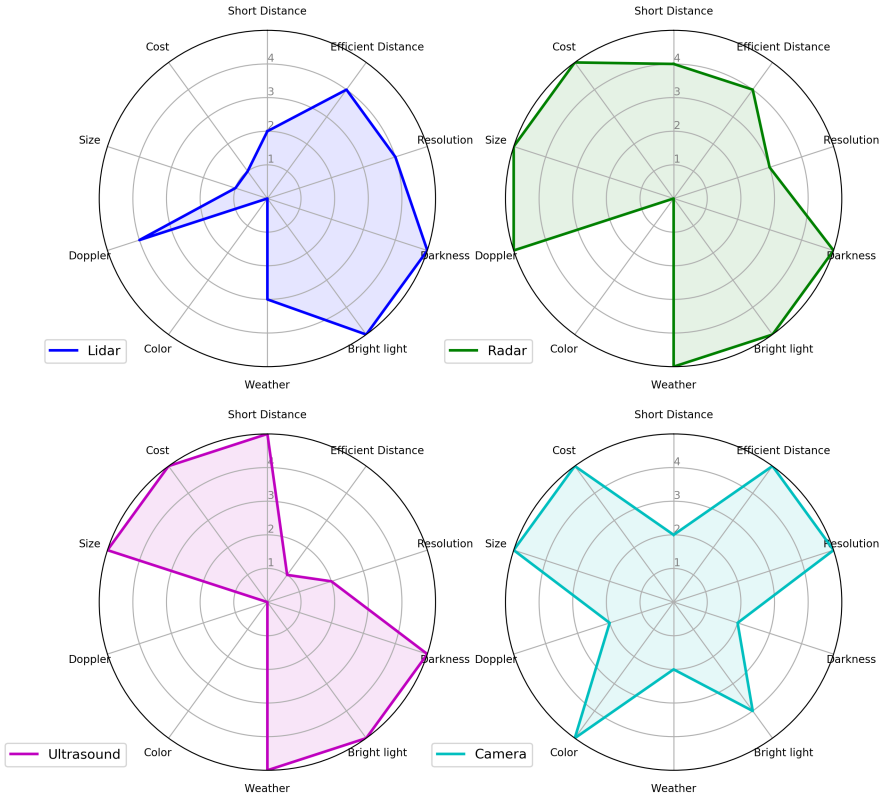

Figure 1.1: Comparison of different sensors in automotive application, where the performances are rated by 5 grades from 0 (bad) to 5 (best)

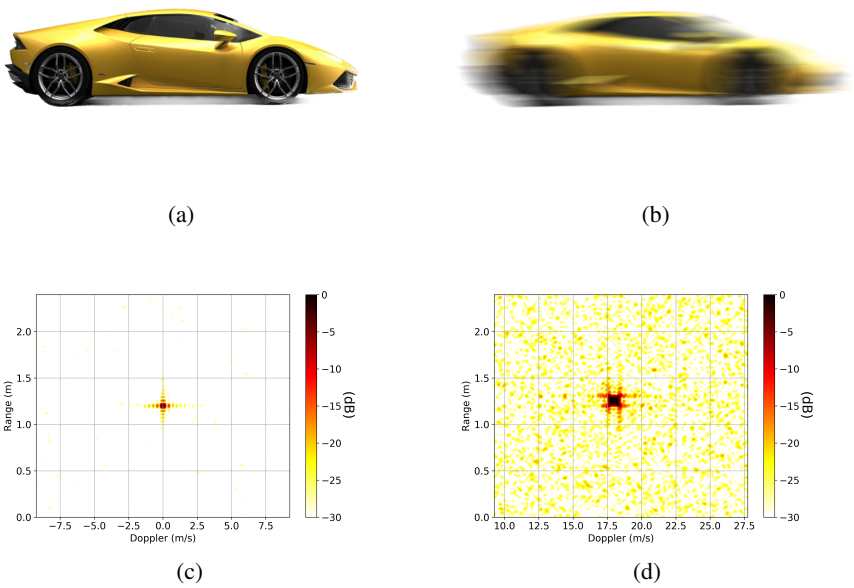

Figure 1.2: Long-time exposure of camera of (a) stationary car and (b) fast-moving car and long-time illumination of radar of (c) stationary point target and (d) fast-moving point target

One primary challenge is the range migration phenomenon and the related Doppler ambiguity problem. For better targets detection and higher Doppler resolution, long-time microwave illumination for the targets are necessary. However, fast-moving targets might migrate several range resolution cells during this time and bring difficulties for joint range and Doppler frequency estimation. The influence of range migration of one single point target on the Fourier spectrum is illustrated in Fig. 1.2 and compared with photos of a car with long-time exposure.

The range migration problem becomes more evident and cannot be ignored when UWB signals are applied. There are two main directions to treat the range migration. The first one is to eliminate the range migration and obtain the focused targets when the Doppler shifts are smaller than the maximum unambiguous velocity which depends on the radar settings. Another direction is when the Doppler ambiguities happen and the fold numbers are expected to be estimated from the range migration. The first case, for example, happens to vehicles mounted with automotive radar when they are driven in the city or rural area and the second case will be considered on the highway.

Another great challenge is the wideband DOA problem. Since the conventional

so-called super-resolution algorithms are formulated based on the assumptions of the narrowband signals, they cannot directly be applied to the wideband cases. Although some wideband DOA algorithms have been proposed, they are not optimised for joint parameters estimation with limited data. New signal processing methods for joint estimation of wideband DOA, Doppler and range with super-resolution abilities are urgently required.

1.2. STATE OF THE ART AND CHALLENGES

1.2.1. RANGE MIGRATION

Detection and localisation of moving targets are important in many fields such as automotive radar [1], ground moving target indication (GMTI) [2], underwater acoustic array [3]. The most important parameters of moving targets are range, azimuthal (and, in 3D space, elevation) angle (or DOA) and velocity. The target range and angle together determine the location of a target. The Doppler (along with range) velocity is usually determined in coherent radars by means of phase shift between chirps within the coherent processing interval (CPI), and DOA is determined from the phase shift of signals received by different antennas within antenna array. Both phase shifts can be easily measured separately using narrowband radar. Using the de-chirping technique for FMCW radar [2, 4], the received signals are transformed into multi-dimensional complex sinusoids (whose phase depends on the fast-time - range, slow-time - Doppler velocity and array element - DOA), which will be discussed in the next chapter. Then the estimation of target's parameters is transformed into the frequencies estimation problem. By extending traditional single-frequency estimators to joint multiple frequencies estimators, such as matched filter, 2D-Capon [5], 2D-MUSIC [6], 2D-ESPRIT [7] and sparse representation methods [8, 9], joint range-Doppler estimation algorithms have been developed. These algorithms perform well under narrowband signal condition. Target movement causes, however, change in the target range during one CPI (physically) and the cross-couplings between fast-time and slow-time (mathematically), which is called range walk or range migration in GMTI [2, 10, 11]. The cross-coupling terms spread the Fourier spectrum and consequently lead to resolution losses and estimation errors for these classic algorithms: the larger the signal bandwidth or the higher the target velocity, the higher the estimation error of conventional methods [10, 12].

Recently, since wideband signals are widely used due to the demand of increasingly higher range resolution, the range migration problem has attracted significant attention. To solve the target migration problem, the relaxation-based super-resolution algorithms have been proposed in [2, 13, 14] for multiple moving target feature extractions. However, they consider a wideband approach for the range pro-

file, while they assume a narrowband approach for the steering vector. In [15], the authors present the iterative adaptive algorithm (IAA) for joint multiple parameters estimation, which provides super-resolution by iteratively calculating the covariance matrix together with estimation results. In [16, 17], IAA is extended to the wideband waveform case together with the range migration problem. However, IAA consumes a huge amount of memory and time when the raw data dimension is large and the scanning area is divided into dense bins, which makes the algorithm impractical for real-time applications. The Keystone transform and matched filter were used in [12, 18] to eliminate the range walk residual and the Radon Fourier transform (RFT) was proposed to consider even higher-order coupling problems by line or curve searching in the frequency domain in [10, 19]. Unfortunately, these approaches need a large amount of raw data to do interpolation or coherent integration, therefore they could not provide the same fine resolution as the super-resolution algorithms in [6, 15]. Implementation of the RFT also requires a large amount of computing power for the line searching in multi-dimensional data. Some waveform design methods are also proposed to solve the range migration problem [11], but these algorithms increase the system's complexity and the achieved resolution is not as high as that obtained by super-resolution algorithms.

1.2.2. DOPPLER AMBIGUITY

According to the Nyquist sampling criterion, there exists a maximum unambiguous velocity which is determined by the constant pulse repetition frequency (PRF). When the target radial velocity is larger than the maximum unambiguous velocity, it will be folded into the unambiguous domain of the Doppler spectrum. This problem is common for the low PRF waveforms. Although some waveform design techniques for unambiguous estimation of Doppler and range (such as multiple pulse repetition frequencies (MPRF) combined with Chinese Remainder Theorem (CRT) [20] or up-/down-chirps [21]) have been proposed, these approaches increase the system complexity and have unsatisfactory performance under low signal-to-noise-ratio (SNR) conditions, which is not a good solution for automotive radar.

For the single PRF waveforms, solutions for the unambiguous Doppler frequency by using the range migration coupling term has been proposed in several papers [10, 16, 22–35]. The methods proposed can be roughly divided into three categories: parametric methods, incoherent integration-based and coherent integration-based methods. The parametric methods use the model of the noise covariance matrix and solve the problem by Bayes estimator. [22–24]. In addition to the heavy computational load, these methods are also usually very sensitive to the parameters setting and the initialization. The incoherent integration methods, for instance, Hough transform (HT) [25], suffer from their poor performance under the low SNR conditions. The coherent methods are usually performed by the matched

filter (MF) bank, e.g., W-Capon, W-APES [26], time-reversing transform [27, 28], scaled inverse Fourier transform [29], modified location rotation transform [30], IAA which is extended to the wideband waveforms [16]. Keystone transform in combination with some focusing criteria can also be applied to unambiguous velocity extraction [31–33]. Another famous coherent integration method is RFT by coupling terms compensation and integration and it is shown in [10, 34, 35] that the generalised RFT is the optimal coherent integration-based method for rectilinearly moving targets under the white Gaussian noise background. However, to accurately resolve the Doppler ambiguity, the coherent integration approaches usually require large data size to perform interpolation or coherent integration, which is often not available due to the limited observation time. Moreover, without appropriate grid oversampling, MF suffers from the collapsing loss for the off-grid targets. Moderate oversampling in every dimension is required to overcome this problem, hence with an increased computational burden.

1.2.3. MOTION PARAMETERS ESTIMATION OF EXTENDED TARGETS

The above-mentioned algorithm and techniques are principally applied to the point-like targets. However, in addition to detection and estimation, the "*shape*" of the targets is desired for target recognition. By increasing the illuminating time, the Doppler resolution can be increased to observe the Doppler differences of scatterers within one extended target, which is the well-known ISAR imaging [36]. Then the "*shape*" of the targets could be recognised. The long-time illumination brings severe range migration for moving targets, but also provides more information of the motion parameters of the targets. Therefore, the range alignment by motion compensation is one of the key problems for the focused images of the target in ISAR application.

ISAR imaging of a single target has been thoroughly studied and is widely used for target classification and recognition [37]. One of the key techniques for ISAR imaging is the range alignment by motion compensation. Many algorithms have been proposed for motion parameters estimation, such as the centroid tracking algorithm [38], the entropy minimisation (EM) [39], the phase gradient auto-focusing technique [40], the image contrast maximisation [41]. Among them, EM is one of the most popular and widely used methods. Moreover, many improved algorithms based on EM have been introduced, such as Rényi entropy [42], Tsallis entropy [43] and efficient implementation of EM [44, 45].

However, if there are multiple closely spaced targets presented in the observed scene, the conventional methods of range alignment and phase adjustment for the only single target may fail to separate the targets with slightly different velocities or accelerations. Current approaches of multiple targets separation in ISAR imaging can be roughly categorised into two classes: separated imaging and direct imaging.

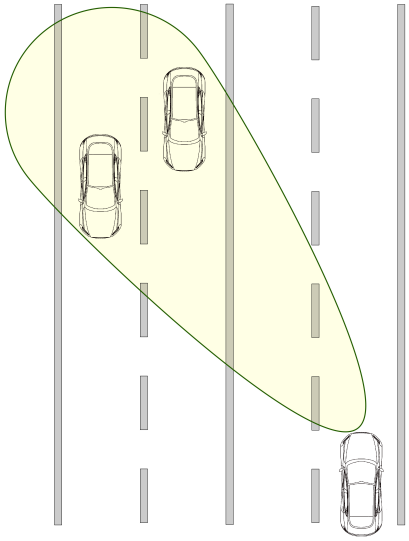

Figure 1.3: Dense vehicular scenario where two cars cannot be separated in both beam and range profile

If the targets are not coupled, a coarse image of the targets can be obtained and the targets can be separated in the coarse image using imaging segmentation techniques [36, 46, 47] or sparse representation [48] and more precise image can be achieved by accurate motion compensation separately.

However, a more challenging scenario is that the targets are coupled with each other and the range histories are overlapped. For such cases, several popular types of algorithms are intensively studied. One is based on time-frequency (TF) analysis which is used to separate different sources in TF domain [49–52]. The drawbacks of the TF analysis are either the cross-terms for Wigner-Ville distribution(WVD) and Radon-Wigner transform (RWT) or the low frequency resolution for short-time Fourier transform (STFT). Another famous algorithm which is based on fractional Fourier transform (FrFT) [53] to extract the higher-order rate of the signal which is corresponding to the acceleration and jerk. However, the targets with the same or similar acceleration are difficult to be recognised by FrFT. Several lines or curves detection based algorithms [54, 55], such as Hough Transform, are applied to separate the range profile of each target. However, the performance of these algorithms decreases significantly when the range histories of different targets seriously coupled. Another type is the exhaustive search of the motion parameters and using auto-focusing criteria as the indications to estimate these parameters [46, 56, 57]. Based on the auto-focusing approach, many algorithms are introduced to separate and image multiple moving targets, e.g., the Modified Keystone [53,58] and Radon-

1

Transform [46].

1.2.4. WIDEBAND DOA

In addition to the range migration, another limitation for (Ultra-)WB signal in the collocated array or multiple-input and multiple-output (MIMO) application is the DOA estimation. Although the range migration problem has been studied intensively, the current algorithms jointly dealing with range migration and DOA estimation fail to provide a good solution to wideband DOA estimation by simplifying the signal model with narrowband DOA assumption [2,14,59]. The traditional DOA estimators are based on narrowband assumptions by the interferometry information, such as Capon, MUSIC, etc. To apply the traditional narrowband super-resolution algorithm for wideband cases, two of the mainstreams of wideband DOA estimation are proposed, namely the incoherent signal subspace method (ISSM) and the coherent signal subspace method (CSSM). ISSM solves this problem via a filter bank to decompose the array output into its independent narrowband components. Then the subspace algorithm is applied to each narrowband output, and DOA estimates can be averaged in some way. However, each of narrowband estimates does not fully exploit the total emitter power and some of the narrowband components may have a low SNR, and the final DOA estimates may be adversely affected by a few inaccurate narrowband estimates [60]. CSSM combines the different narrowband signal subspace into a single signal subspace that obeys the narrowband array model. Although it is shown in [60] that the performance of CSSM is superior to ISSM, the forming of focusing matrices and universal spatial covariance matrix (USCM) can increase the computational complexity significantly. In addition, the accuracy of the focussing matrices highly depends on and is sensitive to the preliminary estimate of the true DOAs [61]. In some other communication problems, joint time-of-arrival (TOA) and DOA estimation in impulse radio (IR)-UWB are studied, unfortunately, the DOAs are estimated by the pulse delay which is determined by the bandwidth and not suitable for the colocated array. Another powerful tool for DOA estimation is the time-frequency(TF)-MUSIC [62, 63] which is used to deal with non-stationary sources and it is also applied for wideband DOA estimation in a similar way as CSSM [64]. However, in FMCW radar, the de-chirped signals (beat frequency signals) for each antenna element behaves as "stationary sources", so an application of TF-MUSIC to them is not helpful.

The main motivation of this research is to develop some new algorithms which could not only estimate the wideband DOAs with the capability of super-resolution but also take the range migration problem into account. Most importantly, all the parameters, i.e., range, Doppler and DOA are estimated jointly. The algorithms should be adaptive to different scenarios. For instance, in the automotive application, the Doppler ambiguity is not considered to alleviate the computational burden

when the vehicles are driven in the city or rural place while it has to be considered when people are driving on a highway. Moreover, the more demanding scenario is the targets imaging when they are hardly separable in the range or beam profile.

1.3. RESEACH OBJECTIVES AND NOVELTIES

This dissertation aims to develop advanced algorithms for joint parameters estimation of multiple fast-moving targets. To achieve these objectives, the following research questions will be addressed step by step

- Joint DOA and Doppler estimation by eliminating the range migration.
- Joint Doppler, DOA and range estimation using UWB FMCW signals in the presence of the Doppler ambiguity.
- Joint Doppler and range estimation for imaging of multiple extended targets.
- Efficient FFT-MUSIC algorithm for automotive application.

1.4. OUTLINES OF THE THESIS

The rest of the thesis is organised as follows:

- **Chapter 2** Fundamentals of FMCW and wideband signal model.

  This chapter gives a brief introduction of the FMCW theory and the corresponding wideband signal model for multiple moving targets are established. The signal model takes advantage of the property of the linear modulated frequency and transform the wideband DOA as the coupling terms in the signal model analogous to the range migration. As such, the range migration and the wideband DOA problem are treated in a similar way. The challenges and the constraints of the migration problem and wideband DOA are reviewed with the mathematical model. This signal model will be used in the following chapters.

- **Chapter 3** Joint parameters estimation using compensated MUSIC algorithm.

  This chapter tries to modify the conventional MUSIC algorithm to the proposed wideband signal model where the Doppler ambiguity is not considered. A novel compensated MUSIC algorithm is proposed in this chapter to adjust the phase in each searching grid and the dynamic noise subspace is extracted to improve the estimation accuracy and resolution. Both 2D and 3D MUSIC algorithm with the proposed compensation method are presented. Moreover, efficient implementations are proposed and the corresponding performances

are compared for the 2D case. Finally, the performances of the proposed methods are compared with other algorithms and validated by the simulation results.

The publications related to this chapter are the following:

- S. Xu and A. Yarovoy, "Joint Doppler and DOA estimation using 2D MUSIC in presence of phase residual," *2017 European Radar Conference (EURAD)*, Nuremberg, 2017, pp. 203-206. doi: 10.23919/EURAD.2017.8249182
- S. Xu and A. Yarovoy, "Joint Parameters Estimation Using 3D Tensor MUSIC in the Presence of Phase Residual," *2018 International Conference on Radar (RADAR)*, Brisbane, QLD, 2018, pp. 1-4. doi: 10.1109/RADAR.2018.8557322
- S. Xu, B. J. Kooij and A. Yarovoy, "Joint Doppler and DOA Estimation Using (Ultra-)Wideband FMCW Signals," *Signal Processing*, 168(2020): 107259.

- **Chapter 4** Joint parameters estimation using spectral norm-based algorithm.

  Since the proposed algorithm in the previous chapter has limited potential for the estimation of Doppler ambiguity, a new algorithm is introduced in this chapter. The algorithm uses the same signal model from Chapter 2 in which the Doppler ambiguities are also considered. The spectral norm-based algorithm for a single target is presented and subsequently applied Greedy and RELAX algorithms, the proposed methods can be easily extended to multiple targets. In addition, the power iteration algorithm is adopted to accelerate the algorithm. Finally, the simulation results show the superiorities of the algorithm over the coherent integration-based algorithm in accuracy and computational time with limited data.

  The publication related to this chapter is

  - S. Xu, and A. Yarovoy, "Joint Features Extraction for Multiple Moving Targets Using (Ultra-)Wideband FMCW Signals in presence of Doppler Ambiguity," *IEEE Transactions on Signal Processing*, under review after revision.

- **Chapter 5** A novel auto-focusing algorithm using entropies of both eigenspectrum and Fourier spectrum for closely multiple extended targets.

  The previous algorithms are based on the point-like targets, while in this chapter, the extended targets are considered. The closely positioned targets

which cannot be separated either in the range profile or the beam is the extreme case in multiple targets imaging. The conventional auto-focusing criteria, e.g. Shannon entropy of the Fourier spectrum would fail to separate two targets if they move with similar radial velocities. The proposed entropy of eigenspectrum has much higher sensitivity in the Doppler differences, and thus, can be used in such cases. Combined the entropies of both Fourier spectrum and eigenspectrum, a new algorithm having both high resolutions in velocity and acceleration is introduced. The real geometry simulation validates the applicability of the proposed algorithm.

The publication related to this chapter is

  - S. Xu, and A. Yarovoy, "Minimum Entropy of the Eigen Spectrum for Motion Parameters Estimation of Multiple Extended-Targets," *IEEE Sensors Journal*, under review.

- **Chapter 6** Super-resolution DOA with FFT-MUSIC Algorithm for Automotive Radar Imaging.

  Although some efficient implementations have been introduced in previous chapters, they are still computationally intensive for current computers. In this chapter, an efficient FFT-MUSIC algorithm is proposed for the range-azimuth image of slow-moving objects. The performance of the algorithm is compared with conventional beamforming algorithm using the experimental data collected from a moving car in the complex environment. Despite the slightly increased computational load, the proposed algorithm provide much higher angular resolution than beamforming method without strong sidelobes and can be implemented in real-time.

  The publication related to this chapter is

  - S. Xu, J. Wang and A. Yarovoy, "Super Resolution DOA for FMCW Automotive Radar Imaging," *2018 IEEE Conference on Antenna Measurements & Applications (CAMA)*, Vasteras, 2018, pp. 1-4.
    doi: 10.1109/CAMA.2018.8530609

- **Chapter 7** Conclusions.

  The conclusions are drawn in this chapter and some recommendations for the future research are presented.

2

FUNDAMENTALS OF FMCW AND WIDEBAND SIGNAL MODEL

2.1. FMCW

In this section, some basic concepts of FMCW and related terms are briefly reviewed. Furthermore, the signal model of multiple moving point-like targets using UWB FMCW antenna array is provided and discussed.

2.1.1. CW RADAR

Continuous-wave (CW) radar systems transmit the electromagnetic wave continuously and the echo reflections from the objects are received and recoded simultaneously and continuously as well [65]. Since the high duty ratio is achieved, it has much higher integrated energy in a short time than the pulse counterpart. Bistatic configuration is employed for CW radars, and since the transmitter and receiver cannot be isolated perfectly, the direct wave from the transmitter to the receiver will influence the received signals. This problem, subsequently, relegates CW systems to relatively low power and hence short-range applications.

Since the range of the targets is determined by the EM wave's round-trip delay, the characteristics of the CW waveforms must be changing to retrieve the range information (e.g., change the wave's frequency or phase over time).

2.1.2. FMCW

There are several possible modulation patterns which can be used for different measurement purposes:

- Sawtooth modulation, also called linear frequency-modulated continuous-wave (LFMCW or FMCW).

- Triangular modulation.
- Square-wave modulation (simple frequency-shift keying, FSK).
- Stepped modulation (staircase voltage).
- Sinusoidal modulation.

Among these modulations, FMCW (upward ramps sawtooth modulation) is widely used in the automotive radar and is the main object of the research in this thesis. The FMCW signal in the time-frequency domain is illustrated in Fig. 2.1. The T_0 is the chirp duration in which the frequency is linearly modulated with time. After the frequency reaches the maximum value, the time interval t_{settle} is needed to reset the frequency to the starting frequency. Since the initial time of the modulation could be nonlinear or unstable, the only useful data are collected in the time periods which are shown as the green line in Fig. 2.1.

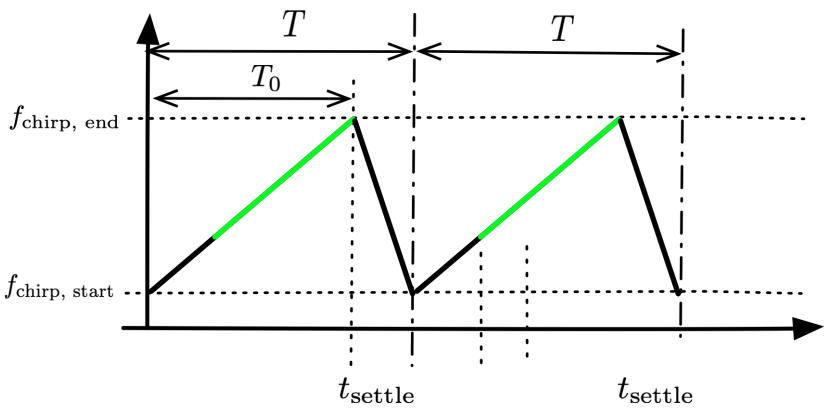

Figure 2.1: FMCW Signal Model

The main advantages of FMCW automotive radar over other waveforms includes:

- Simultaneous ranges and Doppler velocities estimation;
- Relatively low sampling frequency with de-chirping technique;
- Narrowbandd processing (after de-chirping) for short-range applications;
- Safety with low transmitted power;
- Low cost;
- Portable size;

- Simplicity;
- High reliability;
- Good sensitivity.

2.1.3. De-chirping Techniques

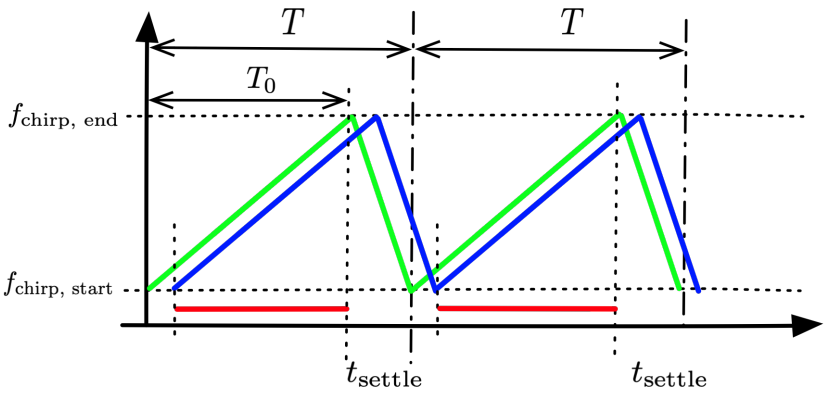

Figure 2.2: Illustration of de-chirping techniques

Different from pulse radar, the received chirp signals can be processed by the matched filter or the so-called de-chirping or de-ramping techniques analogously. Fig. 2.2 shows the theory of de-chirping techniques, where the green line indicates the time-frequency relation of the transmitted chirp signal and the received chirp signal is denoted by the blue line. The de-chirped signal is obtained by instantaneous frequency differences between the transmitted and received chirps (indicated by the red line), which is called the beat frequency signal or beat signal. The beat signal contains the range information as well as the Doppler information. However, the Doppler frequency shift in one beat signal usually is much smaller than that of range and is mostly negligible. To obtain the Doppler information, multiple chirps are used and Doppler frequency is estimated from the phase shift within multiple beat signals.

There are many advantages to apply de-chirping technique other than the matched filter. In addition to the simple implementation in the analogous circuits, the sampling frequency is dramatically reduced, which will be discussed in the signal model in detail.

However, there is also some limitations of FMCW. As we will show in the signal model, usually the maximum unambiguous velocity and maximum unambiguous range are hard to be achieved with low sampling frequency simultaneously.

2.2. FMCW SIGNAL MODEL

2.2.1. SIGNAL MODEL

In this section, the signal model using a monostatic antenna array with one transmitter and L receivers is formulated. Without losing generality, the uniformly distributed linear array (ULA) with omnidirectional elements is considered for the receivers. Assume I point targets with unknown initial range $\mathbf{r} = [R_1, R_2, ..., R_I]$, radial velocity $\mathbf{v} = [v_1, v_2, ..., v_I]$ and angle $\boldsymbol{\theta} = [\theta_1, \theta_2, ..., \theta_I]$ are located in the observed far-field. During one CPI a sequence of FMCW chirps is transmitted with the chirp duration T_0 and the pulse repetition interval (PRI) T. A normalised single chirp signal with bandwidth B has the form

$$s_0(t) = \begin{cases} e^{j2\pi(f_0 t + 0.5\mu t^2)} & t \in [0, T_0], \\ \text{settle time} & t \in (T_0, T), \end{cases} \tag{2.1}$$

where $f_0 = f_{\text{chirp, start}}$ is the starting frequency, $\mu = \dfrac{B}{T_0}$ denotes the frequency modulation rate and the settle time is the system reset interval. The periodic transmitted signal is decomposed into fast-time domain t' and chirp number (slow-time) domain $m = \left\lfloor \dfrac{t}{T} \right\rfloor$ as $t' = t - mT,\ t' \in [0, T_0]$, where $m = 0, 1, 2, ..., M-1$ and M is the total number of the chirps in one CPI.

Then the periodically transmitted signal can be expressed as

$$s(t) = s(t' + mT) = s(m, t') = s_0(t'). \tag{2.2}$$

Consider the ith scatterer in the observation domain with the radial velocity v_i and the initial range R_i, the round trip delay of the reflected signal for ith scatterer is

$$\tau_i(m, t') = \frac{2(R_i + v_i(t' + mT))}{c} = \gamma_i + \frac{2v_i}{c}(t' + mT), \tag{2.3}$$

where c is the speed of light and $\gamma_i = \dfrac{2R_i}{c} \ll T_0$ is the initial round trip delay of ith scatterer. Using the 0th element of the array as the reference, the received signal of ith scatterer by the lth element can be written as

$$\begin{aligned} r_i^{(l)}(m, t') &= \alpha_i e^{j\varphi_i^{(l)}} s(t' + mT - \tau_i(m, t')) \\ &= \alpha_i e^{j\varphi_i^{(l)}} e^{j2\pi\phi_i(m,t')}, \\ \text{with } t' &\in [\gamma_i, T_0], \end{aligned} \tag{2.4}$$

where the superscript (l) denotes the lth element of receiver array, $l = 0, 1, 2, ..., L-1$ denotes the indices of element and L is the total number of the receivers, α_i is

the constant complex amplitude of ith scatterer, $\exp(j\varphi_i^{(l)})$ denotes the phase delay relative to the 0th element, and according to (2.2) the term $2\pi\phi_i(m,t)$ has the form

$$\phi_i(m,t') = f_0(t' - \tau_i(m,t')) + 0.5\mu(t' - \tau_i(m,t'))^2, \quad \text{with } t' \in [\gamma_i, T_0]. \tag{2.5}$$

From the phase of the received signal, the instantaneous frequency of the received signal is extracted as

$$\begin{aligned} f_i(m,t') &= \frac{\partial\phi_i(m,t')}{\partial t'} \\ &= f_0\left(1 - \frac{\partial\tau_i(m,t')}{\partial t'}\right) + \mu(t' - \tau_i(m,t'))\left(1 - \frac{\partial\tau_i(m,t')}{\partial t'}\right) \\ &\approx f_0 + \mu t'. \end{aligned} \tag{2.6}$$

Here the terms of the time delay are neglected because of the short range assumption $\tau_i(m,t') << T_0$ and $v_i << c$. Then the phase delay of the lth element relative to the 0th element is obtained by

$$\varphi_i^{(l)} = 2\pi f_i(m,t')\frac{ld}{c}\sin\theta_i = 2\pi(f_0 + \mu t')\frac{ld}{c}\sin\theta_i, \tag{2.7}$$

where θ_i denotes the angle of the ith scatterer, $f_i(m,t')$ denotes the instantaneous frequency and is obtained from (2.6), and d denotes the distance between the neighbouring elements, respectively. In this thesis, the targets are located in the far-field and the observation time in one CPI is very short, thus, the angles of the target are assumed constant during one CPI. It is seen in (2.7) that the phase delay is not only related to the element index l, but also the fast-time t'. In fact, it is very straightforward because the steering vector is the function of frequency for wideband DOA and the frequency is the function of fast-time for FMCW signal, then naturally, the steering vector is transferred to a function of time. Therefore, the wideband DOA is decomposed into the narrowband one and an additional second-order coupling between the indices of elements and the fast-time. According to (2.7), the second-order coupling has more significant influence when the relative bandwidth $\frac{B}{f_0}$ is larger. Therefore, for DOA estimation, the wideband term is usually related to the relative bandwidth. This is different from the range estimation, the wideband term is generally related to the absolute bandwidth. Especially for moving objects, wideband is considered when range migration problems happen.

This wideband DOA problem has been ignored in many articles for joint parameters estimation [14,66,67]. Moreover, the traditional CSSM or ISSM for wideband DOA are avoided by solving the problem of coupling terms.

The received signal is then correlated with the conjugate copy of the transmitted signal and the de-chirped signal of the ith scatterer received by lth element can be written as (for simplicity, α_i is still used for denoting the complex amplitude of the de-chirped signal)

$$
\begin{aligned}
z_i^{(l)}(m,t') &= r_i^{(l)}(m,t') \times s^*(m,t') \\
&= \alpha_i e^{\varphi_i^{(l)}} \exp[j2\pi f_0(t'-\tau_i) + 0.5\mu(t'-\tau_i)^2] \\
&\quad \times \exp[-j2\pi(f_0 t' + 0.5\mu t'^2)] \\
&= \alpha_i e^{\varphi_i^{(l)}} \exp[j2\pi(f_0 t' - f_0\tau_i + 0.5\mu t'^2 + 0.5\mu\tau_i^2 \\
&\quad - \mu t'\tau_i - f_0 t' - 0.5\mu t'^2)] \\
&= \alpha_i e^{\varphi_i^{(l)}} \exp[j2\pi(-f_0\tau_i + 0.5\mu\tau_i^2 - \mu t'\tau_i)] \\
&\approx \alpha_i e^{\varphi_i^{(l)}} \exp[-j2\pi(f_0\tau_i - \mu t\tau_i)] \\
&= \alpha_i e^{\varphi_i^{(l)}} \exp\left\{-j2\pi\left[f_0\left(\gamma_i + \frac{2v_i}{c}t' + \frac{2v_i}{c}mT\right)\right]\right\} \\
&\quad \times \exp\left\{-j2\pi\left[\mu t'\left(\gamma_i + \frac{2v_i}{c}t' + \frac{2v_i}{c}mT\right)\right]\right\} \\
&= \alpha_i e^{\varphi_i^{(l)}} \exp\left\{-j2\pi\left[f_0\gamma_i + \left(f_0\frac{2v_i}{c} + \mu\gamma_i\right)t'\right.\right. \\
&\quad \left.\left. + f_0\frac{2v_i}{c}mT + \mu\frac{2v_i}{c}mTt' + \mu\frac{2v_i}{c}t'^2\right]\right\} \\
&\approx \alpha_i e^{\varphi_i^{(l)}} \exp\left\{-j2\pi\left[\left(f_0\frac{2v_i}{c} + \mu\gamma_i\right)t' + f_0\frac{2v_i}{c}mT + \mu\frac{2v_i}{c}mTt'\right]\right\} \\
&\approx \alpha_i \exp\left[j2\pi(f_0 + \mu t')\frac{ld}{c}\sin\theta_i\right] \\
&\quad \times \exp\left[-j2\pi\left(f_0\frac{2v_i}{c}Tm + \mu\gamma_i t'\right)\right] \\
&\quad \times \exp\left[-j2\pi\mu\frac{2v_i}{c}Tmt'\right].
\end{aligned} \tag{2.8}
$$

In the last step, we use the assumption that

$$
\left(f_0\frac{2v_i}{c} + \mu\gamma_i\right)t' \approx \mu\gamma_i t', \tag{2.9}
$$

The assumption that the Doppler frequency is negligible with respect to the beat frequency is appropriate under two conditions. The first one is $f_0\frac{2v_i}{c} \ll \mu\gamma_i$ and the second one is that $f_0\frac{2v_i}{cf_s}$ is much smaller than Nyquist bound 0.5, where f_s is the sampling frequency. This assumption is just for simplicity and works for most scenarios but it is worth noting that it is actually not necessary since combining the frequencies estimated in the fast-time and slow-time, accurate estimations of

the velocity v_i and range R_i are allowed. The issue is mentioned here just to call attention to this assumption, since in another type of waveform, this assumption would bring unpleasant results, which will be discussed again in Appendix B.

After analog-digital converter (ADC) with sampling frequency f_s, the analogous data are discretised as $\mathrm{z}_i^{(l)}$ which is represented as

$$\begin{aligned}\mathrm{z}_i^{(l)}(m,k) = \alpha_i \exp[j2\pi(a(\theta_i)l + f_d(v_i)m + f_r(r_i)k)] \\ \times \exp[j2\pi(f_{\theta r}(\theta_i)lk + f_{dr}(v_i)mk)],\end{aligned} \tag{2.10}$$

where $k = \lfloor t' f_s \rfloor$ is the indices of fast-time samples ($k = 0, 1, 2..., K-1$ and K is the total number of the samples in one PRI), the notations $a(\theta_i) = f_0 \dfrac{d}{c} \sin\theta_i$, $f_d(v_i) = -f_0 \dfrac{2v_i}{c}$, $f_r(r_i) = -\dfrac{\mu}{f_s}\gamma_i$,
$f_{\theta r}(\theta_i) = \mu \dfrac{d}{c f_s} \sin\theta_i$ and $f_{dr}(v_i) = -\mu \dfrac{2v_i}{c f_s} T$ are used to simplify the equation.

The data can be stacked as matrix form for the lth element. Before showing the signal model, we first define the notations of DOA steering vector $\mathbf{a}(\theta_i) \in \mathbb{C}^{L\times 1}$, slow-time sinusoidal vector $\mathbf{f}_d(v_i) \in \mathbb{C}^{M\times 1}$, fast-time sinusoidal vector $\mathbf{f}_r(r_i) \in \mathbb{C}^{K\times 1}$, range migration coupling matrix $\mathbf{\Phi}(v_i) \in \mathbb{C}^{M\times K}$ and wideband DOA coupling matrix $\mathbf{\Psi}(\theta_i) \in \mathbb{C}^{L\times K}$, respectively, as

$$\begin{aligned}\mathbf{a}(\theta_i) &= [1, e^{-j2\pi a(\theta_i)}, ..., e^{j2\pi a(\theta_i)(L-1)}]^T, \\ \mathbf{f}_d(v_i) &= [1, e^{j2\pi f_d(v_i)T}, ..., e^{j2\pi f_d(v_i)T(M-1)}]^T, \\ \mathbf{f}_r(r_i) &= [1, e^{j2\pi f_r(r_i)}, ..., e^{j2\pi f_r(r_i)(K-1)}]^T, \\ \mathbf{\Psi}(\theta_i) &= \begin{pmatrix} \mathbf{h}_0^T(\theta_i) \\ \mathbf{h}_1^T(\theta_i) \\ \vdots \\ \mathbf{h}_{L-1}^T(\theta_i) \end{pmatrix}; \quad \mathbf{\Phi}(v_i) = \begin{pmatrix} \mathbf{g}_0^T(v_i) \\ \mathbf{g}_1^T(v_i) \\ \vdots \\ \mathbf{g}_{M-1}^T(v_i) \end{pmatrix},\end{aligned} \tag{2.11}$$

with $\mathbf{h}_l(\theta_i) \in \mathbb{C}^{K\times 1}$ and $\mathbf{g}_m(v_i) \in \mathbb{C}^{K\times 1}$ as

$$\begin{aligned}\mathbf{h}_l(\theta_i) &= [1, e^{j2\pi l f_{\theta r}(\theta_i)}, ..., e^{j2\pi l f_{\theta r}(\theta_i)(K-1)}]^T, \\ \mathbf{g}_m(v_i) &= [1, e^{j2\pi m f_{dr}(v_i)}, ..., e^{j2\pi m f_{dr}(v_i)(K-1)}]^T.\end{aligned} \tag{2.12}$$

With these notations, the signal model for the lth element is written as

$$\mathbf{Z}_i^{(l)} = \alpha_i \mathrm{a}^{(l)}(\theta_i)(\mathbf{1}_M[\mathbf{h}_l(\theta_i)]^T) \odot (\mathbf{f}_d(v_i)\mathbf{f}_r^T(R_i)) \odot \mathbf{\Phi}_l(v_i), \tag{2.13}$$

where $\mathrm{a}^{(l)}(\theta_i)$ is

$$\mathrm{a}^{(l)}(\theta_i) = \exp\left(j2\pi \frac{ld}{\lambda}\sin\theta_i\right). \tag{2.14}$$

Then the received data of lth element in the presence of the Gaussian noise $\mathbf{N}^{(l)}$ is written as

$$\mathbf{X}^{(l)} = \sum_{i=1}^{I} \mathbf{Z}_i^{(l)} + \mathbf{N}^{(l)}. \tag{2.15}$$

For the following analysis and further algorithm, the data are further represented in a more compact way by stacking the discretised data $\mathrm{z}_i^{(l)}(m,k)$ directly to formulate three dimensional tensor $\boldsymbol{\mathcal{Y}} \in \mathbb{C}^{L\times M\times K}$ for multiple targets in the presence of white Gaussian noise as

$$\boldsymbol{\mathcal{Y}} = \sum_{i}^{I} \alpha_i \mathbf{a}(\theta_i) \circ \mathbf{f}_d(v_i) \circ \mathbf{f}_r(r_i) \odot \boldsymbol{\mathcal{W}}_{\theta r}(\theta_i) \odot \boldsymbol{\mathcal{W}}_{dr}(v_i) + \boldsymbol{\mathcal{N}}, \tag{2.16}$$

where $\boldsymbol{\mathcal{N}} \in \mathbb{C}^{L\times M\times K}$ is the complex Gaussian noise tensor with distribution $\mathcal{CN}(0,\sigma^2)$, $\boldsymbol{\mathcal{W}}_{\theta r}(\theta_i) \in \mathbb{C}^{L\times M\times K}$ is the wideband DOA coupling tensor and $\boldsymbol{\mathcal{W}}_{dr}(v_i) \in \mathbb{C}^{L\times M\times K}$ is the range migration coupling tensor of ith target, respectively. Let $[\boldsymbol{\mathcal{P}}(\theta_i)]_{l,0,k} = [\boldsymbol{\Psi}(\theta_i)]_{l,k} \in \mathbb{C}^{L\times 1\times K}$, which means adding a new axis between the row and the column of $\boldsymbol{\Psi}(\theta_i)$ to make it as a three-dimensional tensor $\boldsymbol{\mathcal{P}}(\theta_i)$ (illustrated ib Fig. 2.3), then $\boldsymbol{\mathcal{W}}_{\theta r}(\theta_i)$ and $\boldsymbol{\mathcal{W}}_{dr}(v_i)$ have the form

$$\begin{aligned} \boldsymbol{\mathcal{W}}_{\theta r}(\theta_i) &= \boldsymbol{\mathcal{P}}(\theta_i) \times_2 \mathbf{1}_M^T, \\ \boldsymbol{\mathcal{W}}_{dr}(v_i) &= \mathbf{1}_L \circ \boldsymbol{\Phi}(v_i). \end{aligned} \tag{2.17}$$

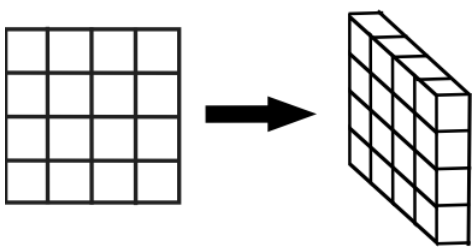

Figure 2.3: Illustration of adding a new axis to make 2D a matrix as 3D tensor

Then the problem is to estimate the parameters θ_i, v_i and R_i for all I point targets from the tensor data $\boldsymbol{\mathcal{Y}}$, where the cubic data $\boldsymbol{\mathcal{Y}}$ are indexed with the array element indices $l = 0, 1, ..., L-1$, slow-time indices $m = 0, 1, ..., M-1$ and fast-time sampling indices $k = 0, 1, ..., K-1$.

2.2.2. UNAMBIGUOUS PARAMETERS

According to (2.8) and Nyquist criterion, the maximum unambiguous angle θ_{max}, Doppler velocity v_{max} and range R_{max} are determined by $a(\theta_i) \in [-0.5, 0.5)$,

$f_d(v_i) \in [-0.5, 0.5)$ and $f_r(r_i) \in [0, 1)$ as

$$\begin{aligned} \sin(\theta_{\max}) &= \min\left\{\frac{c}{2f_0 d}, 1\right\}, \\ v_{\max} &= \frac{c}{4Tf_0}, \\ R_{\max} &= \frac{cK}{2B} = K\Delta r, \end{aligned} \tag{2.18}$$

where $\Delta r = \dfrac{c}{2B}$ is the theoretical range resolution. Here we assume that the azimuthal angles of the targets are within the unambiguous domain and it is usually realised by setting the distance of neighbouring antenna as $d = \dfrac{c}{2f_0} = \dfrac{\lambda}{2}$ to cover the whole azimuthal domain unambiguously, where $\lambda = \dfrac{c}{f_0}$ is the wavelength of the starting frequency. If the Doppler velocity v_i is larger than the maximum unambiguous velocity $v_{\max}$, it will be folded into the unambiguous domain of the sinusoidal components $f_d(v_i)$ according to

$$v_i = 2n_i v_{\max} + \hat{v}_i \tag{2.19}$$

where $|\hat{v}_i| < |v_{\max}|$ is the folded velocity and n_i is the integer fold number. Estimation of velocity from $f_d(v_i) = f_d(\hat{v}_i)$ would only yield the folded velocity $\hat{v}_i$, while the information of the Doppler ambiguity can be extracted from the coupling component $f_{dr}(v_i)$. Here we assume that the $|f_{dr}(v_i)| < 0.5$ to avoid coupling term ambiguity and it is usually satisfied in most applications when $|v_i| < \dfrac{cf_s}{4B}$ holds.

According to (2.18), the constraint between $v_{\max}R_{\max}$ and the sampling frequency f_s has

$$v_{\max}R_{\max} \leq \frac{c^2}{8Bf_0} f_s, \tag{2.20}$$

where $\dfrac{c^2}{8Bf_0}$ is a constant determined by the radar system. For a given system, $v_{\max}R_{\max}$ is bounded by the sampling frequency f_s. Eq. (2.20) indicates that for UWB FMCW radar, large $v_{\max}$ and $R_{\max}$ are usually hard to achieve simultaneously using the low-cost hardware (low sampling frequency). Such constraint limits the application of UWB FMCW radar in many industrial fields. For example, to simultaneously achieve $v_{\max} = 100$m/s and $R_{\max} = 200$m for 77GHz automotive radar with 4GHz bandwidth, the sampling frequency of at least 500MHz is required. Moreover, higher sampling frequency implies a larger amount of data to be collected and processed in a limited time interval, which is computationally heavy and

memory-consuming. To alleviate the burden on the hardware, a possible way is to relax the maximum unambiguous velocity $v_{\max}$ and recover the true ambiguous velocity $|v_i| > |v_{\max}|$ from the coupling term $f_{dr}(v_i)$.

2.3. CONCLUSIONS

In this chapter, the fundamental concepts of CW, FMCW and de-chirping techniques are reviewed and the signal model for multiple moving point targets in high-resolution FMCW radar has been introduced, which will be used in the following chapters. Different from the narrowband cases, the presented signal model not only contains the sinusoidal components whose frequencies are corresponding to the parameters, but also the mutual coupling terms which are brought by range migration and wideband DOA. Therefore, the frequency estimator for conventional narrow signals cannot be applied directly. This problem is one of the main challenges of the whole thesis and a number of novel algorithms to eliminate or take advantages of these terms are introduced in the following chapters.

3

JOINT PARAMETERS ESTIMATION USING COMPENSATED MUSIC ALGORITHM

The joint DOA, Doppler and range estimation of moving point-like targets using the derived signal model in the previous chapter is investigated and the compensated MUSIC algorithm is proposed in this chapter. Based on the signal model in Chapter 2, 2D MUSIC algorithm is firstly adopted for joint estimation of Doppler and DOA by ignoring the coupling terms. Then a novel embedded compensation approach is applied to adjust the phases to improve the accuracy and resolution of the estimation. After that, an original efficient implementation of the proposed algorithm is introduced, and the relevant performances are compared with other algorithms. In spite of the heavy computational load, the same compensation approach is further applied to 3D MUSIC in which the noise subspace is extracted by tensor decomposition. Finally, numerical simulations are used to validate the performance of the proposed methods. It is shown that the performance of the proposed compensated 2D MUSIC has higher accuracy and resolution than that of Keystone MUSIC. In addition, it is shown that for a small number of targets, the Rayleigh-Ritz is the most efficient approach among its counterparts. In addition, the proposed compensation method also shows positive results in 3D MUSIC simulation.

3.1. INTRODUCTION

Although both range migration and wideband DOA estimation are intensively studied separately, there are few articles addressing both problems simultaneously. In this chapter, a MUSIC-based algorithm is proposed for the problem of joint Doppler and DOA estimation using the signal model from the previous chapter considering both range migration and wideband DOA issues. The range migration model has been studied comprehensively and presented as the second-order coupling between fast-time and slow-time. Combine the fact that the steering vector is the function of the frequency of wideband DOA and the frequency is the function of fast-time in FMCW signal, the conventional CSSM and ISSM can be avoided by transforming the steering vector into the function of fast-time. Thus, the wideband DOA problem is transformed to the inter coupling between the fast-time and the element indices analogue to the range migration problem. By this transform, both range migration and wideband DOA problem present as coupling terms and can be eliminated in the same way. Borrowing the signal model from the previous chapter, the classic 2D MUSIC-based algorithm for joint estimation of Doppler and DOA is presented. Unfortunately, conventional 2D MUSIC algorithm cannot correctly estimate the parameters in the presence of the couplings. To eliminate the influence of the coupling terms for accurate parameters estimation, a phase compensation method is proposed for both couplings of range migration and wideband DOA. The compensation method needs, however, multiple large-size matrix eigendecompositions which are computationally intensive. Therefore, two efficient implementations, namely the Lanczos algorithm and Rayleigh-Ritz step, are introduced. We compare the two proposed methods with the inverse method, which is also a general MUSIC accelerating approach presented in [66].

The proposed 2D MUSIC could only estimate two-dimensional parameters simultaneously by averaging one-dimensional data to formulate the covariance matrix. Thus, 2D MUSIC has to be applied at least twice to estimate the three-dimensional parameters. In spite of the computational loads, the compensation algorithm is extended to 3D MUSIC as well in this chapter, where different from eigendecomposition-based 2D MUSIC, the noise subspace is obtained by tensor decomposition.

A series of numerical simulations are performed and the results are presented to demonstrate the applicabilities and the advantages of the proposed algorithms.

The rest of the chapter is organised as follows. In Section 3.2, the classic 2D MUSIC is applied to joint estimation of Doppler and DOA. Then, the compensation algorithm is proposed. The efficient implementations are introduced and compared in Section 3.3. The 3D MUSIC algorithm is further presented in 3.4. Simulation results are presented in Section 3.5 and conclusions are drawn in Section 3.6.

3.2. 2D MUSIC ALGORITHM AND COMPENSATION METHOD

In this section, the classic 2D MUSIC algorithm for joint estimation of DOA and Doppler is presented first. However, the coupling terms decrease the performance of classic 2D MUSIC. In order to circumvent this a novel compensation method is proposed in the MUSIC algorithm to remove such interference. The estimation of the model order is discussed at last in this section.

3.2.1. 2D MUSIC ALGORITHM

With the low-rank 3D data model, it is possible to apply the MUSIC algorithm for joint parameter estimation if we ignore the coupling terms. Using one dimension of sinusoidal data as reference, the 2D MUSIC algorithm can be implemented for joint two-dimensional parameter estimation. The 3D MUSIC algorithm can be further used for joint three-dimensional parameters estimation for DOA, range and Doppler. The noise subspace can be extracted by applying a spatial smoothing technique to eliminate coherence between the sources [68] or by applying a high order singular value decomposition (HOSVD) [69]. However, it is both time- and memory-consuming to directly apply the 3D MUSIC algorithm. Despite such a problem, we extend the proposed algorithm to the 3D case with tensor decomposition later. Here, the 2D MUSIC algorithm is applied first, for instance, to estimate Doppler and DOA jointly. It is worth noting that, the proposed methods can also be applied for joint estimation of Doppler and range or DOA and range. To apply the 2D MUSIC algorithm, the raw data has to be reshaped from the 3D tensor data to the 2D matrix $\mathbf{Y} \in \mathbb{C}^{LM \times K}$ (where L is the number of the antenna elements, M is the number of chirps in one CPI and K is the number of samples for each chirp) by stacking element and slow-time dimensions together from 2.15 as

$$\mathbf{Y} = \begin{pmatrix} \mathbf{X}^{(0)} \\ \mathbf{X}^{(1)} \\ \vdots \\ \mathbf{X}^{(L-1)} \end{pmatrix}. \tag{3.1}$$

For simplicity, $\mathbf{Y}$ is rewritten in matrix notation as:

$$\mathbf{Y} = \sum_{i}^{I} \alpha_i \mathbf{a}(\theta_i \otimes \mathbf{f}_d(v_i)) \mathbf{f}_r^T(R_i) \odot \mathbf{\Omega}_{dr}(v_i) \odot \mathbf{\Omega}_{\theta r}(\theta_i) + \mathbf{N}, \tag{3.2}$$

where $\mathbf{\Omega}_{dr}(v_i) \in \mathbb{C}^{LM \times K}$ and $\mathbf{\Omega}_{\theta r}(\theta_i) \in \mathbb{C}^{LM \times K}$ are given by,

$$\begin{aligned} \mathbf{\Omega}_{dr}(v_i) &= \mathbf{1}_L \otimes \mathbf{\Phi}(v_i), \\ \mathbf{\Omega}_{\theta r}(\theta_i) &= \mathbf{\Psi}(\theta_i) \otimes \mathbf{1}_M \end{aligned} \tag{3.3}$$

Now, the classic 2D MUSIC algorithm is applied directly by ignoring the coupling terms. First, the covariance matrix $\mathbf{R} \in \mathbb{C}^{LM \times LM}$ averaging on fast-time is computed according to

$$\mathbf{R} = \mathbb{E}(\mathbf{Y}\mathbf{Y}^H). \tag{3.4}$$

The eigendecomposition is applied to split the data space into the noise subspace $\mathbf{U_n}$ associated to the noise eigenvectors and the signal subspace $\mathbf{U_s}$ associated to the signal eigenvectors.

$$\begin{aligned} \mathbf{R} &= \mathbf{U}\mathbf{\Lambda}\mathbf{U}^H, \\ \mathbf{U} &= [\mathbf{U_s}\ \mathbf{U_n}]. \end{aligned} \tag{3.5}$$

To extract the noise subspace we assume that the number of the scatterers is known. The estimation of the number of scatterers will be discussed later. The matched steering vector $\boldsymbol{\alpha}(v_p, \theta_q) \in \mathbb{C}^{LM \times 1}$ for the velocity v_p and the angle θ_q is formulated as

$$\boldsymbol{\alpha}(v_p, \theta_q) = \mathbf{a}(\theta_q) \otimes \mathbf{f}_d(v_p). \tag{3.6}$$

After that, the MUSIC spectrum at the point (v_p, θ_q) can be calculated by

$$P(v_p, \theta_q) = \frac{1}{\boldsymbol{\alpha}^H(v_p, \theta_q)\mathbf{U_n}\mathbf{U_n}^H\boldsymbol{\alpha}(v_p, \theta_q)}. \tag{3.7}$$

3.2.2. COMPENSATION FOR COUPLING TERMS

Directly applying the classic MUSIC algorithm without any phase compensation yields an estimation performance that is significantly inaccurate due to the influence of the coupling terms. Hence, phase adjustment is needed before the MUSIC algorithm is applied. Although the Keystone transform is the most common approach for the coupling term adjustment, the interpolation of the Keystone transform leads to significant phase errors when the data size is small [18, 70]. Despite this drawback, the performance of Keystone transform will be discussed and compared with the proposed algorithm in Section 3.5.

Fortunately, since the coupling terms are functions of v for $\mathbf{\Omega}_{dr}(v_i)$ and θ for $\mathbf{\Omega}_{\theta r}(\theta_i)$, we are able to remove the coupling terms in each scanning grid. The compensation term for the grid in terms of (v_p, θ_q) is formulated as

$$\mathbf{C} = (\mathbf{\Omega}_{dr}(v_p) \odot \mathbf{\Omega}_{\theta r}(\theta_q))^*. \tag{3.8}$$

Then by Hadamard product with the raw data matrix $\mathbf{Y}$ yields

$$\hat{\mathbf{Y}} = \mathbf{Y} \odot \mathbf{C}. \tag{3.9}$$

Since the compensation term is just a phase shift, it will not increase the noise power. The coupling terms of the new obtained data are removed for the grid in terms of (v_p, θ_q).

With this compensation, not only the phase is adjusted to improve the accuracy, but also the orthogonality between the steering vector and the noise subspace is enhanced which helps to improve the resolution. The covariance matrix averaging on fast-time is calculated using the improved data $\hat{\mathbf{Y}}$ according to

$$\hat{\mathbf{R}} = \mathbb{E}(\hat{\mathbf{Y}}\hat{\mathbf{Y}}^H). \tag{3.10}$$

Finally, the 2D MUSIC algorithm (3.7) can be applied to the improved covariance matrix.

Fig. 3.1 explains how the compensation influences the orthogonalities between steering vector and the extracted "*noise subspace*" with two rank-one targets. Fig. 3.1(a) illustrates the situation when there are no coupling terms, where the steering vectors are formulated with same amplitude in the above graph and the data are decomposed into noise subspace (indicated by grey colour) and signal subspace (indicated by red and green colour) in the below graph. The signal subspace is the span of the rank-one components corresponding to the targets and therefore, the steering vectors of such targets are orthogonal to the noise subspace, that is why the targets could be found in the mismatch position between the steering vectors and the noise subspace.

Fig. 3.1(b) shows that when the coupling terms are present, the targets cannot be expressed as rank-one components any longer. This explains that when the data are projected on the eigenspace, part of the energies corresponding to the targets will leak into the "*noise subspace*". Thus, the reason for ill-performance of conventional MUSIC is that the steering vectors of the targets are non-orthogonal to the extracted "*noise subspace*".

Fig. 3.1(c) and Fig. 3.1(d) illustrate how the proposed approach improves the orthogonalities between the steering vectors and the "*noise subspace*". When the MUSIC algorithm scans the grid which is the location of the red target, the compensation adjusts the phase and makes the red target as the rank-one component regardless of the green target. Such adjustments lead to the fact that all the energy of the red target will be projected onto the "*signal subspace*" and the steering vector of the red targets are completely orthogonal to the "*noise subspace*" even if it contains the part of the energy of the green target. The same story will occur to the green target when the algorithm scans its location.

According the analysis above, the algorithm is concluded in **Algorithm** 1 (**A**1).

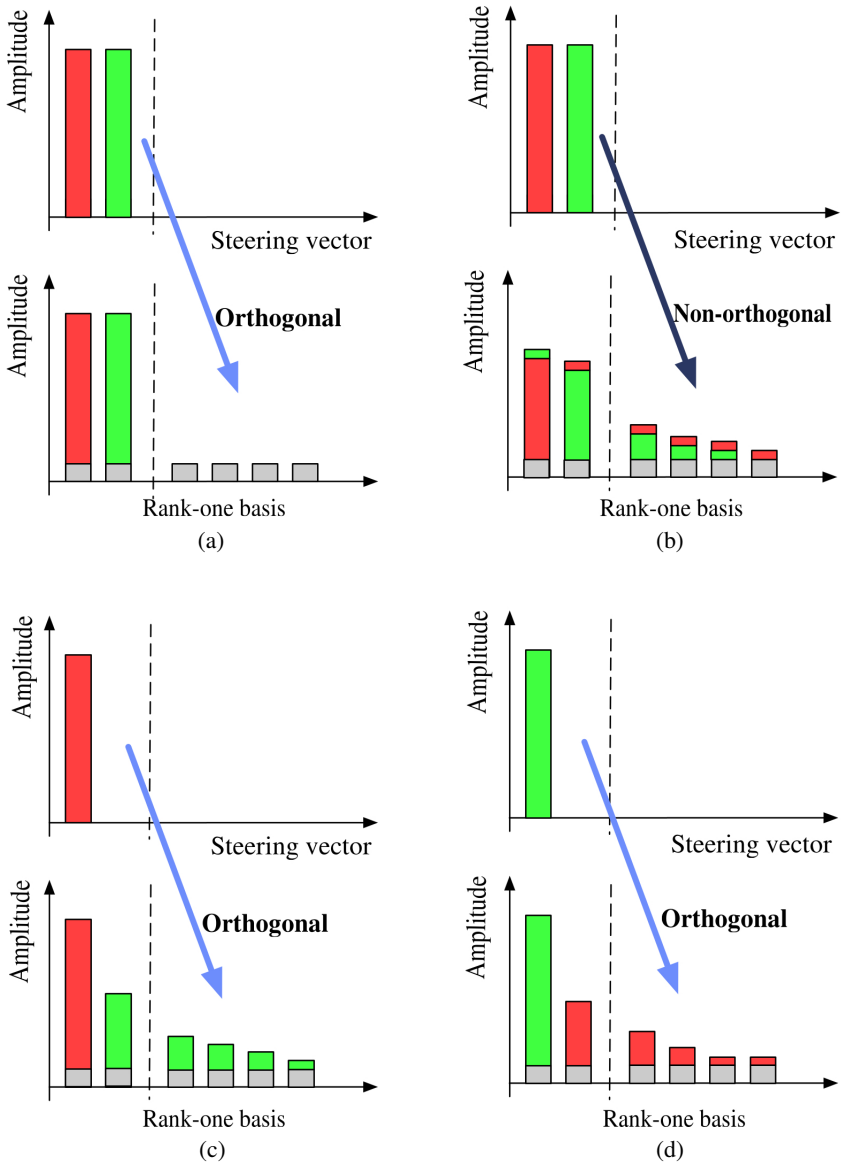

Figure 3.1: Illustration of orthogonality betweem the noise subspace and the steering vectors for (a) without couplings, (b) with couplings, (c) coupling compensation for the red target and (d) coupling compensation for the red target.

Algorithm 1 2D MUSIC with Compensation (**A**1)

Reshape the raw data as (4.19)
for v_p in $[-v_m, v_m]$ **do**
  for θ_q in $[-\theta_m, \theta_m]$ **do**
    $\mathbf{C} = (\mathbf{\Omega}_{dr}(v_p) \odot \mathbf{\Omega}_{\theta r}(\theta_q))^*$
    $\hat{\mathbf{Y}} = \mathbf{Y} \odot \mathbf{C}$
    $\hat{\mathbf{R}} = \mathbb{E}(\hat{\mathbf{Y}}\hat{\mathbf{Y}}^H)$
    $\hat{\mathbf{R}} = \mathbf{U}\mathbf{\Lambda}\mathbf{U}^{-1}$ # Eigendecomposition
    $\mathbf{U_n} = \mathbf{U}[:, I : end]$ # I is the number of targets
    $\boldsymbol{\alpha}(v_p, \theta_q) = \mathbf{a}(\theta_q) \otimes \mathbf{f}_d(v_p)$
    $P(v_p, \theta_q) = \dfrac{1}{\boldsymbol{\alpha}^H(v_p, \theta_q)\mathbf{U_n}\mathbf{U_n}^H\boldsymbol{\alpha}(v_p, \theta_q)}$
  end for
end for

3.2.3. ESTIMATION OF THE TARGET NUMBER

Before implementing the 2D MUSIC algorithm, the number of targets has to be estimated to correctly extract the noise subspace. Apparently, the coupling terms in (3.2) bring difficulties to estimate the number of the targets, since the eigenvalues decrease more smoothly than that of the narrowband model. Therefore, a novel method is proposed for the estimation of the number of targets involved. Usually, the number of targets is much smaller than the dimension of the covariance matrix, so the signal subspace is allowed to be slightly overestimated. Another important fact is that the "*noise subspace*" is dynamic with searching grid, the correct signal component could adaptively project onto the "*signal space*" to guarantee the orthogonality between the steering vector and the "*noise subspace*". According to this property, a larger model order than the true one can be selected first to image the MUSIC pseudo-spectrum. Then by using peaks detection methods we estimate the number of the targets from the MUSIC pseudo-spectrum for simplicity. Although it is allowed to assume the larger dimension of the signal subspace than the true one, it provides better imaging results by using the whole noise subspace. After we obtain the number of targets, the proposed algorithms can be applied to obtain better estimation. The simulations of such a method will be shown in Section 3.5.1.

3.3. EFFICIENT IMPLEMENTATION OF COMPENSATED 2D MUSIC

The proposed algorithm, however, needs multiple eigendecompositions of large matrices, which is unacceptable in automotive applications. In this section, an efficient implementation of the proposed methods without loss of the performance is intro-

duced by accelerating extraction of the noise subspace and parallel implementation.

3.3.1. EFFICIENT IMPLEMENTATION FOR THE NOISE SUBSPACE EXTRACTION

As for 2D MUSIC, the dimension of the covariance matrix $LM \times LM$ is usually very large. Thus, it is a heavy computational burden to perform all the eigendecompositions for each scanning grid and limits the proposed method for real applications. Fortunately, as the covariance is a Hermitian matrix, some properties of the algorithm allow opportunities to accelerate the algorithm. The first one is that the number of targets is usually much smaller than the dimension of the covariance matrix. Instead of calculating all eigenvectors, one can only calculate the needed eigenvectors in the signal space, while the noise subspace can be easily obtained from the orthogonal complement subspace of the signal subspace according to

$$\mathbf{U_n}{\mathbf{U_n}}^H = \mathbf{I} - \mathbf{U_s}{\mathbf{U_s}}^H. \tag{3.11}$$

Another interesting property is that the compensation term is just a minor phase shift. Therefore, the norm distances of the signal subspaces in each adjacent grids are close to each other. Based on these properties, two acceleration methods are introduced, namely the Lanczos algorithm and the Rayleigh-Ritz step. The inverse approach in [66] is also mentioned for comparison.

LANCZOS ALGORITHM

The Lanczos algorithm is an iterative method for calculating the eigendecomposition of large Hermitian/symmetric matrices [71]. It saves a lot of computation by only computing the largest eigenvalues and their corresponding eigenvectors. Thus, it can be used in scenarios where only the signal subspace is required and the dimension of the signal subspace is much smaller than the dimension of the covariance matrix.

RAYLEIGH-RITZ STEP

Lanczos is much faster to extract the signal subspace than the default eig function (in NumPy or MATLAB) if the dimension of the signal subspace is small. However, it is not fast enough and we do not take advantage of the fact that the adjacent signal subspaces are close to each other in the norm distance. The signal subspaces for neighbouring grids are close to each other in the norm distance so the previous signal subspace provides a good initial guess to calculate the next one. Thus, the Rayleigh-Ritz step method [72] is adopted to use the previous signal subspace as the initial guess to approach the current signal subspace. According to the simulation, just one step is needed to obtain a sufficiently good eigenvector approximation.

Table 3.1: Computational Complexity

Algorithm	Computational complexity
Default eig Func	$\mathcal{O}(n^3)$
Inverse	$\mathcal{O}(\frac{1}{3}n^3)$
Lanczos	$\mathcal{O}(\beta n^2)$
Rayleigh-Ritz	$\mathcal{O}(\beta^2 n + \beta^3)$

INVERSE ALGORITHM WITHOUT EVD

In [66], the authors proposed to use the inverse of the covariance matrix to replace the noise subspace. Certainly, calculating the inverse or pseudo-inverse of a huge matrix will save a lot of time compared to calculating the eigendecomposition, and shows comparable results with MUSIC but is faster than eigendecomposition MUSIC. However, this method can only work in high SNR condition. If the SNR is low, the approximation of this method is no longer valid. Moreover, the convergence performance of matrix inverse/pseudo-inverse is not monotonically increasing with the snapshot/SNR [73]. Thus this algorithm is not stable and robust. Despite its disadvantages, from the computational burden and estimation performance perspectives, we use this algorithm as a reference to compare it with our proposed algorithms.

COMPARISON

To compare the performance of selected methods on computation time, we first fix the dimension of the covariance matrix and measure the time consumption with the different number of eigenvectors associated to the largest eigenvalues. The simulation results with a mean time of 100 repeats using Python3.5 with SciPy0.19 under Intel(R) Core i5-6500 @ 3.20GHz is shown in Fig. 3.2(a). (It is worth noting that the results using MATLAB could be different.)

The computation time is not only influenced by the number of eigenvectors associated to the largest eigenvalues, but also by the dimension of the covariance matrix. Thus, the comparison of time consumption with different dimensions of the covariance matrix is shown in Fig. 3.2(b). As we can see, the computation time of the default eig function increases significantly with the dimension of the covariance matrix as it needs $\mathcal{O}(n^3)$ flops (float number operations). The Rayleigh-Ritz step shows to be the most efficient method among all of them.

The computational complexity is shown in Table 3.1, where n represents the dimension of the Hermitian matrix and β represents the number of eigenvectors associated to the β largest eigenvalues.

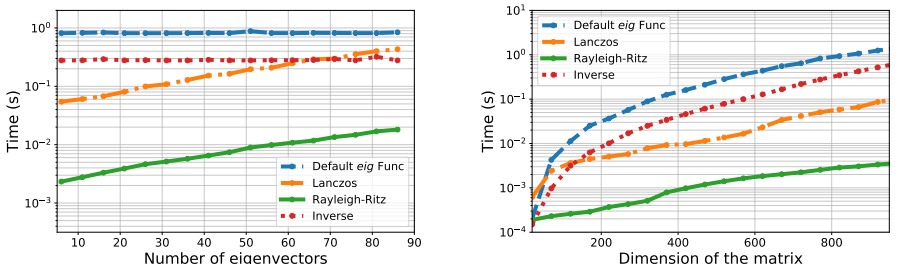

(a) (b)

Figure 3.2: Time consumption comparison for (a) calculating the different number of eigenvectors with the same dimension of the Hermitian matrix of 768×768 and (b) calculating 10 eigenvectors with the different dimension of the Hermitian matrix

According to the above analysis, using the Rayleigh-Ritz step as an example, the algorithm can be illustrated as **Algorithm** 2 (**A**2).

3.3.2. PARALLEL PROCESSING

As the 2D MUSIC algorithm is a scanning process, it is possible to divide the scanning domain into several parts related to CPU cores for parallel processing. We can process each part parallelly to fully utilise the hardware. Here, by using a *threading* package in python3.5, we divide the scanning domain into 4 parts with identical size and by using covariance matrix size of 256×256, the computational time with and without parallel computing are 25.8 seconds and 41.9 seconds, respectively. In the simulation, 62% of the computational time is saved by using parallel processing.

3.4. 3D MUSIC ALGORITHM WITH TENSOR DECOMPOSITION

Previous sections discussed to reduce the range dimension as the reference dimension to extract the noise subspace. So at least two times such MUSIC algorithm has to be performed to obtain three-dimensional parameters. In this section, the proposed compensation algorithm is extended to 3D MUSIC. However, only one-dimensional compensation on velocity is present by ignoring the wideband DOA problem in the algorithm for simplicity. This makes sense since the wideband DOA and range migration have a similar mathematical expression in the signal model and could share the solutions.

As we know, one of the key step of the MUSIC algorithm is the extraction of the noise subspace. Usually, the spatial smoothing technique is applied to obtain the smoothed covariance matrix to increase the detectability of the coherent

Algorithm 2 Compensation algorithm with Rayleigh-Ritz step (**A**2)

Reshape the raw data $\mathbf{Y}$ as (3.1)
$\mathbf{R} = \mathbb{E}(\mathbf{Y}\mathbf{Y}^H)$
$\mathbf{R} = \mathbf{U}\mathbf{\Lambda}\mathbf{U}^H$ # Eigendecomposition
$\mathbf{U_s} = \mathbf{U}[:, 0 : I-1]$
for v_p in $[-v_m, v_m]$ **do**
    $\hat{\mathbf{Y}} = \mathbf{Y} \odot (\mathbf{\Omega}_{dr}(v_p))^*$
    for θ_q in $[-\theta_m, \theta_m]$ **do**
        $\hat{\mathbf{Y}} = \hat{\mathbf{Y}} \odot (\mathbf{\Omega}_{\theta r}(\theta_i))^*$
        $\hat{\mathbf{R}} = \mathbb{E}(\hat{\mathbf{Y}}\hat{\mathbf{Y}}^H)$
        $\mathbf{Z} = \hat{\mathbf{R}}\mathbf{U_s}$
        $\mathbf{Z} = \mathbf{Q}\mathbf{P}$ # QR decomposition
        $\mathbf{H} = \mathbf{Q}^H\hat{\mathbf{R}}\mathbf{Q}$
        $\mathbf{H} = \mathbf{F}\mathbf{\Theta}\mathbf{F}^H$ # Eigendecomposition
        $\mathbf{U_s} = \mathbf{Q}\mathbf{F}$
        $\boldsymbol{\alpha}(v_p, \theta_q) = \mathbf{a}(\theta_q) \otimes \mathbf{f}_d(v_p)$
        $P(v_p, \theta_q) = \dfrac{1}{\boldsymbol{\alpha}^H(v_p, \theta_q)(\mathbf{I} - \mathbf{U_s}\mathbf{U_s}^H)\boldsymbol{\alpha}(v_p, \theta_q)}$
    end for
end for

sources. However, the usage of spatial smoothing decreases the effective raw data size. Tensor decomposition (TD) is adopted here to extract the noise subspace to avoid this side effect and the process of TD is illustrated in Fig. 3.3. Unlike the method in [74], in which the author formulates the multi-dimensional covariance matrix, TD is directly performed. Here, the number of sources are assumed to be known as I. In fact, although the rank-one components of TD are not mutually orthogonal, they could represent the whole signal subspace. The orthogonalisation process is applied to orthogonalise and unitise these components. Next, the noise subspace can be easily obtained from orthogonal complement subspace of the signal subspace. However, the received signals cannot be extracted exactly as rank-one components due to the coupling terms in the data model. Thus, compensation is made before TD to adjust the phase of the signal reflection of one target to a rank one component. As the targets with different velocity have different coupling phase residuals, the compensation has to be implemented in each velocity bin. Therefore, the velocity term is chosen as the first scanning domain to reduce computational complexity.

The compensation term for the coupling at the velocity scanning bin v_p is written as coupling component $\boldsymbol{\mathcal{D}} \in \mathbb{C}^{L\times M\times K}$ as

$$\boldsymbol{\mathcal{D}} = \mathbf{1}_L \circ \boldsymbol{\Omega}_p^{dr} \tag{3.12}$$

Then multiply the conjugate compensation term with raw data elementwisely as

$$\hat{\boldsymbol{\mathcal{Y}}} = \boldsymbol{\mathcal{Y}} \odot \boldsymbol{\mathcal{D}}^* \tag{3.13}$$

The new data, where the coupling term is removed for the velocity v_p are obtained. Then the range and angle scanning can be performed in the current velocity grid.

After removing the phase residual in velocity bin v_p, TD is applied to extract I rank-one component. It is worth noting that these rank-one components cannot represent all the targets signal subspace. Only the targets with velocity v_p, whose phase residuals are compensated, are rank-one component among them.

Then by Kronecker product and orthogonalisation process, the signal subspace is formed as the unit orthogonal column matrix. After that, the noise subspace is obtained by orthogonal projection as

$$\mathbf{U}_n\mathbf{U}_n^H = \mathbf{I} - \mathbf{U}_s\mathbf{U}_s^H, \tag{3.14}$$

where $\mathbf{I}$ is the identity matrix and the noise subspace extraction is illustrated in Fig. 3.4. The steering function vector is formulated for scanning bin $[\theta_p, v_q, r_h]$ as

$$\boldsymbol{\alpha} = \mathbf{a}(\theta_p) \otimes \mathbf{f}_d(v_q) \otimes \mathbf{f}_r(r_h). \tag{3.15}$$

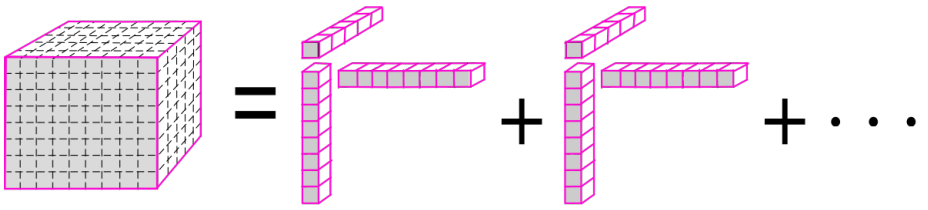

Figure 3.3: Illustration of Tensor Decomposition

The MUSIC spectrum is

$$\boldsymbol{\mathcal{P}}_{p,q,h} = \frac{1}{\boldsymbol{\alpha}^H(\mathbf{I} - \mathbf{U_s}\mathbf{U_s}^H)\boldsymbol{\alpha}}. \tag{3.16}$$

Above all, the algorithm is concluded in **Algorithm** 3 (**A**3).

Algorithm 3 compensated 3D TD-MUSIC (**A**3)

for v_p in $[-v_m, v_m]$ **do**
  $\hat{\boldsymbol{\mathcal{Y}}} = \boldsymbol{\mathcal{Y}} \odot \boldsymbol{\mathcal{D}}^*$
  $\hat{\boldsymbol{\mathcal{Y}}} = \sum_i^I \mathbf{a}_i \circ \mathbf{b}_i \circ \mathbf{c}_i$ # Tensor Decomposition
  $\mathbf{U}_s(i) = \mathbf{a}_i \otimes \mathbf{b}_i \otimes \mathbf{c}_i$
  $\mathbf{U}_s(i) = \dfrac{\mathbf{U}_s(i)}{||\mathbf{U}_s(i)||}$
  $\mathbf{U}_s = \mathbf{orth}(\mathbf{U}_s)$ # Orthogonalisation
  $\mathbf{U}_n\mathbf{U}_n^H = \mathbf{I} - \mathbf{U}_s\mathbf{U}_s^H$
  for θ_q in $[-\theta_m, \theta_m]$ **do**
    for r_h in $[0, R_m]$ **do**
      $\boldsymbol{\alpha} = \mathbf{a}(\theta_q) \otimes \mathbf{f}_d(v_p) \otimes \mathbf{f}_r(r_h)$
      $\boldsymbol{\mathcal{P}} = \dfrac{1}{\boldsymbol{\alpha}^H(\mathbf{I} - \mathbf{U_s}\mathbf{U_s}^H)\boldsymbol{\alpha}}$
    end for
  end for
end for

3.5. SIMULATIONS

In this section, a group of numerical simulations are presented to demonstrate the performance of the proposed methods.

3.5.1. 2D MUSIC

As the coupling term is related to the bandwidth, the performance of the proposed methods with different bandwidths, i.e. 1 GHz and 4 GHz, will be simulated. The

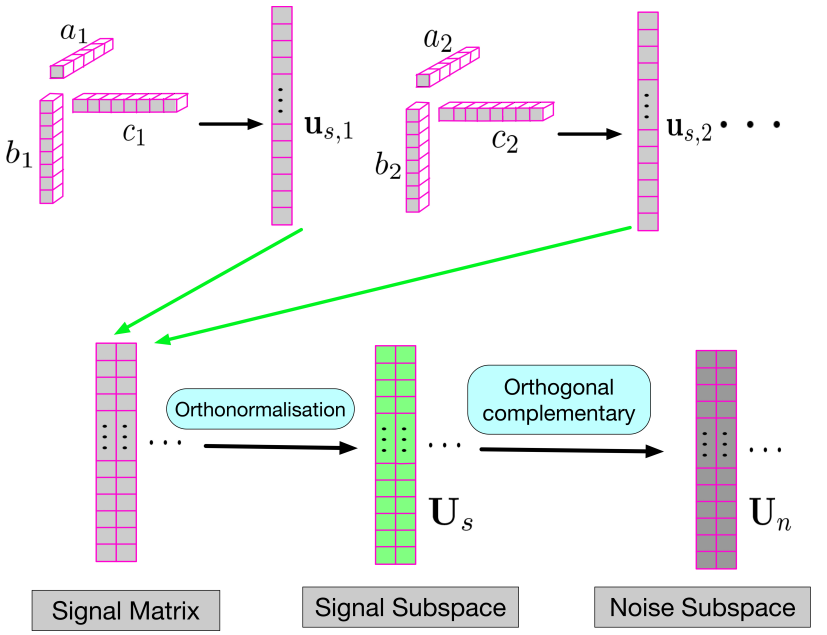

Figure 3.4: Formulation of noise subspace with tensor components

other system parameters used for simulation are shown in Table 3.2.

Table 3.2: Parameters of the System

Parameters	Value
Number of chirps in one CPI	16
Number of samples in one Chirp	32
Number of antenna elements	8
Starting Frequency	77 GHz
Inter-element distance	1.899 mm
Chirp repetition interval	0.1 ms
Chirp duration	0.09 ms

BANDWIDTH 1 GHz

We start with considering a case with a bandwidth of $B = 1\,\mathrm{GHz}$, where the relative bandwidth is 1.3%. Fig. 3.5 shows the root-mean-square errors (RMSEs) of estimates of DOA and Doppler of a single point scatterer with the radial velocity $8\,\mathrm{m/s}$, angle $40°$ and range $80\,\mathrm{m}$ as a function of the SNR. They are compared with the corresponding CRB (see Appendix for CRB derivation). The RMSEs are obtained from 40 Monte Carlo trials. As classic MUSIC is a biased estimator, the

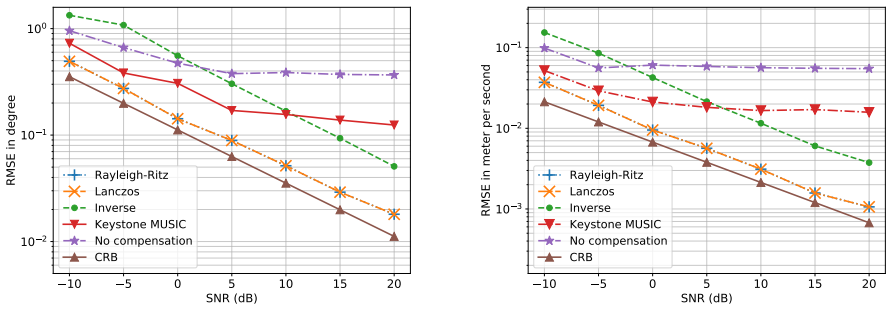

(a) (b)

Figure 3.5: Comparison of RMSEs with CRB as a function of SNR at $B = 1\,\mathrm{GHz}$ for one target at angle 40° and velocity $8\,\mathrm{m/s}$. (a) angle estimation and (b) velocity estimation

RMSEs will not decrease with the increase of SNR. One can also observe that the RMSEs of the Keystone MUSIC do not always decrease along with the increase of the SNR since the error introduced by the interpolation will dominantly decrease the accuracy of the estimation at high SNR condition.

We further focus on the performance of the proposed methods in a challenging scenario. To this end, four closely positioned point scatterers with the same angles $\theta = 45^\circ$ and the same amplitudes $0\,\mathrm{dB}$, but close radial velocities $v = [4.6, 5.68, 6.86, 7.91]\,\mathrm{m/s}$ and random range from $100\,\mathrm{m}$ to $200\,\mathrm{m}$ are set. The SNR is set to $3\,\mathrm{dB}$. The normalised results are shown in Fig. 3.6.

MUSIC with phase compensation (in both Lanczos and Rayleigh-Ritz acceleration implementations) achieves at least -3 dB isolation between the scatterers, while the inverse method and the classic MUSIC algorithm without phase compensation are not able to separate scatterers from each other. The Keystone-MUSIC (Fig. 3.6(b)) shows some separation of the scatterers with low speed, but fast-moving scatterers are not separated.

Table 3.3 shows the computation times of the three methods and the compensated MUSIC algorithm with default eig function, where the observation domain is divided into a 100×100 grid. It is worth noting that the superiority with respect to the computation time consumption of the proposed algorithm could be more significant if the dimension of the covariance matrix would be larger.

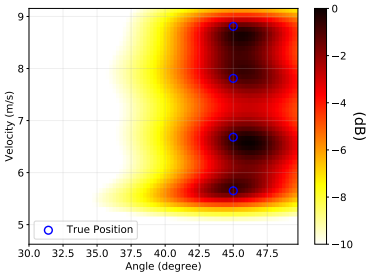

(a)

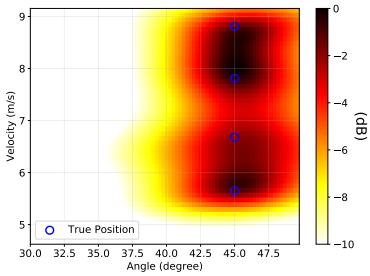

(b)

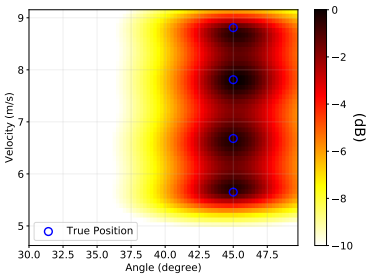

(c)

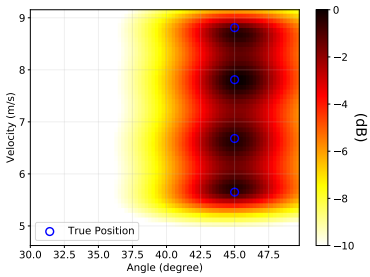

(d)

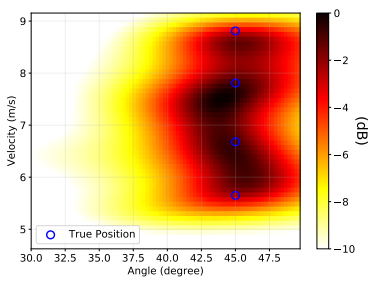

(e)

Figure 3.6: Angle-Velocity maps of $B = 1$ GHz and SNR$= 3$ dB for (a) 2D MUSIC without phase compensation, (b) 2D MUSIC after Keystone transform, (c) 2D MUSIC with phase compensation and accelerated by Lanczos algorithm, (d) 2D MUSIC with phase compensation and accelerated by Rayleigh-Ritz step and (e) 2D MUSIC with phase compensation and accelerated by inverse algorithm

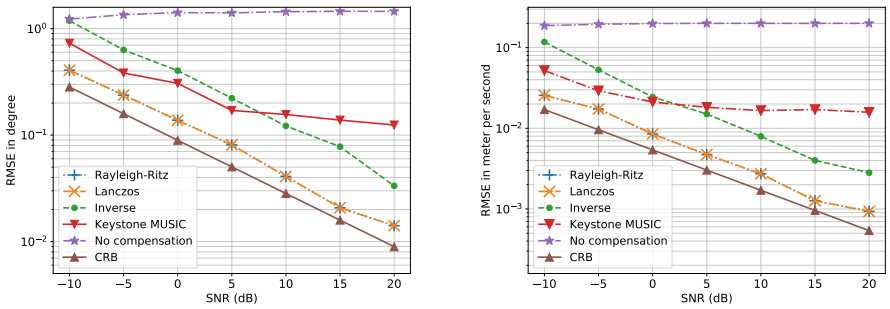

(a) (b)

Figure 3.7: Comparison of RMSEs with CRB as a function of SNR at $B = 4\,\mathrm{GHz}$ for one target at angle 40° and velocity $8\,\mathrm{m/s}$. (a) angle estimation and (b) velocity estimation

Table 3.3: Comparison of computational time

Algorithm	Computational Time
Default eig Func	152.68 s
Lanczos	18.75 s
Rayleigh-Ritz	5.48 s
Inverse	32.66 s
Keystone MUSIC	1.01 s

BANDWIDTH $4\,\mathrm{GHz}$

Next, we increase the bandwidth from $1\,\mathrm{GHz}$ to $4\,\mathrm{GHz}$, where the relative bandwidth is 5.1%. According to the model from (3.2), the estimation accuracy will deteriorate as the bandwidth increases. The same point scatterer with radial velocity $8\,\mathrm{m/s}$, angle 40° and range $80\,\mathrm{m}$ is set for RMSE simulation. The obtained RMSEs results of the proposed methods and the competitors are compared with CRB in Fig. 3.7. The error of the no compensation method is much larger than what we obtained in the case of $B = 1$ GHz.

The next simulation is to test the ability of the proposed algorithm to detect a relatively weak target. According to the analysis, if there is a strong migrated target present in an observation domain, the energy of this target will dominantly spread into several eigenvectors. Thus, the subspace corresponding to the relatively weak target will be allocated to noise subspace. Two targets, one with range 100 m, angle 20° , velocity 8 m/s and amplitude $\alpha = -10\,\mathrm{dB}$ and another one with range 80 m, angle 40°, radial velocity 5 m/s and amplitude $\alpha = 0\,\mathrm{dB}$, are set. The SNR is set to $30\,\mathrm{dB}$. The results are shown in Fig. 3.8, where for improved visibility the results

are normalised. From Fig. 3.8(a), we can see that the weak target is missing in the classic MUSIC result without phase compensation.

Both targets are seen in the MUSIC pseudo-spectrum obtained by Keystone MUSIC algorithms, however the peaks corresponding to the targets are wider than in the classical MUSIC or proposed algorithms and their relative contrast with the background is much smaller in magnitude.

Then 11 point scatterers with random angles from $0°$ to $50°$, random radial velocities from $0\,\mathrm{m/s}$ to $9\,\mathrm{m/s}$ and random ranges from $100\,\mathrm{m}$ to $200\,\mathrm{m}$ random α from $-3\,\mathrm{dB}$ to $0\,\mathrm{dB}$ are set and the SNR is set to $20\,\mathrm{dB}$. The normalised results are presented in Fig. 3.9, where the dynamic range is limited to $20\,\mathrm{dB}$.

From the angle-velocity map, one can conclude that the peaks of estimation without phase compensation are biased towards higher velocities and widened (especially in the azimuthal domain) in comparison with that of the proposed methods. Although the accuracies of estimation are slightly better, the Keystone MUSIC suffers from the poor resolution of closely spaced targets (especially in azimuth domain). At the same time, all three compensation algorithms demonstrate a clear separation of all targets and accurate estimation of their parameters. To show the improvement of the resolution of the proposed compensation method, an extra simulation using the same system parameters of 6 random point targets with large angles and velocities is implemented. The results without compensation, phase adjustment by Keystone transform and phase compensation by the proposed method are presented in Fig. 3.10. The three closely positioned targets are hardly resolved from Fig. 3.10 (a)(b), while they are clearly resolved in Fig. 3.10(c).

In the next simulation, we keep the same parameters as before while increasing the snapshots from 32 to 128. The results of the 11 point targets from the previous simulation are presented in Fig. 3.11. The imaging performance of the inverse algorithm significantly degrades when we increase snapshots to 128 and a strong ghost target appears at the position $(v = 0, \theta = 0)$, while the Rayleigh-Ritz and Lanczos algorithms reveal sharper peaks related to targets. It is noted that the results agree with the simulation in [73].

NUMBER OF TARGETS ESTIMATION

The 11 point scatterers from the previous simulation are used again in this simulation and the SNR is set to $20\,\mathrm{dB}$. Fig. 3.12 shows the number of target estimations using the different dimension of the signal subspace assumption. The connected region label algorithm is used here to obtain the number of targets from the binarised MUSIC spectrum. Here the threshold for binarization is set to $-7\,\mathrm{dB}$, which is a third of the mean value of the normalised MUSIC spectrum of a large number of target assumptions.

Fig. 3.13 shows the MUSIC spectrum of Rayleigh-Ritz method and classic

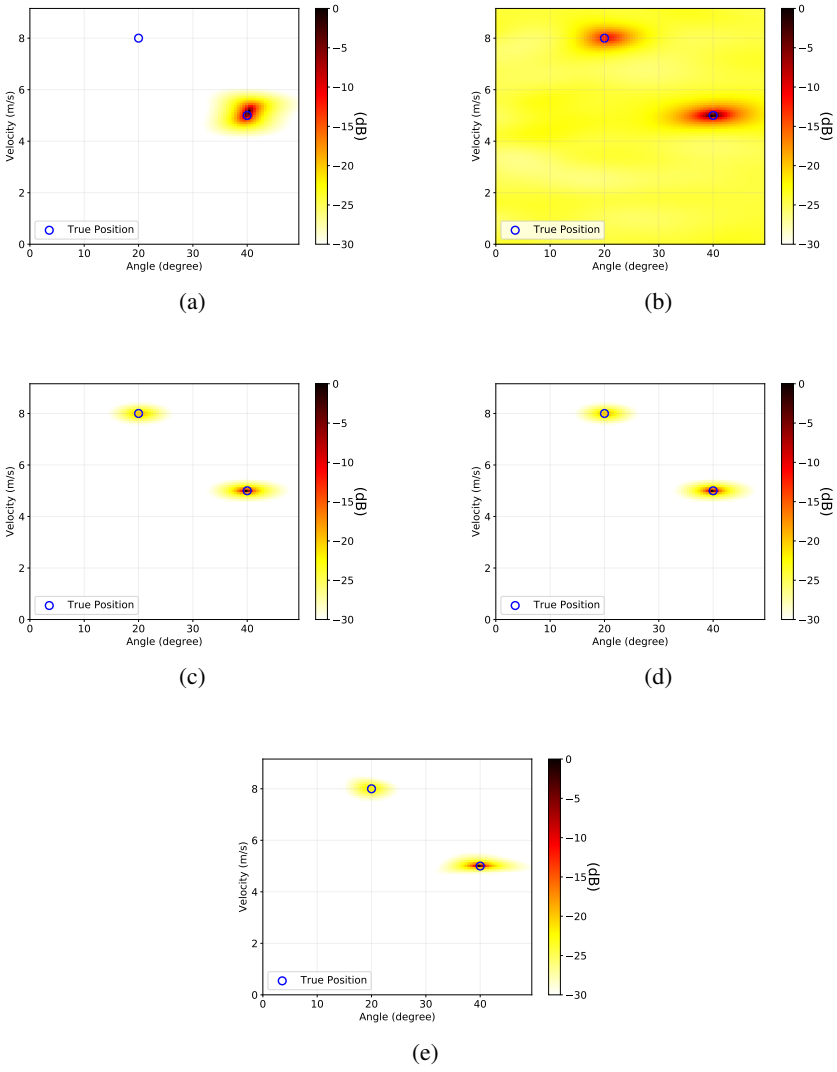

Figure 3.8: Angle-Velocity maps of $B = 4\,\text{GHz}$ and SNR$= 30\,\text{dB}$ for (a) 2D MUSIC without phase compensation, (b) 2D MUSIC after Keystone transform, (c) 2D MUSIC with phase compensation and accelerated by Lanczos algorithm, (d) 2D MUSIC with phase compensation and accelerated by Rayleigh-Ritz step and (e) 2D MUSIC with phase compensation and accelerated by inverse algorithm

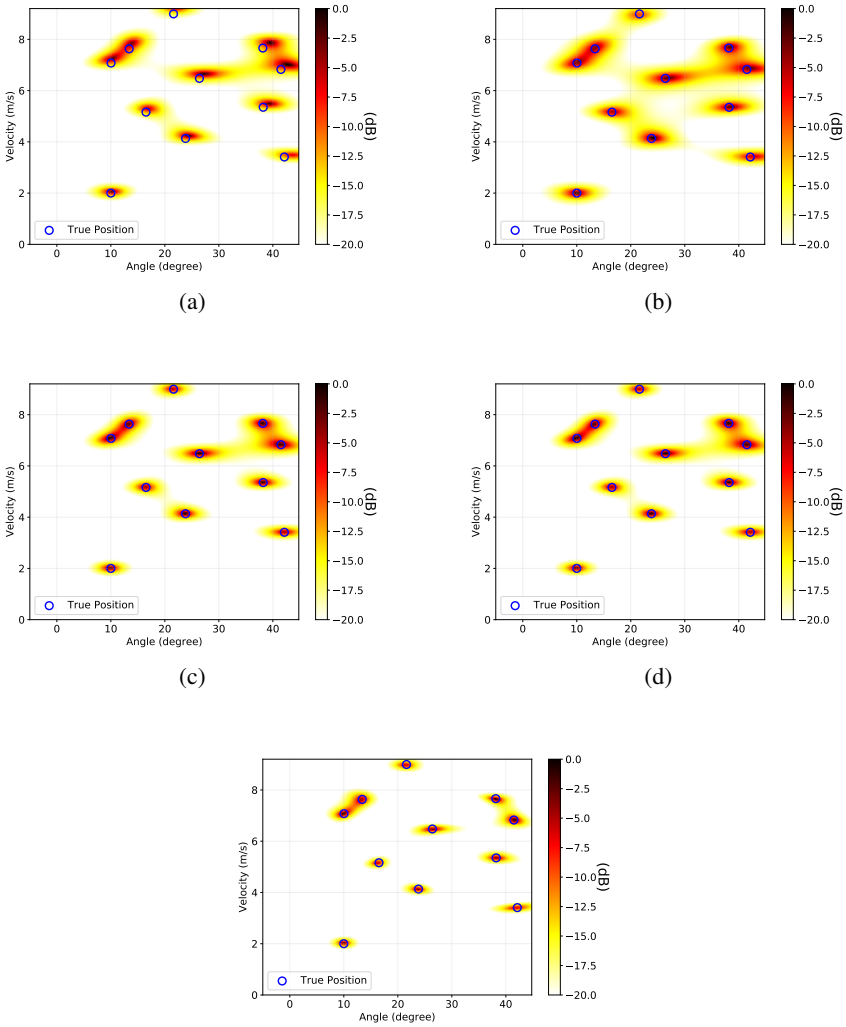

Figure 3.9: Angle-Velocity maps of $B = 4$ GHz and SNR= 20 dB for (a) 2D MUSIC without phase compensation, (b) 2D MUSIC after Keystone transform, (c) 2D MUSIC with phase compensation and accelerated by Lanczos algorithm, (d) 2D MUSIC with phase compensation and accelerated by Rayleigh-Ritz step and (e) 2D MUSIC with phase compensation and accelerated by inverse algorithm

MUSIC without compensation for the incorrect dimension of signal subspace assumptions. From the results, both classic MUSIC and compensation MUSIC will miss targets if the dimension of the signal subspace is underestimated. However,

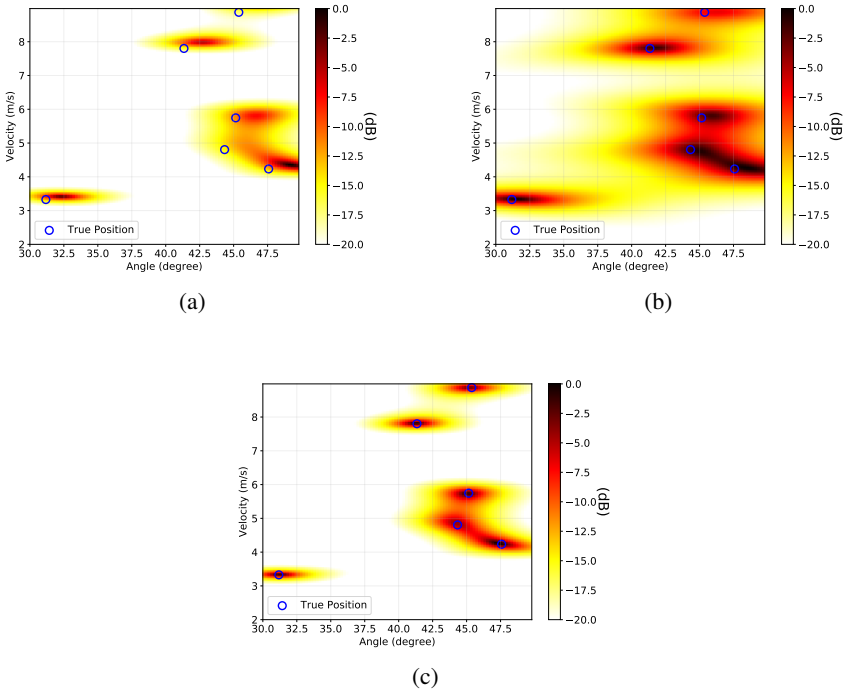

Figure 3.10: (a) 2D MUSIC without phase compensation and (b) 2D MUSIC after Keystone transform (c) 2D MUSIC with phase compensation and accelerated by Rayleigh-Ritz step

compared with Fig. 3.9, our proposed compensation MUSIC has a higher tolerance for overestimating the dimension of signal subspace than that of classic MUSIC.

3.5.2. 3D MUSIC

In this subsection, the numerical simulation for proposed 3D MUSIC algorithm are performed and the radar parameters are shown in Table 3.4.

Three targets at the coordinates (range (m), angle (degrees), velocity(m/s)) $(9, 30, 60)$, $(7, 40, 55)$ and $(8, 35, 50)$ are correspondingly set to simulate multiple moving targets. In this simulation, we assume the number of targets is known. However, the coupling terms usually make it very difficult to correctly estimate the number of sources. Thanks to the fact that the dynamic noise subspace is guaranteed to be orthogonal to the steering function vector, the number of the sources is allowed to be slightly overestimated as well in TD-MUSIC. There are many algorithms and tools of tensor decomposition available and in our simulation, the non-linear least square (NLS) is adopted [75]. The simulation results using 3D TD-

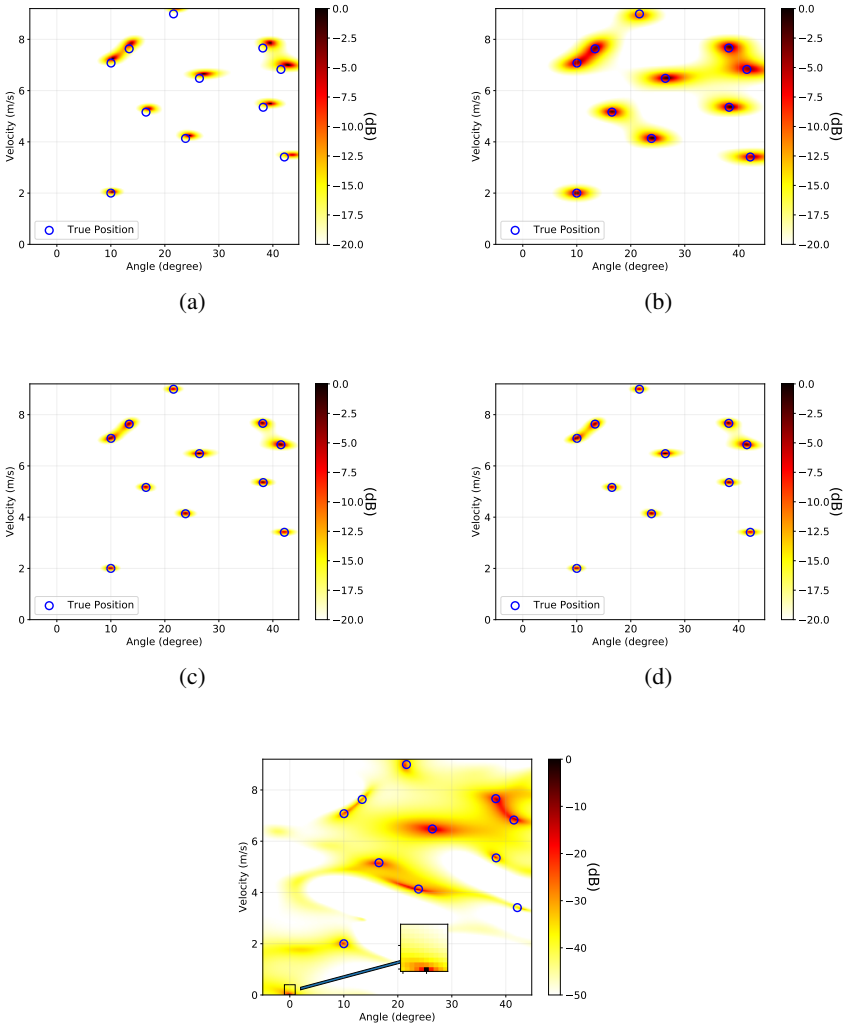

Figure 3.11: Angle-Velocity maps of $B = 4$ GHz, SNR= 20 dB and 128 snapshots for (a) 2D MUSIC without phase compensation, (b) 2D MUSIC after Keystone transform, (c) 2D MUSIC with phase compensation and accelerated by Lanczos algorithm, (d) 2D MUSIC with phase compensation and accelerated by Rayleigh-Ritz step and (e) 2D MUSIC with phase compensation and accelerated by inverse algorithm

MUSIC compensation are shown in Fig. 3.14(a)(c), respectively. From the figures, one can see that all the peaks corresponding to the targets reveal in the right position with high resolution. All the results are normalised and restricted in 20 dB for

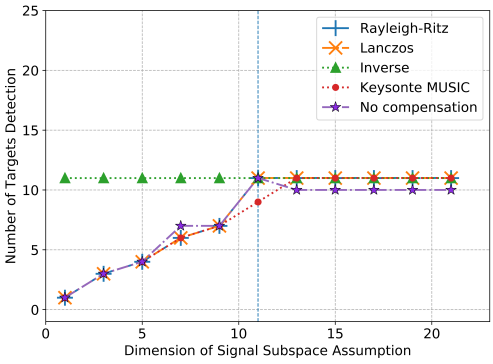

Figure 3.12: The number of targets estimation from MUSIC pseudo-spectrum using different dimensions of the signal subspace assumptions

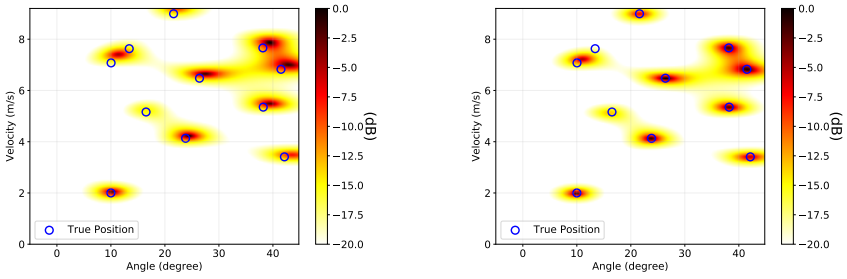

(a) (b)

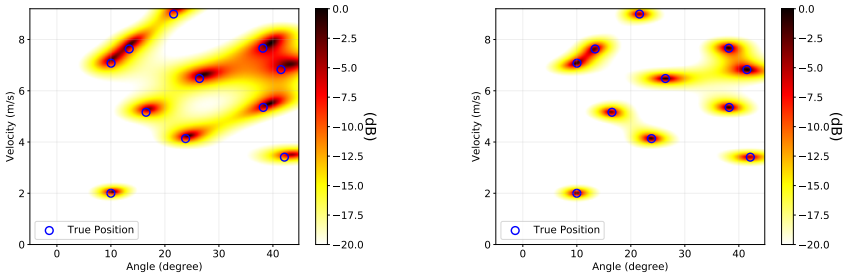

(c) (d)

Figure 3.13: Angle-Velocity maps of $B = 4$ GHz, SNR= 20 dB and 32 snapshots for (a) 2D MUSIC without compensation assume 10 targets, (b) Rayleigh-Ritz step assume 10 targets, (c) 2D MUSIC without compensation assume 16 targets and (d) Rayleigh-Ritz step assume 16 targets

Table 3.4: System Parameters

Parameters	**Values**
Carrier frequency	10 GHz
Number of antenna elements	8
Number of fast-time samplings	64
Number of pulses for CPI	8
Distance between elements	15 mm
Bandwidth	1 GHz
PRI	0.1 ms
SNR	10 dB

better observation.

For comparison, the results using the same 3D TD-MUSIC algorithm without compensation are shown in Fig. 3.14(b)(d), the peaks corresponding to the targets appear at the biased position and the close targets appear as ghost targets. According to the system parameters, although the target may not migrate more than one range resolution cell, the coupling terms influence the resolution and accuracy significantly. Thus, the phase residual phenomenon should not be ignored in the super-resolution algorithms.

The simulation results successfully validate the improvement of estimation performance on accuracy and resolution. The time for one slice map in Fig. 3.14(a) is around one minute, while the time for FFT is less than one second. Although 3D TD is more computationally intensive than conventional FFT, it provides much higher resolutions on estimation. This algorithm could be a subsidiary to provide better estimation in the local spectrum after implementing FFT. Moreover, with parallel processing and more powerful hardware techniques, TD-MUSIC could be a very promising algorithm in the future.

3.6. CONCLUSIONS

In this chapter, we first proposed joint Doppler-DOA estimation using the UWB FMCW array-based radar for moving targets. Using the signal model from Chapter 2 a modified 2D MUSIC algorithm to eliminate the influence of the inter-coupling terms. The method adjusts the phase of the raw data in each scanning grid before eigendecomposition to improve the accuracy of the Doppler and DOA estimation. Moreover, we propose two efficient implementations, namely a Lanczos algorithm and a Rayleigh-Ritz step, to reduce the computational burden specifically for the proposed method.

By comparing RMSEs and CRB of classical MUSIC, Keystone MUSIC and

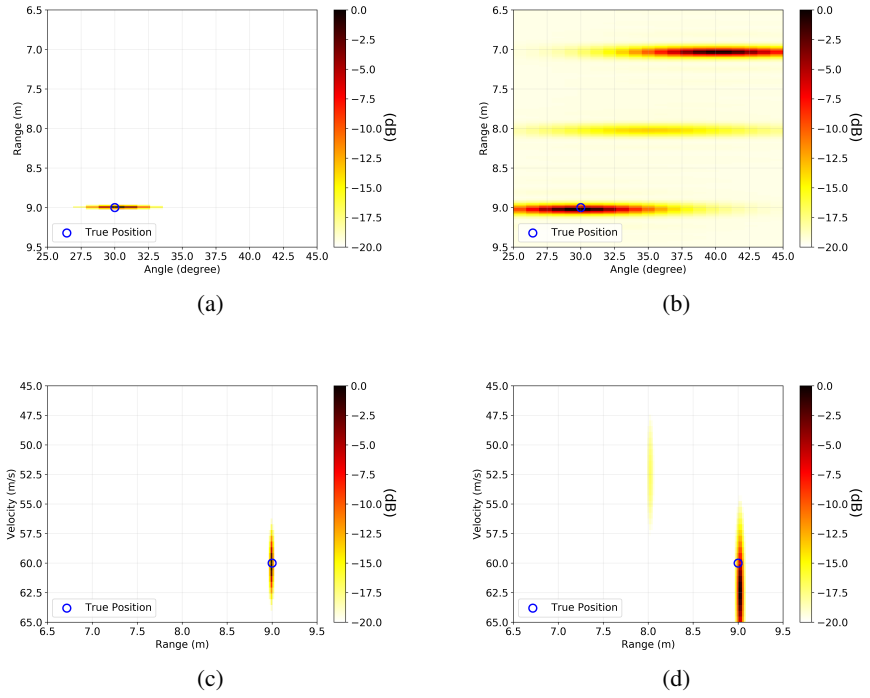

Figure 3.14: Range angle map at velocity 60 m/s (a) with phase compensation, (b) without phase compensation and Range-velocity map at angle 30° (c) with phase compensation, (d) without phase compensation

proposed algorithm (for the bandwidths of 1 GHz and 4 GHz) via numerical simulations, we demonstrate that the phase compensation algorithm improves the accuracies of both Doppler and DOA estimation over the classical and Keystone MUSIC and the accuracies of the proposed algorithm improve with SNR. For example, the accuracies of both Doppler and DOA estimations are improved more than 20 dB for SNR = 20 dB in Fig 3.7. Although for SNR below -10 dB Keystone MUSIC has similar accuracy to the proposed method, the resolution and overall contrast of the MUSIC pseudo-spectrum is worse than by the algorithm proposed. Due to the phase compensation, the algorithm proposed also resolves targets closely spaced in the velocity-angular domain, which are not resolvable both with the classical and Keystone MUSIC algorithms. Further, we show that the proposed Lanczos algorithm and Rayleigh-Ritz are more robust than the inverse algorithm in our simulations. In addition, the Rayleigh-Ritz step shows superiority with respect to computation time consumption when the number of targets is much smaller than the dimension of the signal covariance matrix and has a high tolerance for overestimating the dimension

of the signal subspace.

The compensation approach is further extended to 3D TD MUSIC in spite of the intensive computations. The influence of the coupling phase on the parameters estimation is removed at first by applying a compensation process for each velocity scanning bin. Then TD is applied to decompose the 3-dimensional raw data, and corresponding orthogonal signal subspace is obtained by orthogonalizing the Kronecker product of rank one component. Finally, the 3D MUSIC algorithms are used to estimate the range, Doppler and DOA jointly. The simulation results validate the improvements of proposed methods with high resolution in joint range, Doppler and DOA estimation.

4

JOINT PARAMETERS ESTIMATION USING SPECTRAL NORM-BASED ALGORITHM

The joint estimation of range, velocity and azimuth for multiple fast-moving targets using UWB FMCW radar with the antenna array in the presence of Doppler ambiguities is addressed. The range migration of moving targets is modelled by the mutual coupling between fast-time and slow-time (chirp index) and leads to the smearing of the target spectrum. This phenomenon degrades the performance of conventional detection and estimation techniques, however, it can be used to resolve Doppler (velocity) ambiguities. Similarly to range-Doppler processing, the performance of estimation of DOA with conventional narrowband-based algorithms significantly degrades if an UWB signal is employed. For the FMCW waveform, the wideband DOA differs from the narrowband one by an extra coupling term similar to the range migration problem. A novel spectral norm-based algorithm for joint range, velocity and DOA estimation of fast-moving targets is proposed taking the appropriate wideband signal model into account. The proposed spectral norm-based algorithm avoids the off-grid peak searching and can be easily accelerated by the power iteration algorithm; it outperforms the conventional coherent integration methods in both accuracy and efficiency for the moderate data size. The advantages of the proposed algorithm and its super-resolution ability are validated by the numerical simulations.

4.1. INTRODUCTION

The compensated MUSIC algorithms are introduced in the previous chapter to eliminate the coupling terms and the numerical simulations demonstrate the superiority of the algorithm over other counterparts. The algorithms perform well if the targets move with low velocities without the Doppler ambiguity. However, MUSIC fails to provide an efficient solution to resolve Doppler ambiguities when the Doppler frequencies are out of the scope of the maximum unambiguous velocity.

According to the analysis in Chapter 2, the product of the maximum unambiguous range and maximum unambiguous velocity is constrained by the sampling frequency. To reduce the cost of the hardware in the real applications, long-range and large unambiguous velocity cannot be achieved simultaneously. The range ambiguity is much difficult to resolve for single PRF signals, while the Doppler ambiguity could be estimated from the range migration.

This chapter presents a novel approach to address the problem of features (range, Doppler, DOA) extraction of multiple moving targets in the presence of Doppler ambiguity. The signal model developed in Chapter 2 is still used in this chapter, the difference from chapter 3 is that the velocity v_i could be much larger than $v_{\max}$ or less than $-v_{\max}$. A novel spectral norm-based algorithm is proposed to address the wideband DOA and Doppler ambiguity simultaneously.

There are 6 main algorithms listed in this chapter (**A**4$\backsim$**A**9) and the novelties of this chapter are summarised as:

1. The spectral norm-based algorithm introduced in **A**5 is based on a principally new approach and does not belong to any existing category of algorithms since it is a non-parametric and non-integration based algorithm. As described in Section 1.2.2, there exist three categories to address the Doppler ambiguity problem in state-of-the-art, while the method in the chapter can be recognised as the fourth category.

2. The coupling terms (range migration and wideband DOA) are addressed separately from the sinusoidal signals corresponding to the range, Doppler and DOA in **A**5, while the existing algorithms process the Doppler ambiguity from the coupling terms and sinusoids together. Moreover, due to the usage of alternative update between the coupling terms and the sinusoids in **A**5, the convergent condition is relaxed in terms of SNR.

3. The proposed algorithm outperforms the conventional coherent-integration-based algorithm in terms of accuracy since it avoids the off-grid problem for the fold number estimation.

4. By introducing an efficient implementation via the proposed data reshaping, **A**5 can be solved with less time and memory consumptions. Furthermore, **A**9 is

specifically proposed for our algorithm which provides a more efficient way to solve **A**5 by the power iteration algorithm (**A**8).

5. The performance of the proposed algorithm is analysed in detail for RMSEs of all target parameters estimation and is compared to the corresponding CRB in different scenarios. Furthermore, the simulation results demonstrate that the proposed algorithm holds the super-resolution ability of RELAX algorithm (**A**7).

The rest of the chapter is organised as follows. In Section 4.2, a novel algorithm for a single moving target is introduced. Subsequently, in Section 4.3 the proposed algorithm is combined with the greedy algorithm and RELAX estimator. Section 4.4 presents an efficient implementation of the proposed algorithm. Numerical examples are presented in Section 4.5 to illustrate the performance of the proposed algorithm and compare it with CRB. Finally, the conclusions are drawn in Section 4.7.

4.2. SINGLE TARGET

The joint estimation of range $\mathbf{r}$, velocity $\mathbf{v}$ and DOA $\boldsymbol{\theta}$ from the signal model (2.16) is a highly non-linear problem. In this section, we consider a single point target and propose a novel spectral-norm based algorithm for targets parameters estimation. Then a new alternative update method is introduced to assure the estimation accuracy.

Assume that there is only the ith target presented and all the interferences from other targets are removed or negligible. The data are represented as

$$\boldsymbol{\mathcal{Y}}_i = \alpha_i \mathbf{a}(\theta_i) \circ \mathbf{f}_d(v_i) \circ \mathbf{f}_r(r_i) \odot \boldsymbol{\mathcal{W}}_{\theta r}(\theta_i) \odot \boldsymbol{\mathcal{W}}_{dr}(v_i) + \boldsymbol{\mathcal{N}}. \tag{4.1}$$

Since the coupling terms are functions of the ambiguous velocity v_i and the DOA θ_i, the proposed method attempts to estimate these parameters from the coupling terms first.

4.2.1. COUPLING TERMS ESTIMATION

In this part, we first show a traditional coherent integration method for the parameters estimation from the coupling terms and the drawbacks are discussed. Second, a novel spectral norm-based method is introduced which performs better than conventional coherent integration approaches, especially when the data size is limited.

- Coherent integration-based method

The conventional integration-based methods are realised by the matched filter bank and usually can be implemented via multi-dimensional FFT if the data are uniformly sampled. For the signal model (4.1), the method can be written as

$$\check{v}_i, \check{\theta}_i = \underset{v,\theta}{\operatorname{argmax}} \, ||\mathscr{F}[\boldsymbol{\mathcal{Y}}_i \odot \boldsymbol{\mathcal{W}}^*_{\theta r}(\theta) \odot \boldsymbol{\mathcal{W}}^*_{dr}(v)]||_{\max}, \tag{4.2}$$

where the checkmark $\check{(\cdot)}$ denotes the parameters estimated from coupling terms. The $\check{v}_i$ is the unambiguous velocity which could be much larger than $v_{\max}$ or less than $-v_{\max}$. The estimates are based on peak detection of the coherently integrated energy of the compensated signals. If the coupling terms are correctly compensated, which means the ith target is focused, the integrated energy of the target will produce a maximum. The form of (4.2) corresponds to Generalized-RFT proposed in [34] if the array element dimension is removed, which means that (4.2) is the 3-dimensional form of RFT. Although various coherent integration algorithms are mentioned in the Section 4.1, (4.2) is sufficient to be used as the benchmark hereinafter since the optimality of RFT is shown to perform coherent integration for rectilinearly moving targets under the white Gaussian noise background [10].

4

Since the discrete Fourier spectrum is grid-based and could only yield the on-grid peak, even if the coupling terms are correctly compensated, the maximum spectrum might miss the Fourier grids. Then the on-grid peak of the Fourier spectrum may return a highly inaccurate estimation of $\check{v}_i$ and result in incorrect fold number extraction. This problem is severe if $M < \dfrac{f_0}{B}$ (when neighbouring slow-time frequency grids return different fold number estimation). Henceforth, in case of moderate data size, very dense zero-padding is needed to create the over-complete Fourier basis and match the data, which is both time- and memory-consuming. This problem will be shown in detail in Section 4.5.

- Norm-based method

To address the off-grid problem, we propose a novel spectral norm-based method which can estimate the location of an off-grid peak. To show the proposed algorithm, the data model $\boldsymbol{\mathcal{Y}}_i$ is reshaped into the matrix form $\mathbf{Y}_i \in \mathbb{C}^{LM\times K}$ by stacking the array element and slow-time dimensions together as

$$\mathbf{Y}_i = \begin{pmatrix} [\boldsymbol{\mathcal{Y}}_i]_{0,:,:} \\ [\boldsymbol{\mathcal{Y}}_i]_{1,:,:} \\ \vdots \\ [\boldsymbol{\mathcal{Y}}_i]_{L-1,:,:} \end{pmatrix}. \tag{4.3}$$

Rewrite $\mathbf{Y}_i$ compactly as

$$\mathbf{Y}_i = \alpha_i[\mathbf{a}(\theta_i) \otimes \mathbf{f}_d(v_i)]\mathbf{f}_r^T(r_i) \odot \boldsymbol{\Omega}_{\theta r}(\theta_i) \odot \boldsymbol{\Omega}_{dr}(v_i) + \mathbf{N}, \tag{4.4}$$

where $\mathbf{N} \in \mathbb{C}^{LM\times K}$ is the complex discrete noise, and the coupling matrices $\boldsymbol{\Omega}_{\theta r}(\theta_i) \in \mathbb{C}^{LM\times K}$ and $\boldsymbol{\Omega}_{dr}(v_i) \in \mathbb{C}^{LM\times K}$ are

$$\begin{aligned} \boldsymbol{\Omega}_{\theta r}(\theta_i) &= \boldsymbol{\Psi}(\theta_i) \otimes \mathbf{1}_M, \\ \boldsymbol{\Omega}_{dr}(v_i) &= \mathbf{1}_L \otimes \boldsymbol{\Phi}(v_i). \end{aligned} \tag{4.5}$$

Let $\mathbf{X}_i = \alpha_i[\mathbf{a}(\theta_i) \otimes \mathbf{f}_d(v_i)]\mathbf{f}_r^T(r_i)$, which is a rank-one matrix, then we can show the inequality

$$||\mathbf{X}_i \odot \mathbf{\Omega}_{\theta r}(\theta_i) \odot \mathbf{\Omega}_{dr}(v_i)||_2 \leq ||\mathbf{X}_i||_2, \tag{4.6}$$

with following proof

Proof: Because

$$\begin{aligned}
&||\mathbf{X}_i \odot \mathbf{\Omega}_{\theta r}(\theta_i) \odot \mathbf{\Omega}_{dr}(v_i)||_2 \\
&\quad \leq ||\mathbf{X}_i \odot \mathbf{\Omega}_{\theta r}(\theta_i) \odot \mathbf{\Omega}_{dr}(v_i)||_F \\
&\quad = \sqrt{\sum\nolimits_p \sum\nolimits_q |[\mathbf{X}_i]_{p,q}|^2 \cdot |[\mathbf{\Omega}_{\theta r}(\theta_i)]_{p,q}|^2 \cdot |[\mathbf{\Omega}_{dr}(v_i)]_{p,q}|^2} \\
&\quad = \sqrt{\sum\nolimits_p \sum\nolimits_q |[\mathbf{X}_i]_{p,q}|^2} \\
&\quad = ||\mathbf{X}_i||_F \\
&\quad = ||\mathbf{X}_i||_2,
\end{aligned} \tag{4.7}$$

where $|[\mathbf{\Omega}_{\theta r}(\theta_i)]_{p,q}|^2 = |[\mathbf{\Omega}_{dr}(v_i)]_{p,q}|^2 = 1$, and the equality holds iff $\mathbf{X}_i \odot \mathbf{\Omega}_{\theta r}(\theta_i) \odot \mathbf{\Omega}_{dr}(v_i)$ is rank-one matrix, which obviously is not (since it cannot be formulated by matrix product of two vectors). Here the property $||\mathbf{X}||_2 \leq ||\mathbf{X}||_F$ (equality holds iff $\mathbf{X}$ is rank-one matrix or zero matrix) is used [76].

According to the inequality (4.6), the parameters in the coupling terms can be extracted by

$$\begin{aligned}
\check{v}_i, \check{\theta}_i &= \underset{v,\theta}{\operatorname{argmax}} ||\mathbf{Y}_i \odot \mathbf{\Omega}_{dr}^*(v) \odot \mathbf{\Omega}_{\theta r}^*(\theta)||_2 \\
&= \underset{v,\theta}{\operatorname{argmax}} ||\mathbf{X}_i \odot \mathbf{\Omega}_{dr}(v_i - v) \odot \mathbf{\Omega}_{\theta r}(\theta_i - \theta) \\
&\qquad + \mathbf{N} \odot \mathbf{\Omega}_{dr}^*(v) \odot \mathbf{\Omega}_{\theta r}^*(\theta)||_2 \\
&= \underset{v,\theta}{\operatorname{argmax}} ||\mathbf{X}_i \odot \mathbf{\Omega}_{dr}(v_i - v) \odot \mathbf{\Omega}_{\theta r}(\theta_i - \theta)||_2 + \bar{\sigma} \\
&= \underset{v,\theta}{\operatorname{argmax}} ||\mathbf{X}_i \odot \mathbf{\Omega}_{dr}(v_i - v) \odot \mathbf{\Omega}_{\theta r}(\theta_i - \theta)||_2.
\end{aligned} \tag{4.8}$$

Because we assume the white Gaussian additive noise, the noise energy is uniformly distributed across the whole data and uncorrelated with the signal. Moreover, the compensation to the noise is just a phase shift, it will not increase the noise power. Therefore, after the same phase shift, the noise term $\mathbf{N} \odot \mathbf{\Omega}_{dr}^*(\check{v}_i) \odot \mathbf{\Omega}_{\theta r}^*(\check{\theta}_i)$ is still uncorrelated with the signal component and can be put out from spectral norm as a constant $\bar{\sigma}$.

It is worth noting that the matrix stacking in (4.3) is a practical way to perform matrix manipulation for multi-way data [77]. Although according to the simulation

results, TD could provide similar performance, it is not yet proved mathematically and TD is computationally heavier than matrix norm computation [78].

The non-linear optimisation of (4.8) requires a two-dimensionally exhaustive search on ambiguous velocity v and angle θ simultaneously. In Section 4.4 we demonstrate that (4.8) can be decomposed into two separate one-dimensional searches via the data reshaping.

Compared to the integration-based method, the peak is found without the Fourier grids. Thus, the off-grid problem for the estimates from coupling terms can be avoided. The detailed comparison will be presented in Section 4.5.

4.2.2. FREQUENCIES ESTIMATION

According to the analysis of the CRBs of the folded velocity $\hat{v}_i$ ($|\hat{v}_i| < v_{\max}$) from the sinusoids and the unambiguous velocity $\check{v}_i$ from coupling term separately (see in Appendix A), the estimation accuracy of $\hat{v}_i$ is much higher than that of $\check{v}_i$. Thus, the parameter estimations from the coupling terms are less reliable and less accurate than those from the sinusoids. However, more accurate parameters (azimuth, folded velocity and range) can be obtained from the sinusoids after compensation of the coupling terms using the coarse estimations (azimuth $\check{\theta}_i$ and unambiguous velocity $\check{v}_i$). With the coarse estimates $\check{v}_i$, $\check{\theta}_i$ from (4.8), the compensation terms are formulated as $\boldsymbol{\mathcal{W}}^*_{dr}(\check{v}_i)$ and $\boldsymbol{\mathcal{W}}^*_{\theta r}(\check{\theta}_i)$. If performed with $\boldsymbol{\mathcal{Y}}_i \odot \boldsymbol{\mathcal{W}}^*_{dr}(\check{v}_i) \odot \boldsymbol{\mathcal{W}}^*_{\theta r}(\check{\theta}_i)$, the new decoupled data are obtained. Since there is only one target present and for simplicity, the method for parameters estimation is given from the decoupled data using matched filter

$$\begin{aligned} \tilde{\boldsymbol{\mathcal{Y}}}_i &= \boldsymbol{\mathcal{Y}}_i \odot \boldsymbol{\mathcal{W}}^*_{dr}(\check{v}_i) \odot \boldsymbol{\mathcal{W}}^*_{\theta r}(\check{\theta}_i), \\ \hat{v}_i, \tilde{\theta}_i, \tilde{r}_i &= \underset{v,\theta,r}{\operatorname{argmax}} \, ||\boldsymbol{\mathcal{Y}}_i \times_1 \mathbf{a}^T(\theta) \times_2 \mathbf{f}_d^T(v) \times_3 \mathbf{f}_r^T(r)||_{\max}, \end{aligned} \tag{4.9}$$

where $\tilde{(\cdot)}$ denotes the estimated parameter.

4.2.3. FOLD NUMBER ESTIMATION

As the coarse unambiguous velocity $\check{v}_i$ and the folded velocity $\hat{v}_i$ are estimated, then the initial fold number estimation can be obtained according to (2.19) by

$$\tilde{n}_i = \left\lfloor \frac{\check{v}_i + v_{\max}}{2v_{\max}} \right\rfloor, \tag{4.10}$$

and more accurate estimation of unambiguous velocity is given as

$$\tilde{v}_i = \hat{v}_i + 2v_{\max}\tilde{n}_i. \tag{4.11}$$

It is shown in (4.11) that the unambiguous velocity is divided as the folded velocity $\hat{v}_i$ which is estimated from sinusoidal components and the fold number which is extracted from the coupling components.

It works very well in most cases, however, (4.11) fails in the worst case when the velocity v_i is very close to $(2n+1)v_{\max}$. The problem is illustrated in Fig. 4.1, where Eq. (4.11) works when the targets are located in the grey or cyan region. However, if the target is located close to $(2n+1)v_{\max}$ (green region in Fig. 4.1), for instance, assume $v_i = 3v_{\max}$, the estimate from the coupling component returns $\check{v}_i \approx 3v_{\max}$ (which is indicated as red dashed arrows), then (4.11) might return uncertain fold number 1 or 2 depending on the noise, interference from the other targets and the computational accuracy. Additionally, the estimate $\hat{v}_i$ from the sinusoidal component is $|\hat{v}_i| \approx v_{\max}$ (which is indicated as blue dashed arrows), which might return $\hat{v}_i \lesssim v_{\max}$ or $\hat{v}_i \gtrsim -v_{\max}$. Therefore, there could be 4 combinations of (4.11) and different $\tilde{v}_i$ would be obtained. This problem would happen in each iteration of the RELAX algorithm and would influence the convergence of the RELAX algorithm significantly.

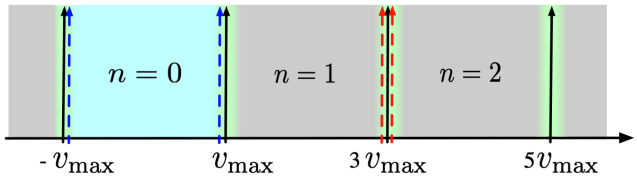

Figure 4.1: Illustration of fold number estimation

To solve this problem, a novel approach is introduced. Since if $v_i \approx (2n+1)v_{\max}$, we have $|\hat{v}_i| \approx v_{\max}$. A threshold ε is set to test the difference $||\hat{v}_i| - v_{\max}|$, and this threshold is determined by the accuracy of the estimate $\hat{v}_i$. If $||\hat{v}_i| - v_{\max}| \leq \varepsilon$ is satisfied, (4.10) is modified by replacing floor operation $\lfloor\rfloor$ by round operation $\lfloor\rceil$ to obtain the uncertain fold number. Then the fold number can be determined according to the sign of $\hat{v}_i$. If $\hat{v}_i < 0$ the fold number is correctly estimated with more confidence, otherwise the fold number is more likely overestimated.

According to the analysis, the fold number estimation is summarized in **Algorithm** 4 (**A**4).

4.2.4. REFINE THE PARAMETERS BY ALTERNATION

As we mentioned before, the unambiguous velocity estimate $\check{v}_i$ is coarse and inaccurate which may result in the inaccuracy of the estimations of $\hat{v}_i$ and $\tilde{n}_i$. Thus, a novel refinement method is introduced to improve the accuracy of the estimation by alternatively updating $\tilde{v}_i, \tilde{\theta}_i$ by (4.9) and (4.11) and updating $\boldsymbol{\mathcal{W}}^*_{dr}(\check{v}_i), \boldsymbol{\mathcal{W}}^*_{\theta r}(\check{\theta}_i)$ by $\check{v}_i,\ \check{\theta}_i \Leftarrow \tilde{v}_i,\ \tilde{\theta}_i$. The reason is straightforward because the accurate $\tilde{v}_i$ and $\tilde{\theta}_i$ lead to accurate coupling terms compensation and in return increase the accuracies of $\tilde{v}_i$ and $\tilde{\theta}_i$. Since the alternative method converges very fast, only 3 or 4 repeats

Algorithm 4 Fold Number Estimation Algorithm (**A**4)

Input: $\hat{v}_i$, $\check{v}_i$, $v_{\max}$, ε
if $||\hat{v}_i| - v_m| > \varepsilon$:
    $\tilde{n}_i = \left\lfloor \frac{\check{v}_i + v_{\max}}{2v_{\max}} \right\rfloor$
    $\tilde{v}_i = \hat{v}_i + 2v_{\max}\tilde{n}_i$
else:
    $\tilde{n}_i = \left\lfloor \frac{\check{v}_i + v_{\max}}{2v_{\max}} \right\rfloor$
    if $\hat{v}_i > 0$:
        $\tilde{n}_i \Leftarrow \tilde{n}_i - 1$
    endif:
    $\tilde{v}_i = \hat{v}_i + 2v_{\max}\tilde{n}_i$
endif
Output: $\tilde{n}_i$, $\tilde{v}_i$

are sufficient for convergence. Although the alternation process only needs a few repeats, it is very important and influences the estimation results significantly. The comparison with and without such alternation will be shown in Section 4.5.

4.2.5. AMPLITUDE ESTIMATION

As we have already estimated the frequencies, the estimation of the complex amplitude is directly given by

$$\tilde{\alpha}_i = \frac{1}{LMK}[\boldsymbol{\mathcal{Y}}_i \odot \boldsymbol{\mathcal{W}}^*_{dr}(\check{v}_i) \odot \boldsymbol{\mathcal{W}}^*_{\theta r}(\check{\theta}_i)] \times_1 \mathbf{a}^T(\tilde{\theta}_i) \times_2 \mathbf{f}_d^T(\hat{v}_i) \times_3 \mathbf{f}_r^T(\tilde{r}_i). \quad (4.12)$$

Although the alternation steps can optimize the solutions, (4.9) is still an on-grid estimation. As soon as the relatively accurate estimation is obtained as the initial guess, the Nelder-Mead method [79] is adopted to optimize the estimation of the local optimal off-grid solution as

$$\begin{aligned} \tilde{\boldsymbol{\mathcal{Y}}}_i &= \boldsymbol{\mathcal{Y}}_i \odot \boldsymbol{\mathcal{W}}^*_{dr}(\check{v}_i) \odot \boldsymbol{\mathcal{W}}^*_{\theta r}(\check{\theta}_i), \quad (4.13) \\ \tilde{\alpha}_i, \tilde{v}_i, \tilde{\theta}_i, \tilde{r}_i &= \underset{\alpha,v,\theta,r}{\operatorname{argmax}} ||\boldsymbol{\mathcal{Y}}_i - \alpha \mathbf{a}(\theta) \circ \mathbf{f}_d(v) \circ \mathbf{f}_r(r)||_F. \end{aligned}$$

The algorithm for a single target is summarised as **Algorithm** 5 (**A**5).

4.3. MULTIPLE TARGETS

In this section, the multiple target scenario is considered and the estimation is performed in two steps: first, a greedy algorithm for initialisation, and second, the

Algorithm 5 Alternation Algorithm (**A**5)

1: Estimate $\check{v}_i, \check{\theta}_i = \underset{v,\theta}{\operatorname{argmax}} ||\mathbf{Y}_i \odot \mathbf{\Omega}^*_{dr}(v) \odot \mathbf{\Omega}^*_{\theta r}(\theta)||_2$
2: Estimate fold number $\tilde{n}_i = \left\lfloor \dfrac{\check{v}_i + v_{\max}}{2v_{\max}} \right\rfloor$
3: **repeat**
4: Update $\hat{v}_i, \tilde{\theta}_i, \tilde{r}_i$ from (4.9)
5: Update $\tilde{v}_i$, $\tilde{n}_i$ according to **A**4
6: Update $\check{v}_i,\ \check{\theta}_i \Leftarrow \tilde{v}_i,\ \tilde{\theta}_i$
7: Update $\boldsymbol{\mathcal{W}}^*_{dr}(\check{v}_i)$ and $\boldsymbol{\mathcal{W}}^*_{\theta r}(\check{\theta}_i)$
8: **until** the stop criteria satisfied
9: Estimate $\tilde{\alpha}_i$ from (4.12)
10: Optimize (4.13) using Nelder-Mead method
11: **Output:** $\tilde{\alpha}_i,\ \tilde{v}_i,\ \tilde{\theta}_i,\ \tilde{r}_i$

RELAX algorithm for optimisation. Both the greedy algorithm and the RELAX algorithm have been widely used and show an effective performance in many applications [2, 13, 14, 80–84]. Thus, the general ideas of the greedy and RELAX algorithm are adapted to the multiple-target scenario with the proposed method of a single target.

4.3.1. GREEDY ALGORITHM

For multiple targets, the greedy algorithm is performed to extract and remove each target sequentially. By applying the **A**5 to the raw data, the parameters of the target with maximum magnitude will be estimated. Construct the reflected signal as $\tilde{\boldsymbol{\mathcal{Z}}}_i$ and subtract it from the data as

$$\begin{aligned} \tilde{\boldsymbol{\mathcal{Z}}}_i &= \tilde{\alpha}_i \mathbf{a}(\tilde{\theta}_i) \circ \mathbf{f}_d(\tilde{v}_i) \circ \mathbf{f}_r(\tilde{r}_i) \odot \boldsymbol{\mathcal{W}}_{\theta r}(\tilde{\theta}_i) \odot \boldsymbol{\mathcal{W}}_{dr}(\tilde{v}_i), \\ \boldsymbol{\mathcal{Z}} &\Leftarrow \boldsymbol{\mathcal{Z}} - \tilde{\boldsymbol{\mathcal{Z}}}_i, \end{aligned} \tag{4.14}$$

where the initialisation is made with $\boldsymbol{\mathcal{Z}} \Leftarrow \boldsymbol{\mathcal{Y}}$. Repeat **A**5 by updating $\boldsymbol{\mathcal{Z}}$ in (4.14) until some stop condition is satisfied. Here a threshold of magnitude is selected as the criterion for the stopping condition and defining the number of targets for simplicity. The greedy algorithm stops if the magnitude of the ith target is smaller than the threshold ϵ_1. The threshold ϵ_1 can be selected relatively smaller than the desired magnitude and the number of targets is allowed to be slightly overestimated since it will be reconsidered later.

This algorithm is summarised as **Algorithm** 6 (**A**6).

Algorithm 6 Greedy Algorithm (**A**6)

1: $\boldsymbol{\mathcal{Z}} = \boldsymbol{\mathcal{Y}}$, $i = 1$
2: **repeat**
3: Estimate ith parameters $\tilde{\boldsymbol{\vartheta}}_i$ using **A**5 from $\boldsymbol{\mathcal{Z}}$
4: Formulate $\tilde{\boldsymbol{\mathcal{Z}}}_i$, and remove it from $\boldsymbol{\mathcal{Z}}$ as (4.14)
5: $i \Leftarrow i + 1$
6: **until** $|\tilde{\alpha}_i| \leq \epsilon_1$
7: **Output:** number of targets $\tilde{I} = i$ and all the corresponding features $\tilde{\boldsymbol{\vartheta}}_i = [\tilde{\alpha}_i,\ \tilde{v}_i,\ \tilde{\theta}_i,\ \tilde{r}_i]$

4

4.3.2. RELAX ALGORITHM

The estimation results of **A**6 are coarse since the mutual interference between the targets will affect the estimation of other targets and the estimation error will accumulate with the increase of the number of targets in the scene. To address this problem, an iterative parameters estimation method is presented in this subsection [80].

Assume the number of the targets has been estimated, which can be incorrect and will be reconsidered in the following, the parameters of the ith targets can be re-estimated by **A**5 from the data without the interference from the other targets

$$\boldsymbol{\mathcal{Z}}_i \Leftarrow \boldsymbol{\mathcal{Y}} - \sum_{p \neq i} \tilde{\boldsymbol{\mathcal{Z}}}_p. \tag{4.15}$$

Thus, the new parameters are estimated without interference from the side lobes or spread spectrum from the other targets. This algorithm loops from $i = 1$ to $i = \tilde{I}$, and for more accurate estimation, it has to be repeated multiple times. As the number of the targets may be slightly overestimated, a more demanding threshold ϵ_2 can be set after several iterations. Once the magnitude is lower than ϵ_2 in the iteration, the corresponding target is abandoned.

To save computational time, (4.8) is replaced by

$$\check{n}_i, \check{\theta}_i = \underset{n,\theta}{\operatorname{argmax}} ||\mathbf{Y} \odot \boldsymbol{\Omega}^*_{dr}(\hat{v}_i + 2nv_m) \odot \boldsymbol{\Omega}^*_{\theta r}(\theta)||_2, \tag{4.16}$$

and (4.10) in **A**5 is replaced by

$$\tilde{n}_i \Leftarrow \check{n}_i. \tag{4.17}$$

This is because we already have a relatively accurate estimation of the folded velocity $\hat{v}_i$, the information desired from the coupling term is the fold number $\tilde{n}_i$. The stop criterion can be made based on the estimation convergence.

The iterative algorithm is summarised in **Algorithm** 7 (**A**7).

Algorithm 7 RELAX Algorithm (**A**7)

1: Apply **A**6 for initial parameters estimation
2: **repeat**
3: $\quad \boldsymbol{\mathcal{Z}} = \boldsymbol{\mathcal{Y}}$
4: $\quad$ **for** $i = 1 : \tilde{I}$ **do**
5: $\quad\quad \boldsymbol{\mathcal{Z}}_i = \boldsymbol{\mathcal{Z}} - \sum_{p \neq i} \tilde{\boldsymbol{\mathcal{Z}}}_p$
6: $\quad\quad$ Estimate ith parameters using **A**5 from $\boldsymbol{\mathcal{Z}}_i$ and reformulate $\tilde{\boldsymbol{\mathcal{Z}}}_i$, where (4.8) is replaced by (4.16) and (4.10) is replaced by (4.17)
7: $\quad$ **end for**
8: $\quad$ After several iterations, abandon the targets according to $|\tilde{\alpha}_i| \leq \epsilon_2$ and update $\tilde{I}$
9: **until** some stop criteria satisfied

NUMBER OF TARGETS ESTIMATION

The estimation of the number of scatterers is usually a difficult problem, especially in the presence of the coupling components. Although the proposed magnitude thresholding works very well when the targets are far-separated from each other, it may be difficult to define the thresholds when there are too many closely spaced targets within Rayleigh resolution. An alternative way is to combine the proposed method with generalized Akaike information criterion (GAIC). Since it is not the main contribution of this thesis, readers are referred to [2].

4.4. EFFICIENT IMPLEMENTATION

It is time-consuming to solve (4.8) with the simultaneously two-dimensional scanning. In this section, we introduce a novel method to solve it efficiently. In fact, (4.8) can be solved separately by two one-dimensional scanning on v and θ. Here, we show the method of estimating $\check{v}_i$ as an example. For doing that, we reshape the tensor data (4.1) to a new matrix form by stacking the array element and the fast-time dimensions together in matrix $\mathbf{V}_i \in \mathbb{C}^{M \times LK}$ as

$$\mathbf{V}_i = \Big([\boldsymbol{\mathcal{Y}}_i]_{0,:,:}, [\boldsymbol{\mathcal{Y}}_i]_{1,:,:}, \cdots [\boldsymbol{\mathcal{Y}}_i]_{L-1,:,:} \Big), \tag{4.18}$$

and it can be written compactly as

$$\begin{aligned} \mathbf{V}_i =& \alpha_i \mathbf{f}_d(v_i) [\mathbf{a}(\theta_i) \otimes \mathbf{f}_r(r_i)]^T \odot \Big[\mathbf{1}_M \boldsymbol{\psi}^T(\theta_i) \Big] \odot \Big[\mathbf{1}_L^T \otimes \boldsymbol{\Phi}(v_i) \Big] + \bar{\mathbf{N}} \\ =& \alpha_i \mathbf{f}_d(v_i) \left[\mathbf{a}(\theta_i) \otimes \mathbf{f}_r(r_i) \odot \boldsymbol{\psi}(\theta_i) \right]^T \odot \Big[\mathbf{1}_L^T \otimes \boldsymbol{\Phi}(v_i) \Big] + \bar{\mathbf{N}}, \end{aligned} \tag{4.19}$$

where $\boldsymbol{\psi}(\theta_i) \in \mathbb{C}^{LK\times 1}$ is

$$\boldsymbol{\psi}(\theta_i) = \begin{pmatrix} \mathbf{h}_0(\theta_i) \\ \mathbf{h}_1(\theta_i) \\ \vdots \\ \mathbf{h}_{L-1}(\theta_i) \end{pmatrix}. \tag{4.20}$$

Such reshaping of the data is beneficial to use matrix manipulation and more importantly, to hide the wideband DOA coupling term into the same dimension by stacking element indices l and fast-time samples k together. Thus, the matrix $\alpha_i \mathbf{f}_d(v_i)\left[\mathbf{a}(\theta_i) \otimes \mathbf{f}(r_i) \odot \boldsymbol{\psi}(\theta_i)\right]^T$, which contains the wideband DOA coupling term, is a rank-one matrix. Similar to (4.6), we have

$$\begin{aligned} &||\alpha_i \mathbf{f}_d(v_i)\left[\mathbf{a}(\theta_i) \otimes \mathbf{f}_r(r_i) \odot \boldsymbol{\psi}(\theta_i)\right]^T \odot \left[\mathbf{1}_L^T \otimes \boldsymbol{\Phi}(v_i)\right]||_2 \\ &\quad \leq ||\alpha_i \mathbf{f}_d(v_i)\left[\mathbf{a}(\theta_i) \otimes \mathbf{f}_r(r_i) \odot \boldsymbol{\psi}(\theta_i)\right]^T||_2. \end{aligned} \tag{4.21}$$

So $\check{v}_i$ can be estimated by one-dimensional search as

$$\check{v}_i = \underset{v}{\operatorname{argmax}} ||\mathbf{V}_i \odot [\mathbf{1}_L^T \otimes \boldsymbol{\Phi}^*(v)]||_2. \tag{4.22}$$

Now we focus on the efficient solution of (4.22). Although there is a default $norm$ function in MATLAB, it is not optimised for our specific problem. Let $\boldsymbol{\Lambda}_i(\check{v}_i) = \mathbf{V}_i \odot [\mathbf{1}_L^T \otimes \boldsymbol{\Phi}^*(v)]$, so

$$||\boldsymbol{\Lambda}_i(v)||_2 = \sqrt{||\sigma(\boldsymbol{\Lambda}_i(v)\boldsymbol{\Lambda}_i^H(v))||_{\max}}. \tag{4.23}$$

The solution of the spectral norm is transformed into the estimation of the largest eigenvalue of the matrix $\boldsymbol{\Lambda}_i(v)\boldsymbol{\Lambda}_i^H(v)$. Thus, compared to (4.3), another benefit of (4.18) is that the smallest dimension of the data matrix is shrunk to reduce the computational load of calculating the spectral norm. There are many algorithms to perform the eigendecomposition of a Hermitian matrix; here we propose to use the simple power iteration algorithm since only the largest eigenvalue is needed [85]. Moreover, the compensations in the adjacent searching grids are just a minor phase shift, thus, the eigenvectors associated with the largest eigenvalues for the neighbouring searching grids are close to each other in the norm distance. According to the simulation, after good initialisation, only a few power iterations are required to provide sufficiently good largest eigenvalue approximation with the previous eigenvector as the initial guess. To make the thesis self-contained, the power iteration algorithm is given in **Algorithm** 8 (**A**8).

Based on the analysis, the efficient implementation of (4.22) is shown in **Algorithm** 9 (**A**9), where the velocity searching domain $\check{\mathbf{v}}$ is $-V : \Delta v : V$ (sampled with the linear spacing Δv).

Algorithm 8 Power Iteration (**A**8)

1: **Input:** Hermitian matrix $\mathbf{R}$, $\mathbf{u}^{(0)}$ with $||\mathbf{u}^{(0)}|| = 1$, $j = 0$
2: **repeat**
3: $\quad \mathbf{w} = \mathbf{R}\mathbf{u}^{(j)}$
4: $\quad \mathbf{u}^{(j+1)} = \mathbf{w}/||\mathbf{w}||$
5: $\quad \lambda^{(j+1)} = (\mathbf{u}^{(j+1)})^H \mathbf{R}\mathbf{u}^{(j+1)}$
6: $\quad j \Leftarrow j + 1$
7: **until** $|\lambda^{(j)} - \lambda^{(j-1)}| < \delta$, δ is the presetting threshold
8: **Output:** $\mathbf{u}^{(j)}$, $\lambda^{(j)}$

Algorithm 9 Efficient Implementation of (4.22) (**A**9)

1: Initialize $\mathbf{u}^{(0)} = [1, 0, 0, ..., 0] \in \mathbb{R}^{M\times 1}$, empty vector $\boldsymbol{\lambda} = \varnothing$, searching domain $\check{\mathbf{v}} = -V : \Delta v : V$, $j = 0$
2: **for** v in $\check{\mathbf{v}}$ **do**
3: $\quad \mathbf{R} = \boldsymbol{\Lambda}_i(\mathrm{v})\boldsymbol{\Lambda}_i^H(\mathrm{v})$
4: $\quad$ Compute $\lambda^{(j+1)}$ and $\mathbf{u}^{(j+1)}$ using **A**8 with input $\mathbf{R}$ and $\mathbf{u}^{(j)}$
5: $\quad$ Store the eigenvalue $[\boldsymbol{\lambda}]_j = \lambda^{(j+1)}$
6: $\quad j \Leftarrow j + 1$
7: **end for**
8: Find index q of $||\boldsymbol{\lambda}||_{\max}$ in $\boldsymbol{\lambda}$
9: **Output:** $[\check{\mathbf{v}}]_q$

The angle $\check{\theta}_i$ can be estimated similarly by stacking the slow-time and the fast-time dimensions together from (4.1). The derivations are straightforward and omitted here.

4.5. SIMULATIONS

In this section, several numerical examples are presented to demonstrate the effectiveness of the proposed algorithm.

The conventional coherent-integration method by replacing step 1 in **A**5 by (4.2) (FFT-based algorithm) are compared with the proposed algorithm in terms of accuracy and time consumption. The RMSE is obtained by 400 Monte-Carlo trials as RMSE $= \sqrt{\mathbb{E}[(\tilde{\vartheta} - \vartheta)^2]}$, where $\tilde{\vartheta}$ denotes the estimated parameter and ϑ is its true value. The starting frequency of the FMCW waveform is $f_0 = 77$ GHz and the chirp duration is $T_0 = 0.08$ ms. The chirp repetition interval is $T = 0.1$ ms and $M = 8$ chirps data are collected for simulation, so the total CPI is 0.8 ms. A standard ULA of $L = 8$ elements with the inter-element distance

of $d = \frac{c}{2f_0} = \frac{\lambda}{2} \approx 0.195$mm is considered for the receivers. Therefore, within such a short time, all the targets are approximately moving with constant velocities. According to the parameters, the unambiguous velocity domain is $[-v_{\max}, v_{\max})$ with $v_{\max} \approx 9.7$ m/s. Unless otherwise stated, the alternation in **A**5 is repeated 3 times as default; the default bandwidth is set as $B = 4$ GHz, which means the theoretical range resolution is $\Delta r = \frac{c}{2B} \approx 0.037$ m; the magnitudes of the targets follow $|\alpha_i| \sim \mathcal{U}(0.5, 1)$ and keep constant over observation time; the threshold ϵ_1 is set as $0.2 \times |\tilde{\alpha}_1|$ and ϵ_2 is set as $0.4 \times |\tilde{\alpha}_1|$, where $|\tilde{\alpha}_1|$ is the estimated magnitude of first target and usually is the largest magnitude among all targets; the velocities of the targets are set randomly, following the uniform distribution as $v_i \sim \mathcal{U}(-6v_{\max}, 6v_{\max})$. The SNR is defined as SNR $= \frac{||\sum_i^I \mathbf{X}_i \odot \mathbf{\Omega}_{\theta r}(\theta_i) \odot \mathbf{\Omega}_{dr}(v_i)||_F^2}{||\mathbf{N}||_F^2}$.

4

4.5.1. MULTIPLE TARGETS SIMULATION AND TIME CONSUMPTION COMPARISON

In the first case study, the general estimation performance of the proposed norm-based method and that of the FFT-based method are compared. 10 random point-like moving targets are set in the observation scene and are illuminated by FMCW waveform. The reflected signals are received by the antenna array and are sampled with sampling frequency $f_s = 640$ kHz ($K = 512$ snapshots for each fast-time) and the SNR is set to 10 dB. The simulation results are shown in Fig. 4.2, where the labels in the legend are: *FFT* denotes the FFT-based algorithm, *Norm* denotes the proposed spectral norm algorithm and implemented by default *norm* function and *PI* denotes the proposed algorithm implemented by the power iteration algorithm.

Here, to illustrate the off-grid problem of the FFT-based method, two sets of simulation for this method are performed with $\kappa - 1$ times zero-padding (κ times FFT points). In the first case, (4.2) is applied with 1 time ($\kappa = 2$) zero-padding. The angle-range and range-velocity results are shown in Fig. 4.2(a)(b), respectively. Since the DOAs have no ambiguity problem for the system, despite minor errors, the DOAs are almost correctly estimated. However, most of the velocity estimates have large errors due to the off-grid problem.

The situation is better when 3 times zero-padding is applied ($\kappa = 4$) and the results are shown in Fig. 4.2(c)(d), where 2 targets still appear with incorrect ambiguity number estimation. Although it can be expected that better results can be obtained with increasing of κ, the time- and memory-consumptions become unacceptable for automotive application.

Fig. 4.2(e)(f) and Fig. 4.2(g)(h) show much accurate estimation of the scene by using the proposed norm-based methods with and without the power iteration algorithm, respectively. The estimation of the angles is more accurate than that in

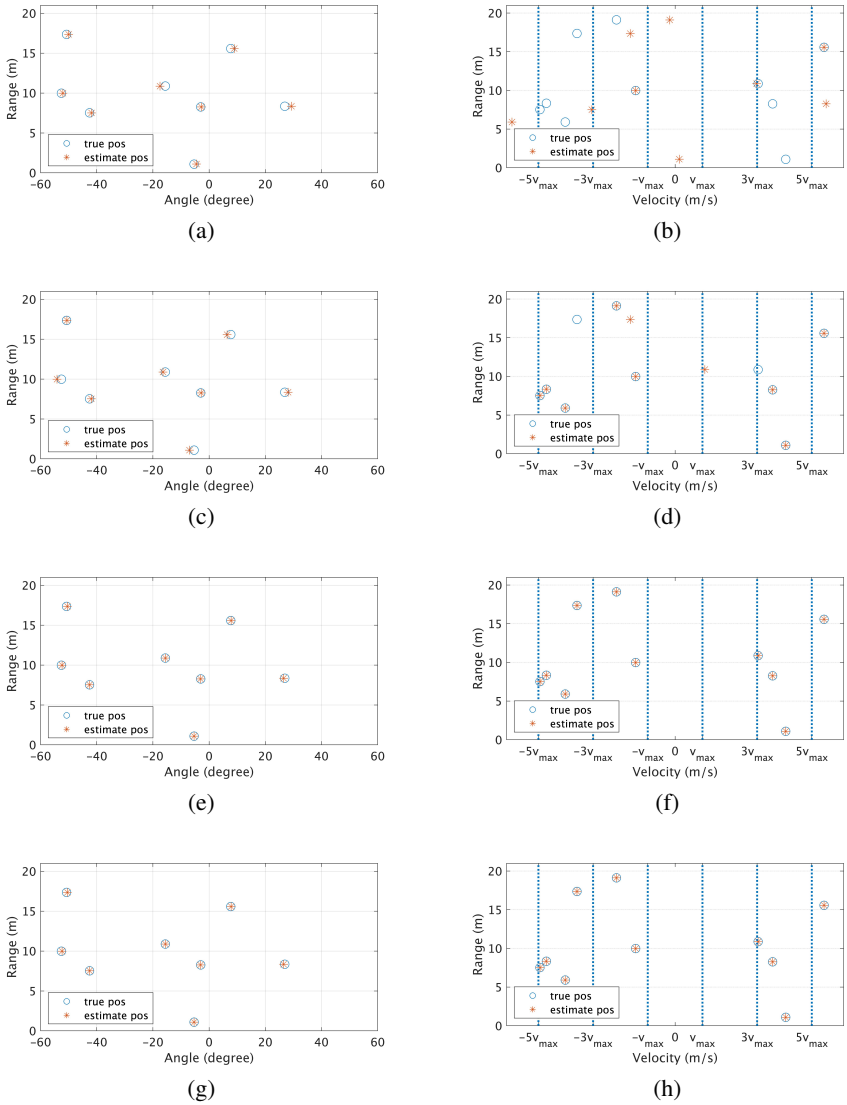

Figure 4.2: Angle-range and velocity-range maps for (a)(b) FFT-based algorithm with 1 ($\kappa = 2$) time zero-padding, (c)(d) FFT-based algorithm with 3 ($\kappa = 4$) times zero-padding, (e)(f) proposed norm-based method, (g)(h) proposed efficient implementation.

Fig. 4.2(a)(c) and there is no estimation error of fold number in Fig. 4.2(f)(h). Additionally, the proposed efficient implementation has similar performance with the default $norm$ function.

The estimation error of fold number $\sum_i^I |n_i - \tilde{n}_i|$ and RMSEs of unambiguous

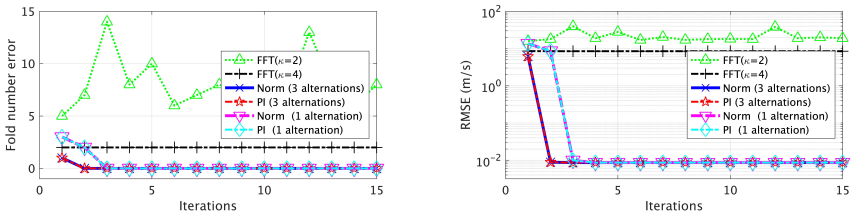

(a) (b)

Figure 4.3: (a) Fold number estimation errors with iteration, (b) RMSEs of ambiguous velocities with iteration

4

velocity are shown in Fig. 4.3 and here we assume the number of targets I is known. It is shown that for 10 far-separated targets, the RELAX algorithm with proposed methods converges within 3 iterations. However, the FFT-based algorithm with 1-time zero-padding cannot converge to a stable point and with 3 times zero-padding converges with the wrong fold number estimation. The RMSEs of unambiguous velocity estimation in Fig. 4.3(b) strongly correspond to the estimation errors of the fold number in Fig. 4.3(a), while the proposed spectral norm-based algorithms with and without efficient implementation can reach 0 error of fold number estimation. Additionally, the proposed algorithm with only 1-time alternation in **A**5 is also applied and the simulation results in Fig. 4.3 demonstrate that with more alternations in **A**5, **A**7 can converge faster.

In addition to the better accuracy of the proposed algorithm, the comparison of the time consumption of different algorithms is listed in Table 4.1. The simulation results show that the proposed algorithm implemented with the power iteration algorithm is preferable in both accuracy and efficiency.

Table 4.1: Time consumption comparison

Algorithm	**A**2	**A**3 per iteration
Norm-based (power iteration)	12.70 s	8.27 s
Norm-based (default norm function)	19.07 s	9.77 s
FFT-based ($\kappa = 2$)	31.14 s	13.57 s
FFT-based ($\kappa = 4$)	217.79 s	54.45 s

4.5.2. LOW SNR AND WITH DIFFERENT ALTERNATIONS

The previous simulation has shown that **A**5 could accelerate the convergence of **A**7, and in this subsection, the superiority of **A**5 under low SNR condition with multiple targets is presented as well. To reduce the integrated SNR, the fast-time samples

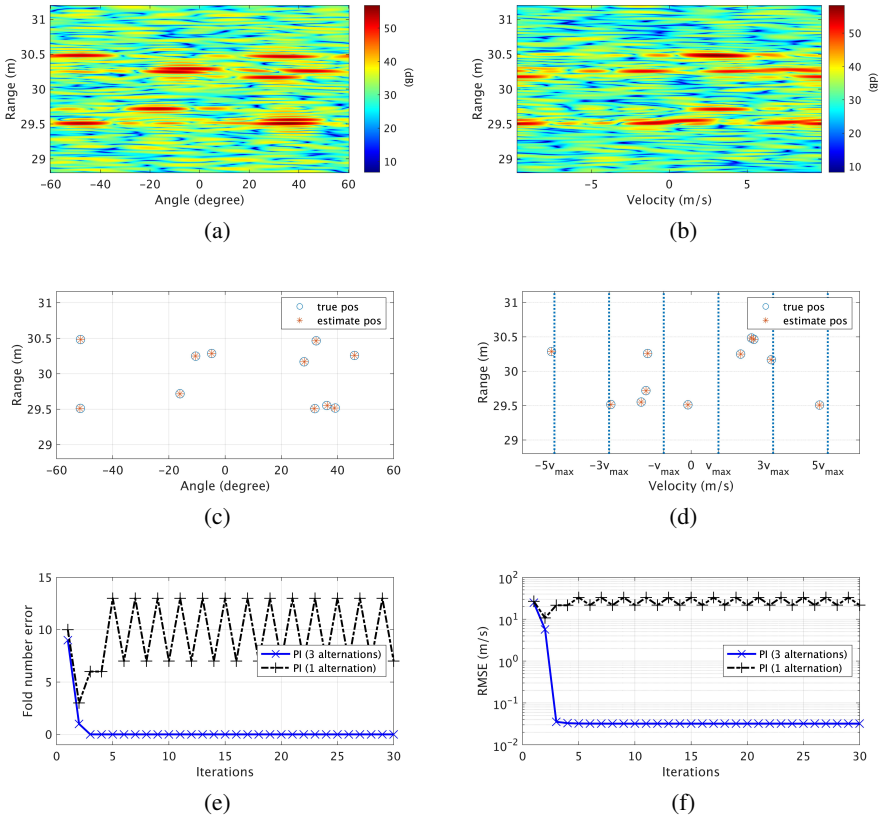

Figure 4.4: Simulation results: (a) angle-range spectrum for $M = 0$, (b) range-velocity spectrum for $L = 0$, (c) angle-range map using proposed algorithm with power iteration, (d) velocity-range map using proposed algorithm with power iteration, (e) fold number errors with different alternations and (f) RMSEs of ambiguous velocity estimation with different alternations

are decreased to $K = 64$ and SNR is set to SNR $= 5$ dB. The other 11 point-like targets are randomly positioned in the observation scene. The results of applying FFT to the raw data of the first slow-time sample ($M = 0$) and the first antenna element ($L = 0$) are shown in Fig. 4.4(a)(b), in which the migration phenomenon is hardly seen from the range-velocity map. The estimation results with the proposed algorithm are shown in Fig. 4.4(c)(d). The proposed algorithm can estimate all the targets with high accuracy. Then to prove the importance of **A**5, the alternation is decreased to 1 repeat and the corresponding fold number estimation error and the RMSE of the unambiguous velocities are plotted in Fig. 4.4(e)(f). It is clear that without sufficient alternations, **A**7 could not reach the convergence, while with only 3 repeats of **A**5, **A**7 converges within 5 iterations.

4.5.3. RMSE COMPARISON OF NORM VERSUS FFT

To show the off-grid problem clearer, two sets of simulations are performed for only one target, which either is an on-grid target or an off-grid one. To save the simulation time on Monte Carlo trials, the fast-time snapshots are set to $K = 64$. The parameters for the on-grid target are $r = 16\frac{\Delta r}{\kappa}$, $v = 20\frac{2v_{\max}}{\kappa M}$, $\theta = 40°$ and the off-grid target is located in between of two FFT grids both for range and velocity as $r = 16.5\frac{\Delta r}{\kappa}$, $v = 20.5\frac{2v_{\max}}{\kappa M}$ and $\theta = 40°$, where κ means $\kappa - 1$ times zero-padding for the (4.2).

The RMSEs and the corresponding CRB comparisons are shown in Fig. 4.5 for $\kappa = 4$ (see Appendix A for CRB derivation). One can see from Fig. 4.5 that, for the on-grid target, both norm-based and FFT-based algorithm can reach the CRBs for all the parameters. It is also observed that the proposed method can reach the CRB around -5 dB for the ambiguous velocity, while the FFT-based algorithm reaches the CRB around 0 dB.

Even though, we have to admit that under the very low SNR condition, coherent integration methods might have better estimation performance than proposed method since the RMSEs of FFT-based method are much lower than that of the proposed algorithm for SNR in $(-20, -10)$ dB.

Consider the off-grid target, the RMSE of the velocity using the FFT-based method cannot reach the CRB but keeps an approximately constant value of $2v_{\max}$. This is because the fold number is estimated incorrectly. The wrong estimation of the unambiguous velocity decreases the accuracies of the DOA, range and amplitude as well.

4.5.4. RMSES COMPARISON OF BANDWIDTH 1 GHZ VERSUS 4 GHZ

From the signal model, we can speculate that with larger bandwidth, the phase of the coupling terms will vary more significantly and therefore have higher SNR tolerance. It means the parameters extraction from the coupling terms can be more accurate with larger bandwidth in the low SNR conditions. Thus, in this study, the performance of the proposed methods with different bandwidth, namely 1 GHz and 4 GHz, is tested. Two separate targets are set in the observation scene. The the parameters of two targets are $v = [50, 60]$ m/s, $\theta = [30°, 10°]$, $r = [0.5, 0.8]$ m, respectively.

Fig. 4.6 gives the results of the RMSEs and the corresponding CRB comparisons. According to Fig. 4.6, the performances for angle and the amplitude are almost identical and this demonstrates that the proposed method is adaptive to signals with different bandwidths for DOA estimation. It is also observed that the CRB of range for 4 GHz is lower than that for 1 GHz simply because the wider frequency band provides higher range resolution. Moreover, the RMSE of the unambiguous

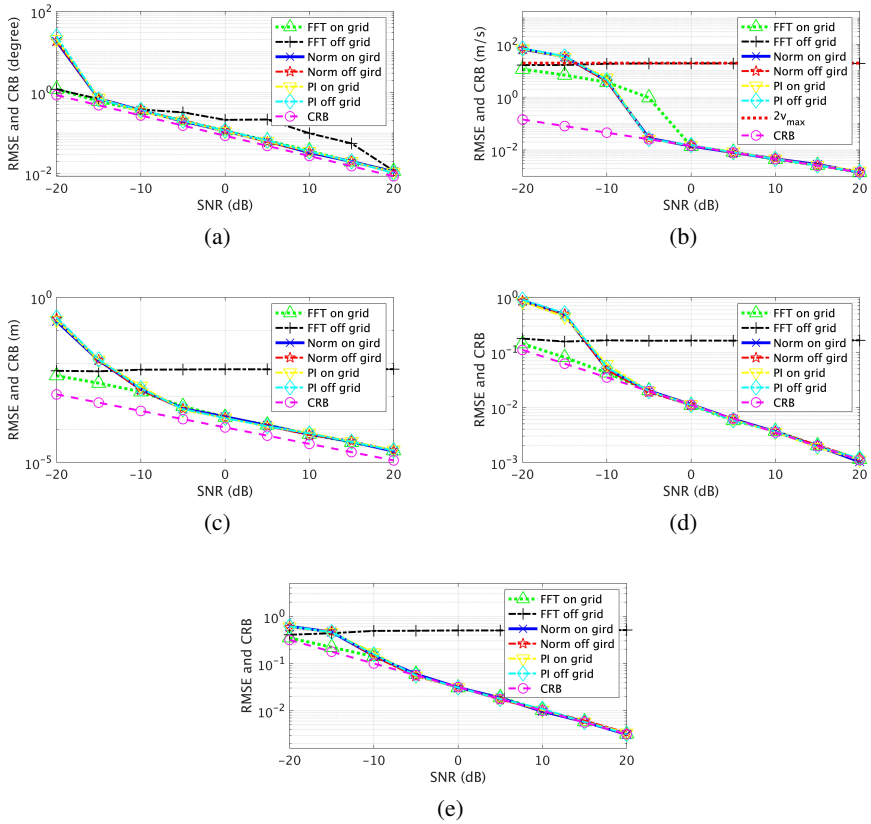

Figure 4.5: RMSEs and CRB comparisons for a single point-like target of (a) angle $\tilde{\theta}$, (b) velocity $\tilde{v}$, (c) range $\tilde{r}$, (d) real part and (e) imaginary part of the amplitude $\tilde{\alpha}$

velocity reaches the CRB from the lower SNR condition at -2.5 dB for 4 GHz signal, while that for 1 GHz signal reaches the CRB from around 5 dB. The simulation results indicate that a possible way to resolve the fold number under very low SNR condition with constrained data size is to increase the bandwidth.

4.5.5. RMSEs OF CLOSELY POSITIONED TARGETS

The super-resolution ability of the RELAX algorithm has been shown in [2]. While the proposed method is applied to a more general signal model, the estimation performance for the close targets is evaluated in numerical simulations in this subsection. Two targets with the same angles and Doppler shifts but half range resolution distance separated are set in the observation scene. The parameters are $v = [50, 50]$ m/s, $\theta = [30°, 30°]$, $r = [0.5, 0.5 + \dfrac{\Delta r}{2}]$ m, respectively.

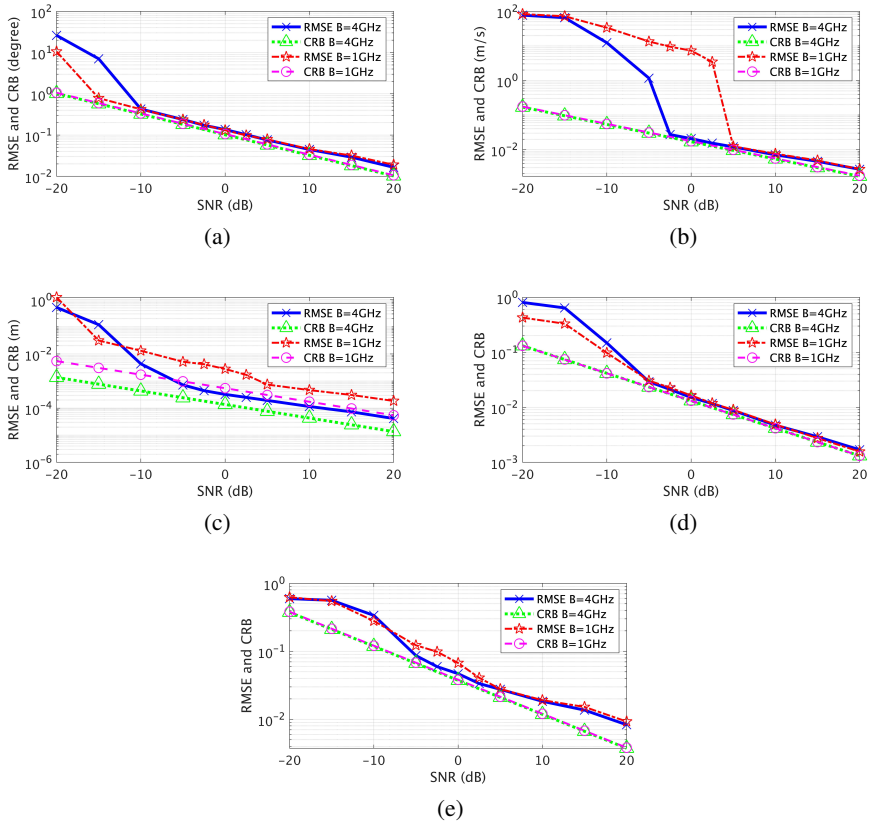

Figure 4.6: RMSEs and CRB comparisons for two far-separated targets of (a) angle $\tilde{\theta}$, (b) velocity $\tilde{v}$, (c) range $\tilde{r}$, (d) real part and (e) imaginary part of the amplitude $\tilde{\alpha}$

The comparisons of the RMSEs and the corresponding CRBs using the proposed algorithm with efficient implementation are shown in Fig. 4.7(a)-(e). Although the performance is not as good as that for two far-separated targets in Fig. 4.6, the RMSEs of all the parameters decrease with the CRB from SNR $= 0$ dB. Among all the parameters, the RMSE of unambiguous velocity estimation has the best performance and almost reaches the CRB.

Moreover, the RMSE trends and the simulation results show that the two closely spaced targets are successfully resolved from each other, which validates that the proposed algorithm holds the super-resolution ability of **A**7. It is worth noting that for two closely positioned targets, much more iterations (around 50 iterations) are needed for convergence and the range residuals with iterations are plotted in Fig. 4.7(f), where the range residual of pth iteration is defined as $|\tilde{r}^{(p)} - \tilde{r}^{(p-1)}|$.

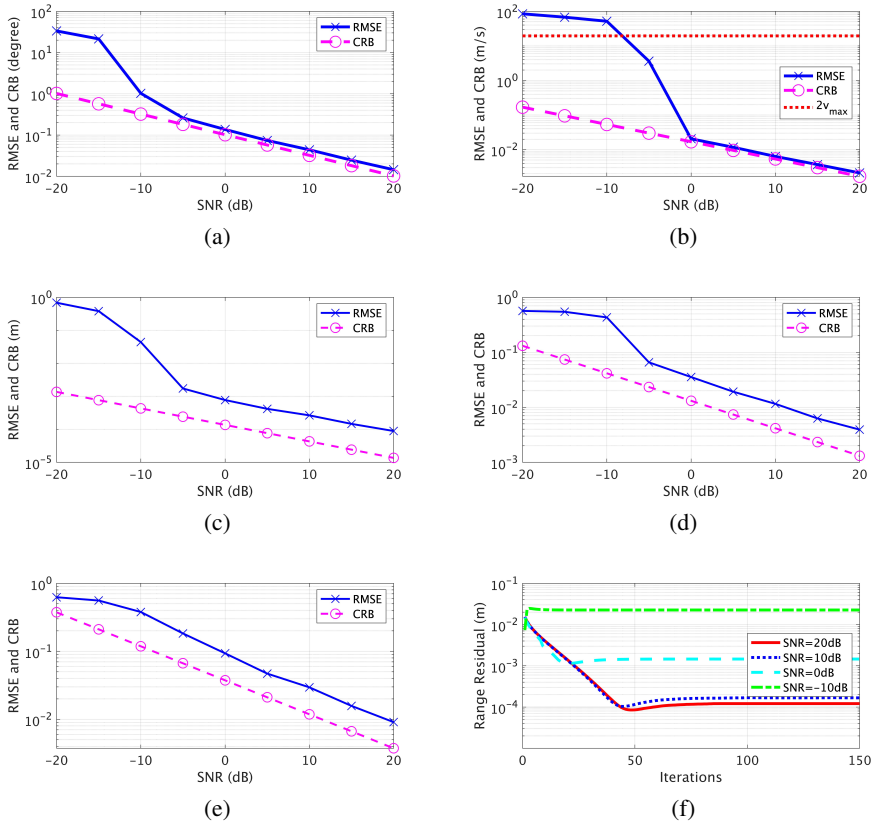

Figure 4.7: RMSEs and CRB comparisons for two close targets of (a) angle $\tilde{\theta}$, (b) velocity $\tilde{v}$, (c) range $\tilde{r}$, (d) real part and (e) imaginary part of the amplitude $\tilde{\alpha}$, and (f) the range residual with iteration number.

4.6. COMPARISON WITH COMPENSATED MUSIC AND SUGGESTIONS

Since we have proposed two algorithms for the coupling terms compensation algorithm, the differences between them and the suggestion for different applications should be discussed.

The main difference is that the compensated MUSIC algorithm treats the coupling terms as redundant phases which are expected to be eliminated, while in this chapter extra information, the Doppler ambiguity number, is extracted from the coupling terms. Obviously, the problem in the previous chapter is a special case of the problem addressed in this chapter. Therefore, the algorithm introduced in this chapter can be applied, without any problem, to the issue in the previous chapter.

Although the spectral norm-based algorithm has wider applications, it clearly has some limitations as well.

Firstly, although the efficient implementation is proposed, the RELAX algorithm consumes much more time than MUSIC algorithm, and more importantly, the time consumptions increase exponentially with the model order and can only be applied to signal model with sparse targets. Secondly, as shown in the simulations that the performance of spectral norm require higher SNR to be applicable.

Thus, the suggestion between two algorithms is that when the velocity of the objects is relatively slow, the MUSIC algorithm is the optimal option, while when the scenario comes to sparse targets but with very high velocities, the RELAX algorithm seems a better choice.

4.7. CONCLUSIONS

In this chapter, a novel algorithm has been proposed to address the joint features extraction of multiple fast-moving targets using (ultra-)WB FMCW signals considering both Doppler ambiguity and wideband DOA problems. The kernel of the algorithm combines several parts: a spectral norm-based parameters extraction from the coupling components and an alternative parameter refinement method is introduced for a single target, then the Greedy algorithm for initialisation and RELAX algorithm for optimisation of the results are applied for multiple targets. An efficient implementation of the proposed algorithm is further introduced by the power iteration algorithm. The performance of the algorithm proposed is validated by numerical simulations. According to the results of the simulations, the algorithm proposed outperforms the traditional coherent integration method both in accuracy and efficiency when the data size is limited and SNR is sufficient. On top of that, the SNR tolerance of the proposed algorithm is enhanced by increasing the signal bandwidth, which makes the algorithm well-suited for UWB radars. Finally, it is also proved that our approach holds the super-resolution ability of RELAX at the expense of a slight loss of accuracy and a larger number of iterations.

5

MOTION-BASED SEPARATION AND IMAGING OF CLOSELY-SPACED EXTENDED TARGETS

Multiple moving extended-targets separation and imaging using UWB FMCW antenna array are investigated in this chapter. The difference in motion of closely-spaced extended targets is used to separate and image them while their radar signatures overlap in the range-azimuth domain. The conventional inverse synthetic aperture radar (ISAR) concept is adopted to image the targets and separate them by appropriate motion compensation. A novel auto-focusing criterion based on the entropy of the eigenspectrum and the Fourier spectrum is proposed. It allows separating closely spaced targets and estimating their motion parameters and it overcomes the low Doppler resolution of closely-spaced extended targets of conventional techniques. Afterwards, the bearing information is extracted by signal reconstruction for every target separately. With the estimated position and the motion parameters of multiple targets, their images are reconstructed using standard imaging processing algorithms. The performance of the proposed method is validated via numerical simulations.

5.1. INTRODUCTION

The range migration problem of point-like targets in the UWB FMCW signal model has been thoroughly considered in previous chapters. The point-like target assumption is appropriate when the targets are far away from the sensors and the Doppler differences of the scatterers within one target due to the target rotation is much smaller than the Doppler frequency resolution. By extending the illumination time, the resolution of the Doppler frequency can be enhanced and such Doppler differences can be observed. According to such differences, the "*shape*" of the target could be obtained from the range-Doppler image for further target recognition. This is the basic idea of ISAR and the main difference to SAR is that the relative velocities of the targets and the sensors are unknown. Although the ISAR auto-focusing algorithms have been very mature for a single target, most algorithms would fail to separate multiple closely-positioned targets in intensive traffic.

To overcome such drawback, a novel algorithm based on the entropies of both eigenspectrum and Fourier spectrum is introduced to estimate the motion parameters and obtain a better separation of multi-targets on Doppler shifts when they have slightly different velocities and the same accelerations. Since the eigenspectrum has a much higher sensitivity to the second-order mutual coupling introduced by the first-order motion, i.e. the constant velocities, targets with similar velocities might be separated while they cannot be separated by the conventional entropy minimisation of Fourier spectrum. However, the eigenspectrum is weakly sensitive to the asymmetric mutual coupling and insensitive to the auto-coupling. Thus, it is difficult to estimate the higher-order motion parameters from eigenspectrum accurately. Therefore, a simple method to combine both entropies is introduced and the high resolutions for both velocities and accelerations are achieved. To alleviate the noise influence as much as possible, the entropy maps are denoised by total variation (TV) algorithm before combination and the local minima are detected with a threshold of prominence. Then the range histories are aligned and Keystone transform are utilised to eliminate the phase error within the unambiguous domain. The FFT is applied to image the focused targets and the thresholding is adopted to separate different targets sequentially. The range-Doppler map can be further reconstructed by combining the imaging results of multiple targets.

The rest of this chapter is organised as follows. The signal model for multiple targets illuminated by UWB FMCW signals is established in Section 5.2. A new criterion for auto-focusing ISAR imaging is introduced in Section 5.3. Numerical simulations are presented in Section 5.4 and the conclusions are drawn in Section 5.5.

5.2. SIGNAL MODEL

In this section, the signal model of multiple extended targets using wideband FMCW is formulated and the scenario with the coordinates is illustrated in Fig. 5.1.

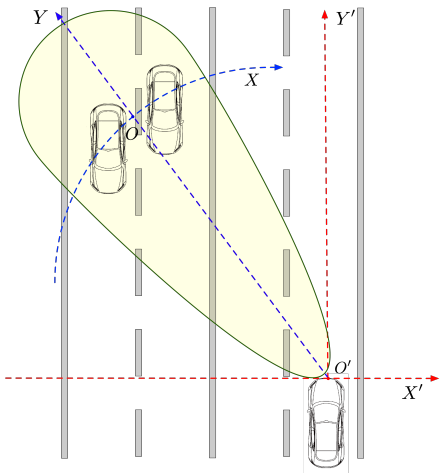

Figure 5.1: Scenario with coordinates

Since the scatterers from one target could have different velocity projection on the line of sight (LOS) and the corresponding received signals contain different Doppler information as well, a scattering centroid is usually chosen as a reference phase centre. Generally, the scattering centre can be chosen randomly close to the geometric centroid of the target. Consequently, the scattering centre is usually not unique but located in a bounded region. Assume the instantaneous range of the scattering centre is expressed as the second-order polynomial

$$R_i(t_m) = R_{i0} + v_i t_m + \frac{1}{2} a_i t_m^2, \tag{5.1}$$

where $t_m = mT$ is the slow-time, R_{i0} denotes the initial range of the scattering centre of the ith target and the corresponding motion parameters, velocity and acceleration are denoted by v_i and a_i, respectively. Here, the fast time t' is directly omitted since $t' << t_m$. Moreover, the higher-order motion parameters are ignored since it is sufficiently accurate to describe the movements of the targets with the second-order Taylor polynomial in a short time [58, 86]. It is worth noting that, the proposed algorithm would also work for higher-order motions at the price of an increased computational burden.

The instantaneous range of the jth scatterer includes the polynomial term $R_i(t_m)$ and the triangular terms which denote the relative range to the phase centre and the projection of the cross-range on the LOS. Therefore, the instantaneous range of the

jth scatterer of ith target is given as [37, 51]

$$\begin{aligned} R_{ij}(t_m) &= R_i(t_m) + y_{ij}\cos(\omega_i t_m) + x_{ij}\sin(\omega_i t_m) \\ &\approx R_{i0} + v_i t_m + \frac{1}{2}a_i t_m^2 + y_{ij} + x_{ij}\omega_i t_m, \end{aligned} \tag{5.2}$$

where y_{ij} and x_{ij} denote range and cross-range relative to the scattering centre of jth scatterer of ith target and $y_{ij}, x_{ij} \ll R_{i0}$, ω_i is the rotational speed of ith target, which is provided by the tangential velocity. Since the observation time is short, the assumptions $\cos(\omega_i t_m) \approx 1$ and $\sin(\omega_i t_m) \approx \omega_i t_m$ are made to linearise the model [37, 51].

Then the round trip delay of the transmitted waves reflected from the jth scatterer of ith target is then written as

$$\tau_{ij}(t_m) = \frac{2R_{ij}(t_m)}{c}, \tag{5.3}$$

where c is the speed of the light.

Insert (5.2) in (5.3), the round-trip delay is written as

$$\begin{aligned} \tau_{ij}(t_m) &= \frac{2R_{ij}(t_m)}{c} \\ &= \frac{2}{c}\left(R_{i0} + v_i t_m + \frac{1}{2}a_i t_m^2 + y_{ij} + x_{ij}\omega_i t_m \right) \\ &= \frac{2(R_{i0} + y_{ij})}{c} + \frac{2(v_i + x_{ij}\omega_i)}{c}t_m + \frac{a_i}{c}t_m^2. \end{aligned} \tag{5.4}$$

By choosing a proper scattering centre, the target "*shape*" could be constructed by y_{ij} and $x_{ij}\omega_i$. Here, the "*shape*" is a distorted shape in the XOY plane, and if the ω_i can be correctly estimated, the real spatial shape in $X'OY'$ plane can be reconstructed.

With the time delay in (5.4), the analogously received wave of jth scatterer from ith target is obtained as $r_{ij}(t) = s(t - \tau_{ij}(t_m))$. Then $r_{ij}(t)$ is mixed with the conjugate copy of the transmitted wave and the de-chirped signal of such scatterer

is obtained as

$$
\begin{aligned}
y_i(t_m, t') &= r_{ij}(t_m, t')s^*(t_m, t') \\
&= \alpha_{ij} \exp\{j2\pi[f_0(t - \tau_{ij}(t_m)) + \mu(t' - \tau_{ij}(t_m))^2 \\
&\qquad - f_0 t' - \mu t^2]\} \\
&\approx \alpha_{ij} \exp[-j2\pi(f_0\tau_{ij}(t_m) + 2\mu\tau_{ij}(t_m)t')] \\
&= \alpha_{ij} \exp\Big\{ - j2\pi\Big[f_0\frac{2(v_i + x_{ij}\omega_i)}{c}t_m \\
&\qquad + f_0\frac{a_i}{c}t_m^2 + 2\mu\frac{2(R_{i0} + y_{ij})}{c}t' \\
&\qquad + 2\mu\frac{2(v_i + x_{ij}\omega_i)}{c}t_m t' + 2\mu\frac{a_i}{c}t_m^2 t'\Big]\Big\},
\end{aligned}
\tag{5.5}
$$

where α_{ij} is the complex amplitude of jth scatterer of ith target, and the constant terms $\exp\Big(- j4\pi f_0\frac{R_{i0} + y_{ij}}{c}\Big)$ and $\exp\Big[4\mu\Big(\frac{R_{i0} + y_{ij}}{c}\Big)^2\Big]$ are subsumed by the constant amplitudes term α_{ij}. Here since the observing time is very short, we assume that the amplitudes of all the scatterers do not change within one CPI.

Sampling the data $y_i(t_m, t)$ in terms of the fast time t' with frequency f_s (sampling interval $T_s = \frac{1}{f_s}$), and the data can be stacked as matrix form $\mathbf{X}_i \in \mathbb{C}^{M\times K}$

$$
\begin{aligned}
\mathbf{X}_{ij} = \alpha_{ij}&\mathbf{f}_d(v_i + x_{ij}\omega_i)\mathbf{f}_r^T(y_{ij}) \\
&\odot \mathbf{\Psi}(v_i + x_{ij}\omega_i) \odot \mathbf{\Omega}(a_i) \odot \mathbf{\Theta}(a_i),
\end{aligned}
\tag{5.6}
$$

where $k = 0, 1, ..., K-1$ is the fast time sampling indices and K is the total samples in one chirp, and the sinusoidal vectors $\mathbf{f}_d(v_i + x_{ij}\omega_i) \in \mathbb{C}^{M\times 1}$, $\mathbf{f}_r(y_{ij}) \in \mathbb{C}^{K\times 1}$ are

$$
\begin{aligned}
\mathbf{f}_d(v_i + x_{ij}\omega_i) =&\Big[1, \exp\big(- j4\pi\frac{v_i + x_{ij}\omega_i}{\lambda}T\big), ..., \\
&\exp\big(- j4\pi\frac{v_i + x_{ij}\omega_i}{\lambda}T(M-1)\big)\Big]^T, \\
\mathbf{f}_r(y_{ij}) =&\Big[1, \exp\big(- j8\pi\mu\frac{R_{i0} + y_{ij}}{cf_s}\big), ..., \\
&\exp\big(- j8\pi\mu\frac{R_{i0} + y_{ij}}{cf_s}(K-1)\big)\Big]^T,
\end{aligned}
\tag{5.7}
$$

where $\lambda = \frac{c}{f_0}$ is the wavelength corresponding to the lowest frequency of the band, and the coupling matrices $\mathbf{\Psi}(v_i + x_{ij}) \in \mathbb{C}^{M\times K}$, $\mathbf{\Omega}(a_i) \in \mathbb{C}^{M\times K}$, $\mathbf{\Theta}(a_i) \in \mathbb{C}^{M\times K}$

are defined with entries as

$$[\mathbf{\Psi}(v_i + x_{ij})]_{m,k} = \exp\Big[- j8\pi\mu \frac{v_i + x_{ij}\omega_i}{cf_s} Tmk\Big], \tag{5.8}$$
$$[\mathbf{\Omega}(a_i)]_{m,k} = \exp\Big[- j2\pi f_0 \frac{a_i}{c} T^2 m^2\Big],$$
$$[\mathbf{\Theta}(a_i)]_{m,k} = \exp\Big[- j4\pi\mu \frac{a_i}{cf_s} T^2 m^2 k\Big]$$

The signal model for a single scatterer contains the sinusoidal terms $\mathbf{f}_d(v_i+x_{ij}\omega_i)$ and $\mathbf{f}_r(y_{ij})$, whose Fourier spectrum reveals the distorted shape of the targets by y_{ij} and $x_{ij}\omega_i$. In addition to the sinusoidal terms, there are three extra coupling components. The second-order mutual coupling term $\mathbf{\Psi}(v_i + x_{ij}\omega_i)$ is the function of the Doppler velocity v_i in $v_i + x_{ij}\omega_i$. Here, the velocity v_i can be larger than the maximum unambiguous velocity of the system and will be folded in the unambiguous Doppler interval. This is one of the main problems for targets detection and parameters estimation in most cases when the acceleration of the target is ignored. The high-order phase term $\mathbf{\Omega}(a_i)$ and higher-order asymmetric mutual coupling term $\mathbf{\Theta}(a_i)$ contain the higher-order motion parameters, i.e. the acceleration a_i. To image the ith target in the range-Doppler map, all these coupling terms should be correctly compensated.

The matrix data of a single antenna element are $\mathbf{X}_{ij}$. Now the ULA for receiver is considered and the wideband steering matrix $\mathbf{A}(\theta_{ij}(t_m)) \in \mathbb{C}^{L\times K}$ can be written as [77]

$$\mathbf{A}(\theta_{ij}(t_m)) = \mathbf{a}(\theta_{ij}(t_m))\mathbf{1}_K^T \odot \mathbf{\Phi}(\theta_{ij}(t_m)), \tag{5.9}$$

where $\theta_{ij}(t_m)$ is the azimuth of the jth scatterer of the ith target at the time t_m and the narrowband steering vector is

$$\mathbf{a}(\theta_{ij}(t_m)) = \Big[1, \exp\big(- j2\pi \frac{d}{\lambda} \sin(\theta_{ij}(t_m))\big), ..., \exp\big(- j2\pi \frac{(L-1)d}{\lambda} \sin(\theta_{ij}(t_m))\big)\Big]^T, \tag{5.10}$$

and according to (2.13) the coupling term introduced by the wideband waveform is

$$[\mathbf{\Phi}(\theta_{ij}(t_m))]_{l,k} = \exp\Big(- 2j\pi\mu \frac{lkd}{cf_s} \sin(\theta_{ij}(t_m))\Big). \tag{5.11}$$

Stacking all the slow-time t_0 to t_{M-1} forms the tensor data $\boldsymbol{\mathcal{A}}_{ij} \in \mathbb{C}^{M\times K\times L}$ as

$$\boldsymbol{\mathcal{A}}_{ij} = \begin{array}{c} \mathbf{A}(\theta_{ij}(t_0)) \\ \mathbf{A}(\theta_{ij}(t_1)) \\ \vdots \\ \mathbf{A}(\theta_{ij}(t_{M-1})) \end{array}. \tag{5.12}$$

Now the discretised data $\boldsymbol{\mathcal{Y}}_{ij} \in \mathbb{C}^{M\times K\times L}$ of the antenna array of the jth scatterer of ith target are stacked as a tensor, given by

$$\boldsymbol{\mathcal{Y}}_{ij} = \boldsymbol{\mathcal{A}}_{ij} \odot (\mathbf{X}_{ij} \circ \mathbf{1}_L), \tag{5.13}$$

and the received multi-way data $\boldsymbol{\mathcal{Z}} \in \mathbb{C}^{M\times K\times L}$ in the presence of the noise are written as

$$\boldsymbol{\mathcal{Z}} = \sum_{i}^{I}\sum_{j}^{J} \boldsymbol{\mathcal{Y}}_{ij} + \boldsymbol{\mathcal{N}}, \tag{5.14}$$

where $\boldsymbol{\mathcal{N}}$ is the discrete multi-way additive complex Gaussian white noise with the entries' distribution as $\mathcal{N}(0, \sigma^2)$.

Now the problem is to estimate the motion parameters and image the targets from the tensor data $\boldsymbol{\mathcal{Z}}$.

5.3. MOTION-BASED TARGET SEPARATION AND IMAGING

In this section, we propose a novel method for multiple closely-spaced extended targets separation and imaging. Firstly, the motion parameters of the targets are estimated using the combination of the conventional Fourier spectrum-based entropy and the proposed eigenspectrum-based entropy. Secondly, the ISAR imaging is performed via the range-Doppler processing and a simple thresholding method is applied to separate multiple targets. Thirdly, the azimuths of the targets are estimated correspondingly using the signal reconstruction of the targets. Finally, the observed scene is reconstructed via an image processing technique using the estimated target motion parameters.

5.3.1. MOTION PARAMETERS ESTIMATION

To present the 2D targets in the Fourier spectrum by the conventional range-Doppler algorithm, the range migration needs to be eliminated. To align the range history, or equivalently to compensate the coupling components $\boldsymbol{\Psi}(v_i + x_{ij}\omega_i)$, $\boldsymbol{\Omega}(a_i)$ and $\boldsymbol{\Theta}(a_i)$, the motion parameters of the scattering centre v_i and a_i should be estimated.

However, since the motion parameters of targets usually are different, the range alignments of all the observed targets cannot be performed simultaneously. The Shannon Entropy of the Fourier spectrum provides an efficient way of estimating the motion parameters for a single extended target and can be applied in the multi-targets scenario if the targets have sufficiently different motion parameters [39, 45, 86]. The Shannon entropy for a vector $\mathbf{s} = [s_1, ..., s_N]$ with positive entries is defined by

$$\text{Entropy}(\mathbf{s}) = -\sum_{n=1}^{n=N} p_n \log p_n, \tag{5.15}$$

where

$$p_n = \frac{s_n}{\sum_n s_n}. \tag{5.16}$$

According to the definition of the Shannon entropy, when the targets are correctly focused by motion compensation, the FFT result yields a minimum entropy value. In terms of velocity v and acceleration a, the range alignment is performed via phase compensation as

$$\begin{aligned}\hat{\mathbf{Y}}(v,a) &= \mathbf{Y} \odot \mathbf{\Psi}^*(v) \odot \mathbf{\Omega}^*(a) \odot \mathbf{\Theta}^*(a) \\ &= \alpha_{ij}\mathbf{f}_d(v_i + x_{ij}\omega_i)\mathbf{f}_r^T(y_{ij}) \\ &\quad \odot \mathbf{\Psi}(v_i - v + x_{ij}\omega_i) \\ &\quad \odot \mathbf{\Omega}(a_i - a) \odot \mathbf{\Theta}(a_i - a),\end{aligned} \tag{5.17}$$

where $\mathbf{Y} = [\boldsymbol{\mathcal{Z}}]_{:,:,0}$ is the data of the first antenna element. With the power spectrum $\mathbf{P}(v,a) = (\mathscr{F}\hat{\mathbf{Y}}(v,a)) \odot (\mathscr{F}\hat{\mathbf{Y}}(v,a))^*$, the motion parameters are estimated via the optimisation:

$$\tilde{v}, \tilde{a} = \underset{v,a}{\text{argmin}}\ \text{Entropy}[\textbf{vec}(\mathbf{P}(v,a))]. \tag{5.18}$$

The conventional Fourier spectrum-based Shannon entropy works properly when the motion parameters of different targets - velocities or accelerations - are significantly distinct. However, the Fourier spectrum has relatively low sensitivity on the second-order mutual coupling, therefore, it may be difficult to separate the targets when they are moving with slightly different velocities and similar acceleration.

To overcome this problem, we propose a novel approach based on Shannon entropy of the matrix eigenspectrum for motion parameters estimation given by

$$\begin{aligned}\mathbf{R}(v,a) &= \hat{\mathbf{Y}}(v,a)\hat{\mathbf{Y}}^H(v,a), \\ \tilde{v}, \tilde{a} &= \underset{v,a}{\text{argmin}}\ \text{Entropy}[\boldsymbol{\sigma}(\mathbf{R}(v,a))].\end{aligned} \tag{5.19}$$

It is worth noting that $\mathbf{R}(v,a) = \hat{\mathbf{Y}}^H(v,a)\hat{\mathbf{Y}}(v,a)$ can also be used for EM. Moreover, since the eigenspectrum is insensitive to the auto-coupling terms, the $\hat{\mathbf{Y}}(v,a)$ can be replaced by $\hat{\mathbf{Y}}(v,a) = \mathbf{Y} \odot \mathbf{\Psi}^*(v) \odot \mathbf{\Omega}^*(a)$, where the term $\mathbf{\Theta}^*(a)$ is omitted for computational simplicity. The proposed approach is based on the fact that the off-grid eigenspectrum has a much higher sensitivity to the second-order mutual coupling terms than grid-based Fourier spectrum and has no side-lobes issues.

Although the proposed entropy has higher velocity resolution, it is much less affected by the coupling terms $\mathbf{\Theta}(a_i)$ and $\mathbf{\Omega}(a_i)$. This is because these coupling terms have much less influence on the orthogonality of the eigenvectors. Therefore, it is possible to have two entropy maps together, where the Fourier spectrum-based entropy has a higher resolution for the higher-order motion parameters while eigenspectrum-based entropy has a higher resolution for the first-order motion parameters. A straightforward approach is to combine these two entropies to obtain high-resolution separation both on velocity and acceleration.

Before combining them, the entropy maps should be normalised into the same scale. We propose to use the normalisation towards the interval $[0, 1]$ by

$$N(I) = \frac{I - \min(I)}{\max(I) - \min(I)}, \tag{5.20}$$

where I denotes the entropy map constructed by the entropy value of all the searching grid on velocity and acceleration, and $\max()$ and $\min()$ return the maximum and minimum value of the map. To benefit from the high sensitivities to different motion parameters, we propose the novel metric obtained from both entropy maps:

$$S = -[1 - N(F)][1 - N(\Sigma)], \tag{5.21}$$

where F and Σ are the entropy maps of Fourier spectrum and eigenspectrum, respectively. Then the motion parameters can be estimated by finding the local minima of the combined entropy map of S.

To automatically detect the targets and estimate the motion parameters, some further steps should be performed. Since both entropy maps contain noise, there might be many local minima introduced by the noise. To alleviate the influence of noise, the TV denoising algorithm [87] is applied to the combined entropy. This processing removes most of the local minima. The locations of the left local minima would indicate the motion parameters of the targets.

5.3.2. TARGET IMAGING AND SEPARATION

With the estimated parameters from the previous step, the targets can be imaged separately by appropriate range alignments. By the coupling terms compensation for the scattering centre, part of the signal distortion due to the range migration will

be eliminated. However, that is not sufficient to obtain a well-focused image due to the Doppler differences of the scatterers to the phase centre. The Keystone transform is performed to the aligned data within the maximum unambiguous Doppler interval [58]. The process is illustrated as

$$\mathscr{F}\{\text{Keystone}[\mathbf{Y} \odot \mathbf{\Psi}^*(\tilde{v}) \odot \mathbf{\Omega}^*(\tilde{a}) \odot \mathbf{\Theta}^*(\tilde{a}) \odot (\mathbf{f}_d(\tilde{v})\mathbf{1}_K^T)^*]\}, \tag{5.22}$$

where Keystone denotes the Keystone transform operation and the term $(\mathbf{f}_d(\tilde{v})\mathbf{1}_K^T)^*$ is used to put the scattering centre in the centroid of the spectrum. If the estimation results are located within the acceptable boundary, all the scatterers of one target are shifted into the observation window without Doppler ambiguity, and the FFT and Keystone transform will generate a focused image.

Here we also assume that the targets would not be focused at the same time; otherwise, they will be recognised as the same target. According to this assumption, when one target is focused, the others would not be entirely focused. Then, the multiple targets can be separated with CLEAN techniques or the thresholding method [56]. If the targets are constructed of too many scatterers, it is time-consuming to apply the CLEAN technique, therefore, the simpler thresholding is adopted in this chapter for target detection and separation. From the separated focused range-Doppler map, the distorted shape of the targets can be recognised and parameters of all the dominant scatterers $\tilde{y}_{ij}$ and $\tilde{x}_{ij}\tilde{\omega}_i$ are estimated.

5.3.3. AZIMUTHAL BEAMFORMING

Multiple targets may not be separable in the azimuthal domain by means of traditional BF techniques if they are closely positioned. Although the subspace-based methods can provide super-resolution ability, most of them are applicable for only the point-like targets and not suitable for extended targets considered in this study [77]. Fortunately, since the targets have been separated from the previous steps, the corresponding azimuthal information can be estimated separately.

Because the azimuths of the targets are slightly changing with time, to accurately estimate the azimuths of the targets, the data $\mathbf{Z} = [\boldsymbol{\mathcal{Z}}]_{0,:,:}$ of the first slow-time index are used to avoid angle migration.

To estimate the azimuth of a single target, we apply BF with the reconstructed data of each target separately. For the ith target, the reconstructed data for the first slow-time sample and the searching angle grid $\tilde{\theta}$ are

$$\tilde{\mathbf{Z}}_i(\tilde{\theta}) = \tilde{\alpha}_i \mathbf{A}(\tilde{\theta}) \odot \Big(\sum_j^J \mathbf{1}_M \mathbf{f}_r^T(\tilde{y}_{ij}) \Big). \tag{5.23}$$

Then the estimation can be made simply by

$$\tilde{\theta}_i = \underset{\theta}{\operatorname{argmax}} \, |\text{Tr}[\tilde{\mathbf{Z}}_i^H(\theta)\mathbf{Z}]|. \tag{5.24}$$

5.3.4. IMAGING OF THE OBSERVED SCENE

According to the parameters estimated above, we can image the observed scene of multiple moving targets. Here, we assume the ranges of the targets are known, which are easily estimated from the range profile and we also assume that all the targets move along the Y' axis. Then, the image of the observed scene can be obtained by a few steps:

IMAGE RESCALING

Since the image is distorted by the $x_{ij}\omega_i$, the real crossrange x_{ij} is rescaled by dividing the ω_i, where $\omega_i \approx \dfrac{v_i \tan\theta_i}{R_{i0}}$.

ROTATION AND LOCATION

The map in coordinate XOY has to transform to real geometric coordinate $X'OY'$ according to the angle θ_i for the ith target separately. Finally, based on the estimated positions of the centroid of the targets θ_i and R_i, the focused images of all the targets are placed in the corresponding positions.

5.4. SIMULATIONS

In this section, the simulation results are presented to demonstrate the performance of the proposed algorithm and further discussions on the proposed algorithm are also provided.

5.4.1. NUMERICAL SIMULATIONS

The automotive scenario is considered and the radar has the following parameters. The bandwidth of FMCW signal is $B = 4$ GHz with starting frequency $f_0 = 77$ GHz, the chirp duration is $T_0 = 320$ μs and the chirp repetition interval is $T = 400$ μs. $M = 156$ chirps are transmitted in a burst and the reflected signals are received by the ULA with $L = 8$ antenna elements. After the de-chirping process, the data are sampled with the sampling frequency of $f_s = 625$ kHz. Then the received data in the multi-way form $\boldsymbol{\mathcal{Z}} \in \mathbb{C}^{156\times200\times8}$ are used to estimate the motion parameters. As for the target, each car model is represented by 137 dominant points scatterers as shown in Fig. 5.2. The amplitudes of all the scatterers are set from uniform distribution $\alpha_{ij} \sim \mathcal{U}(0.8, 1)$. The SNR is set to 10dB with additive complex Gaussian noise.

To validate the performance of separating multiple closely-spaced targets, two cars are set in the observed domain, which cannot be separated from the beam and range profile. The exact geometry of the two cars is shown in Fig. 5.3, where the radar is located in the position of $(0, 0)$. This scenario is very common in the real world, where two cars are close to each other and partially overlapped with each

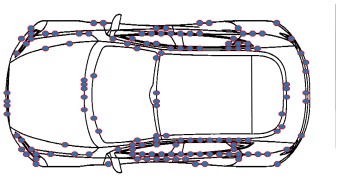

Figure 5.2: Car model with 137 point scatters

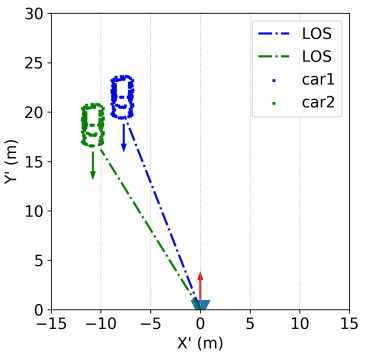

Figure 5.3: The geometry of the simulations

other in both beam and range. It is worth noting that the real geometry is indicated by axis X' and Y', while the ranges X of the LOS are indicated by the dashed lines. The velocities of car1 and car2 are set as 20.87 m/s and 20.62 m/s along the negative Y' axis. We assume the radar is mounted on the vehicle which has a velocity of 19.44 m/s along the positive Y' axis. Thus, the total relative velocities of the cars to the radar are -40.31 m/s and -40.06 m/s along the Y-axis and the velocity projections of the scattering centre of the targets on the LOS are -37.89 m/s and -34.69 m/s, respectively. Moreover, the accelerations of both targets are set to $a_i = 0$ m/s^2 to test the capability of separating two cars from the Doppler differences.

According to the parameter setting of the system and the objects, the discrete received data in tensor form are established using the signal model (5.14). It is worth noting that in reality, only half of these scatterers can be illuminated by the radar due to the propagation of the radio wave, but for simulation, we assume all these scatterers are observed by the radar. In the signal model, the relative velocities of the cars along the Y' axis are divided into two orthogonal components, the radial parts $v_{\parallel}$ in the direction to the radar and tangential parts $v_{\perp}$ which is orthogonal to the radial parts $v_{\parallel}$ and provide the rotational speeds of the targets as $\omega = \frac{v_{\perp}}{R}$. Here,

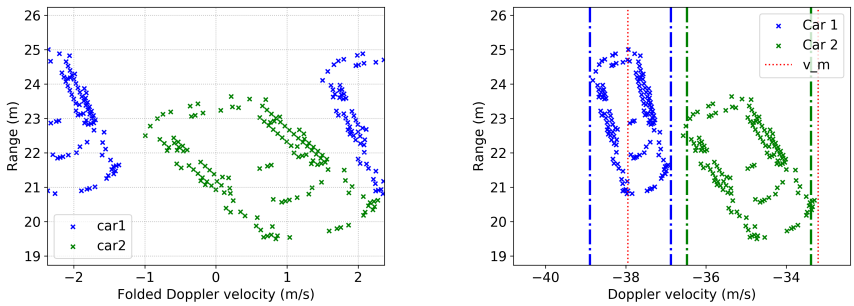

(a) (b)

Figure 5.4: Range-Doppler map for (a) range-Doppler map in the observed window and (b) unfolded range-Doppler map

since the observing time is very short, we assume the speeds are constant over one CPI.

For comparison, the ideal imaging results of all the scatterers without any coupling components are shown in Fig. 5.4. Fig. 5.4(a) shows the positions of the scatterers of the cars in the observed window in which the velocities are folded within the maximum unambiguous domain. Fig. 5.4(b) illustrates the corresponding unfolded imaging results with the green and blue dashed lines indicating the region of acceptable boundaries of two cars and the space between the red dashed lines indicates the maximum unambiguous domain. All the velocity estimations within the dashed lines (green and blue) would compensate the most coupling influence and bring the target close to the centroid of the observed window. One of the main objectives in the following simulation is the estimation of the motion parameters of the cars and reconstruction of the unfolded range-Doppler map similar to Fig. 5.4(b).

By applying 1D FFT on the fast-time domain of the data, the range migration phenomenon of two cars is shown in Fig. 5.5(a), in which the range histories of two targets are overlapped with almost the same slope and are hardly separated. Fig. 5.5(b) shows the imaging results without any range alignment applying 2D FFT to the raw data of a single antenna element.

Next, the proposed eigenspectrum based entropy map (5.19), the conventional Fourier spectrum-based entropy map (5.18) and the combination of both entropies (5.21) are applied to the simulated data and the simulation results are shown in Fig. 5.6, where all the entropy results are normalised. The local minimum values are detected with the prominence threshold 0.05 and indicated by the white crosses for all the entropy maps. Here to clearly show the local entropy, we made an assumption

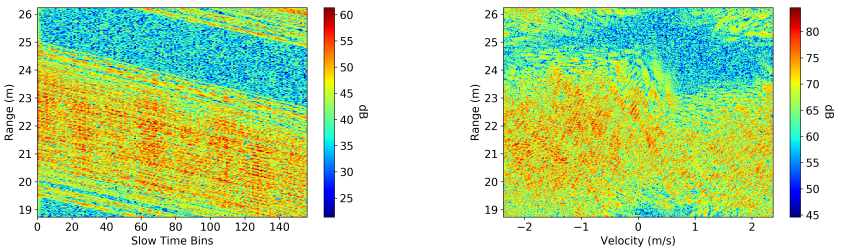

(a) (b)

Figure 5.5: (a) 1D FFT on fast time to show the range migration with slow-time bins and (b) 2D FFT imaging result without motion compensation

that the coarse velocity estimations have been obtained which are in the range from -33 m/s to -40 m/s.

Fig. 5.6(a) shows the proposed entropy map obtained with the eigenspectrum and Fig. 5.6(b) shows the counterpart of using the Fourier spectrum. Since the eigenspectrum is weakly sensitive to the asymmetric coupling terms, the entropy map shows strong thick lines along the acceleration dimension. Although the resolution of the acceleration is low, one can observe that two targets are distinctly resolved in Fig. 5.6(a) from the velocity domain, while they can hardly be separated in Fig. 5.6(b). Therefore, the algorithms for multiple targets imaging of the Fourier spectrum-based EM [56, 58] will fail to image the targets separately. The result of using the proposed combination is shown in Fig. 5.6(c).

One can observe that although the eigenspectrum-based entropy map provides a high resolution on velocity, it yields local minima with poor acceleration estimations. By contrast, the Fourier spectrum-based entropy map has much higher resolution in the acceleration domain but fails to separate two cars in the velocity domain. The targets detection and motion parameters estimation revealed in Fig. 5.6(c) by the proposed algorithm agrees with the ground truth in terms of velocity and acceleration estimation.

To show the superiority of the proposed algorithm, the entropies at the acceleration 0 m/s^2 are plotted in Fig. 5.7. There is a deep valley between two peaks which corresponds to the cars with the proposed algorithm, while the entropy of the Fourier spectrum is much smoother and only one peak could be recognised.

After the motion parameters estimation, the next step is to image the targets separately. According to (5.22), the coupling terms are firstly compensated for the phase centre. Secondly, Keystone transform is applied to eliminate the coupling terms for all the scatterers within the unambiguous region. After that, 2D FFT is used to obtain the range-Doppler map of the cars. Finally, the "*shape*" of the targets

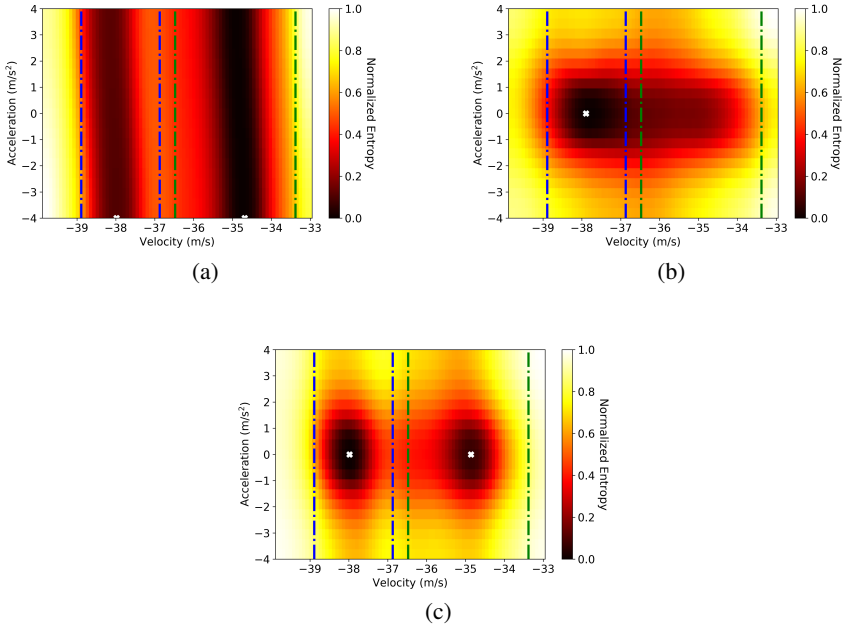

Figure 5.6: The entropy map for (a) the eigenspectrum, (b) Fourier spectrum and (c) the combined entropy by (5.21)

are extracted using thresholding sequentially.

The cars are imaged using 2D FFT followed by 10 dB thresholding and the results are shown in Fig. 5.8. Since two cars are so close in Doppler velocity that they are not able to completely separated for all scatterers and the part of another car would appear in the observed window. The thresholding results are further combined to generate the unfolded range-Doppler map, which is shown in Fig 5.9. Despite some artefacts, the overall map agrees well to Fig. 5.4(b).

Then the BF results using the algorithm described in Section 5.3.3 of two cars are plotted in Fig. 5.10, where the azimuths of the cars are correctly estimated. In comparison, the BF result of using the whole data of the first slow-time is plotted as well, where only one peak can be estimated for a single car.

After estimating the azimuths, the real geometric image can be reconstructed according to the steps proposed in Section 5.3.4 and the imaging results are shown in Fig. 5.11. By comparison with the geometric setting in Fig. 5.3, the two cars are correctly positioned in the observed scene.

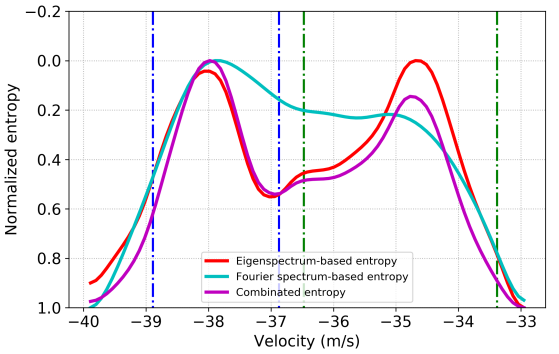

Figure 5.7

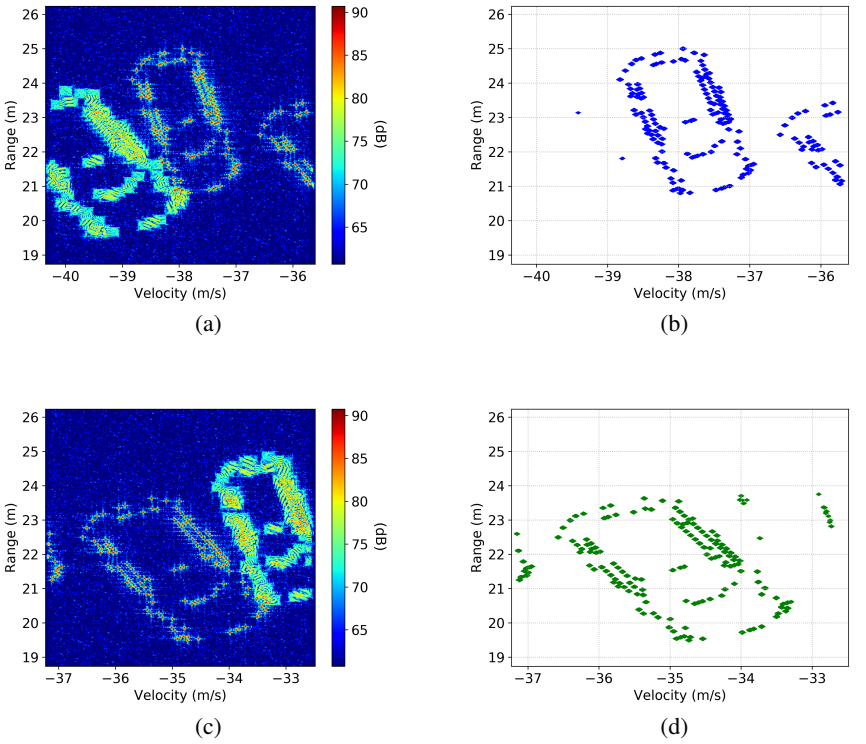

Figure 5.8: (a)(b) Focusing image and thresholding result for car1 and (c)(d) Focusing image and thresholding result for car2

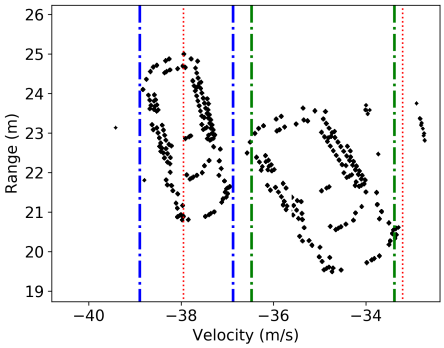

Figure 5.9: Estimated unfolded range-Doppler map

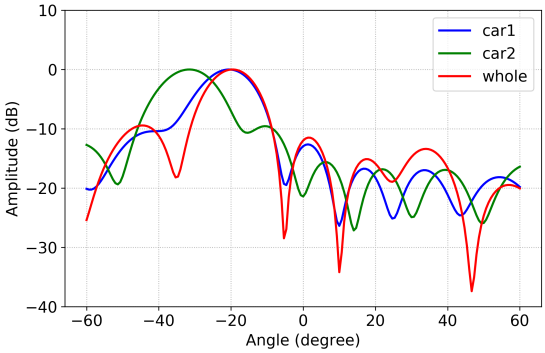

Figure 5.10: Beamforming results

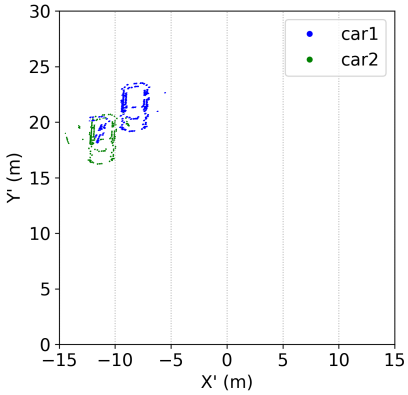

Figure 5.11: Reconstructed Scene

5.4.2. DISCUSSIONS

In addition to the advantages demonstrated in the simulation, the algorithm has some limitations. The first one is that the eigenspectrum is much easier to be contaminated by the noise than the Fourier spectrum. Therefore, the general performance of the proposed method under low SNR condition, for instance, less than 0 dB, is usually worse than that of Fourier spectrum-based entropy. The second limitation is that the entropy of both eigenspectrum-based and Fourier spectrum-based would fail to separate two targets when their energies of the reflected signals are significantly distinct, for instance, more than 10 dB.

5.5. CONCLUSIONS

The motion parameters estimation and range-Doppler imaging of multiple moving extended-targets are addressed in this chapter. To improve the moving targets separation in the Doppler velocity domain when the targets are moving with almost the same accelerations, a novel auto-focusing method based on the entropy of the eigenspectrum is proposed. Combining the proposed eigenspectrum-based entropy and Fourier spectrum-based entropy, both Doppler velocities and higher-order motion parameters can be estimated accurately. After estimating the motion parameters, the azimuths of the extended targets are estimated by reconstructing the corresponding signal model respectively. Finally, the spatial images of extended targets are reconstructed. The numerical simulation results show the applicability of the proposed method to the automotive application. The advantage over conventional algorithm are demonstrated for moderate SNR condition and the limitations of the algorithm are also discussed.

6

SUPER-RESOLUTION DOA WITH FFT-MUSIC ALGORITHM FOR AUTOMOTIVE RADAR IMAGING

Radar imaging for automotive radar is studied and a novel FFT-MUSIC algorithm is proposed and applied to the experimental data. Although many advanced algorithms have been proposed in previous chapters, they have the same limitations. The current computational power limits the applications for these algorithms in real-time processing of automotive radar. In this chapter, an original FFT-MUSIC imaging algorithm is introduced to overcome poor cross-range resolution of traditional beamforming (BF) algorithms. The algorithm provides super-resolution on the DOA profile and provides a clear image of the environment. The experimental data are collected with NXP dolphin radar in Delft campus and processed with conventional beamforming method and proposed FFT-MUSIC algorithm. The performances of both algorithms are thoroughly compared.

6.1. INTRODUCTION

Automotive radar has been significantly growing in popularity in recent years [21, 88–95]. The basic concept of automotive FMCW radar is to generate and transmit a linear frequency ramp as the transmitted signal. By mixing the transmitted and received signals, the beat frequency signal is generated in the receiver. The range profile is obtained by spectrum analysis of such beat frequency. Meanwhile, the angle profile of the targets could be extracted from the phase delay between different radar antenna array elements. Although with MIMO radar the equivalent aperture of the virtual array is up to two times larger as the physical aperture, the angular resolution of conventional BF is extremely limited by the aperture size. To improve the performance of angle-range imaging, so-called super-resolution algorithms, such as 2D MUSIC [96], 3D MUSIC [97] and FFT-ESPRIT [67], have been introduced to automotive radar. However, high-dimensional MUSIC cannot be adopted for real-time implementation due to the high computational load. Moreover, the fast Fourier transform - estimation of signal parameters via rotational invariance techniques (FFT-ESPRIT) algorithm can hardly work in the challenging environment because the 1D FFT of only one element could not provide sufficient SNR to detect the targets [67].

To reduce the imaging complexity and at the same time provide high angular resolution, we present the FFT combined with MUSIC algorithm for the UWB MIMO automotive radar angle-range imaging and the results from measured data are presented and compared with that of conventional BF method. The experimental data are collected from moving cars equipped with NXP radar demonstrator [98]. After the data preprocess and MIMO calibration, the range profile is processed by FFT for high efficiency and MUSIC algorithm is applied to angle profile for high angular resolution. The spatial smoothing is applied to avoid coherent sources and a dynamic threshold is set to detect the number of the sources in each range cell. Moreover, an original dynamic normaliser is also applied to each range cell to approximate the true spectrum image.

The rest of the chapter is organised as follows. Section 6.2 describes how the experimental data are collected and preprocessed. The imaging algorithm is described in detail in Section 6.3. The imaging results are presented and compared in Section 6.4. Main conclusions about the performance are drawn in Section 6.5.

6.2. DATA COLLECTION AND PREPROCESSING

6.2.1. RADAR SETUP

The experiments are implemented in the campus of Delft University of Technology where there are many stationary parking cars, concrete buildings and moving bicycles. The MIMO radar (see in Fig. 6.1(a)) is set in the front of a car as shown

in Fig. 6.1(b). The radar with 3 transmitters and 4 receivers can be considered as a ULA with 3×4 elements. The car moved at speed of around 10 Km/h inside the campus. The raw data were collected by radar and the scenarios were captured by the driving recorder (Camera and GPS). The radar system settings are shown in

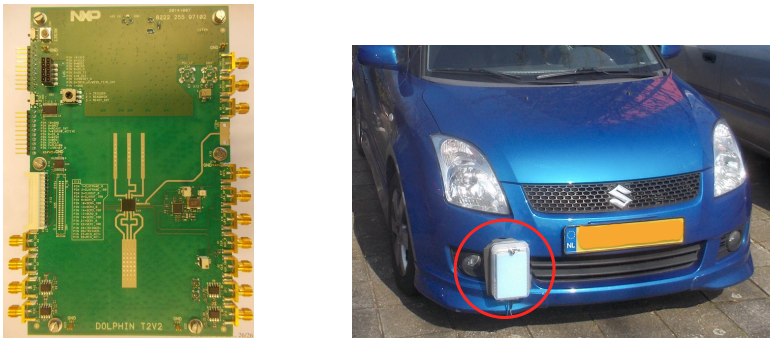

(a) (b)

Figure 6.1: Experiments setup: (a) NXP radar demonstrator RF board and (b) Experimental auto equiped with NXP radar demonstrator

Table 6.1. The transmitted FMCW signal model is shown in Fig 2.1. The MIMO

Table 6.1: System Parameters

Parameters	**Values**
Centre frequency	78.8 GHz
Bandwidth	1 GHz
Number of transmitters	3
Number of recievers	4
Number of chirps	32
Distance between elements	1.899 mm
Sampling frequency	20 MHz
Chirp duration	50 μs
Settle time	6 μs

transmitters transmit chirp signals sequentially and the reflected signals from the reflector are received by four receivers. After mixing with the transmitted signal, the beat frequency signal is generated and digitised by sampling at a low sampling rate. However, the raw data cannot be processed for imaging immediately, and some preprocessing operations should be implemented to filter out the interferences. The original measured data include many interferences due to the system settings. Moreover, the array pattern needs to be calibrated to suppress the mutual

coupling between array elements.

6.2.2. MIMO CALIBRATION

The MIMO calibration vector is collected by experimental trials. The steering vector directing to angle θ of MIMO virtual array is $\mathbf{a}(\theta) = \boldsymbol{\alpha}(\theta) \otimes \boldsymbol{\beta}(\theta)$, where $\boldsymbol{\alpha}(\theta)$ is the transmitted steering vector, $\boldsymbol{\beta}(\theta)$ is the received steering vector. In the following, the virtual array steering vector $\mathbf{a}(\theta)$ will be adopted. The reflected signal of a single target located at the 0° is collected as $\mathbf{a}_{\text{measured}}(0^\circ)$ in the laboratory. The ideal reflection of such target without mutual coupling is calculated as $\mathbf{a}_{\text{ideal}}(0^\circ)$. Then the calibration vector for this angle can be approximated by

$$\mathbf{c} = \mathbf{a}_{\text{ideal}}(0^\circ) \oslash \mathbf{a}_{\text{measured}}(0^\circ). \tag{6.1}$$

We note that a more accurate calibration matrix can be obtained by measuring multiple angles. Then the raw data can be calibrated by taking the element-wise product with $\mathbf{c}$ along the virtual array dimension. After all the preprocessing. the three-dimensional beat frequency data model $\boldsymbol{\mathcal{Y}} \in \mathbb{C}^{L \times M \times K}$ can be written as

$$\boldsymbol{\mathcal{Y}} = \sum_{i=1}^{I} \alpha_i \mathbf{a}(\theta_i) \circ \mathbf{f}_d(v_i) \circ \mathbf{f}_r(R_i) + \boldsymbol{\mathcal{N}}, \tag{6.2}$$

where $i = 1, 2, ..., I$ is the index of the far-field targets, α denotes the complex amplitude, L denotes the number of elements of the virtual array, M denotes the number of chirps, K denotes the number of fast-time samples after preprocessing, θ_i denotes the angle of the ith scatterer, $\boldsymbol{\mathcal{N}} \in \mathbb{C}^{L \times M \times K}$ denotes the additive system noise, and $\mathbf{a}(\theta_i) \in \mathbb{C}^{L \times 1}$, $\mathbf{f}_d(v_i) \in \mathbb{C}^{M \times 1}$, $\mathbf{f}_r(R_i) \in \mathbb{C}^{K \times 1}$, respectively, denote the virtual steering vector, Doppler beat frequency vector, range beat frequency vector of the ith scatterer. Here, according to the system parameters, the range migration phenomenon of slowly moving targets is nonobvious and could be neglected in the model.

6.3. IMAGING FOR ANGLE-RANGE

After removing the interferences and array calibration, the data are prepared for imaging. The wideband signal provides a sufficiently high range resolution with FFT. Thus, FFT is directly applied to the range domain. To accurately indicate the range profile, zero-padding is made for the FFT operation. After 1D FFT, the data model $\mathbf{Y}_{\tilde{k}} \in \mathbb{C}^{L \times M}$ of the $\tilde{k}$th range cell can be written as

$$\mathbf{Y}_{\tilde{k}} = \sum_{i=1}^{I} \alpha_i \text{sinc}[\beta(r_{\tilde{k}} - r_i)] \times \mathbf{a}(\theta_i) \mathbf{f}_d^T(v_i) + \mathbf{N}, \tag{6.3}$$

where β is a constant determined by the system parameters, $\tilde{k}$ is the index of the range profile after FFT, r_i is the range of ith scatterer and $\mathbf{N}$ is the noise matrix. As for the angle domain, 1D MUSIC is applied for each range cell by using the Doppler beat frequency dimension as the reference dimension.

6.3.1. SPATIAL SMOOTHING

Spatial smoothing has to be implemented before applying MUSIC algorithm in each range cell to separate the coherent signals. In fact, two closely spaced stationary targets have almost the same Doppler shift and are hardly separated by eigendecomposition. For a detailed explanation of spatial smoothing, the reader is referred to [99, 100].

6.3.2. TARGETS DETECTION IN EACH RANGE CELL

The eigendecomposition is performed then to the smoothed covariance matrix $\mathbf{C}_{\tilde{k}} \in \mathbb{C}^{(L-P)\times(L-P)}$ to obtain the eigen space as

$$\mathbf{C}_{\tilde{k}} = \mathbf{U}_{\tilde{k}} \mathbf{\Lambda}_{\tilde{k}} \mathbf{U}_{\tilde{k}}^{H}, \tag{6.4}$$

where P is the constant for dimension reduction in spatial smoothing, $\mathbf{U}_{\tilde{k}}$ is a unitary matrix. The eigenvalues can be found from the diagonal matrix $\mathbf{\Lambda}$. The eigenvalue vector is

$$\boldsymbol{\lambda}_{\tilde{k}} = [\lambda_{\tilde{k},1}, \lambda_{\tilde{k},2}, ..., \lambda_{\tilde{k},L-P}] = \text{diag}(\mathbf{\Lambda}_{\tilde{k}}). \tag{6.5}$$

The number of the targets can be estimated from this vector. If there is no target, the absolute values of the eigenvalues decrease very smoothly, while if there are some targets present, the absolute value of the eigenvalues corresponding to the targets will be much larger than that corresponding to the noise. Although there are many criteria in literature for the number of targets estimation, in this section a threshold which is determined by the average value of the eigenvalues is used in each range cell for simplicity.

6.3.3. MUSIC ALGORITHM FOR AZIMUTH-RANGE IMAGING

Then according to the number of detected targets, the noise subspace can be extracted from the eigendecomposition as

$$\mathbf{U}_{\tilde{k}} = [\mathbf{W}_{\tilde{k}} \ \mathbf{V}_{\tilde{k}}], \tag{6.6}$$

where $\mathbf{W}_{\tilde{k}}$ and $\mathbf{V}_{\tilde{k}}$ represent the signal subspace and noise subspace, respectively. Divide the angle domain into Q grids as $[\theta_0, \theta_1, ..., \theta_Q]$ and formulate the steering vector $\mathbf{a}(\theta) \in \mathbb{C}^{(L-I)\times 1}$ as

$$\mathbf{a}(\theta) = [1, e^{j2\pi \frac{d}{\lambda} \sin\theta}, ..., e^{j2\pi \frac{(L-P)d}{\lambda} \sin\theta}]^T, \tag{6.7}$$

where d is the inter space between neighbouring virtual elements and λ is the wavelength of the center frequency. Applying MUSIC algorithm, the pseudo-spectrum of angle $\mathbf{p}_{\tilde{k}} \in \mathbb{R}^{Q\times 1}$ can be obtained

$$\mathbf{p}_{\tilde{k}} = [\frac{1}{||\mathbf{a}(\theta_0)\mathbf{V}_{\tilde{k}}||^2}, ..., \frac{1}{||\mathbf{a}(\theta_Q)\mathbf{V}_{\tilde{k}}||^2}]^T. \tag{6.8}$$

The MUSIC spectrum is the pseudo-spectrum, which means the amplitudes of MUSIC results cannot directly represent the amplitudes of the scatterers.

To approximate the real spectrum of the range-angle map, the pseudo-spectrum needs some transformation. Here, we propose a novel normalisation method by using the spectral norm of $\mathbf{Y}_{\tilde{k}}$ to approximately represent the maximum energy of the range cell $\tilde{k}$. Therefore, after normalisation of the pseudo-spectrum to the same baseline as $0 \sim 1$ for all range cells, the spectral norm of $\mathbf{Y}_{\tilde{k}}$ is calculated as the maximum spectrum of range cell $\tilde{k}$. Now, the spectrum for different range cells are comparable and the formula is

$$\hat{\tilde{\mathbf{p}}}_{\tilde{k}} = ||\mathbf{Y}_{\tilde{k}}||_2 \frac{\hat{\mathbf{p}}_{\tilde{k}} - ||\hat{\mathbf{p}}_{\tilde{k}}||_{\min}}{||\hat{\mathbf{p}}_{\tilde{k}}||_{\max} - ||\hat{\mathbf{p}}_{\tilde{k}}||_{\min}} \tag{6.9}$$

6.4. PROCESSING RESULTS

In this section, we will present some results of the measured data by the proposed methods. The car was moving with a speed of about 10 Km/h for the whole experiment.

The first scenario for the measured data is shown in Fig. 6.2(a), where the strong reflectors contain the building wall with metal reinforcement (indicated by the purple dashed line), a pedestrian close to the wall (indicated by the green circle), a metal sewer cover (indicated by the green circle) some stationary cars (indicated by the red circle). The imaging result of the proposed method for such a scenario is shown in Fig. 6.2(c), and for comparison, the processing results using conventional BF method is shown in Fig. 6.2(b). By comparison, the spectra of the wall metal reinforcement and the car are narrower for super-resolution algorithm than that of BF method. Moreover, the pedestrian and sewer cover are masked by the sidelobes of the spectra of the wall in Fig. 6.2(b), while in Fig. 6.2(c) the pedestrian and the sewer cover can be clearly separated from the wall (indicated by the white arrows).

The second scenario is shown in Fig. 6.3(a), where the strong reflectors are the bicycles along the road (indicated by the purple dashed line), a cyclist (indicated by the green circle) and a lamppost (indicated by the cyan square) in front of the car. The processing results using both the MUSIC algorithm and the BF method are shown in Fig. 6.3(c) and Fig. 6.3(b), respectively. The figures also show that the spectrum for both bicycles and lamppost are overall narrower and more clear of

MUSIC algorithm than that of BF method. The sidelobes for BF method (indicated with red arrows) are as strong as the spectrum of the cyclist (indicated with the white arrow), which makes it difficult to identify the cyclist.

From the figures and analysis above, the performance of the angular resolution of the MUSIC algorithm is overall much better than that of the BF method. The time consumption of two methods for the same data and with the same computer is 0.44 second for the FFT-MUSIC method and 0.09 second for FFT-BF method. Although it is slightly slower in this case, the proposed FFT-MUSIC algorithm has much room for efficient implementation by using parallel processing in the real application.

6.5. CONCLUSIONS

In this chapter, we have presented the MIMO automotive radar angle-range imaging using FFT-MUSIC and the results with experimental data. The data collected from moving cars are preprocessed and calibrated at first. Then the FFT-MUSIC algorithm is applied for the angle-range imaging. The range profile is processed by FFT for efficiency and MUSIC algorithm is applied for angle profile for high-resolution separation. The experimental results obtained with MUSIC and BF method are presented and compared. Although the time consumption is slightly increased, it is clear that the MUSIC algorithm provides much higher angular resolution without strong sidelobes.

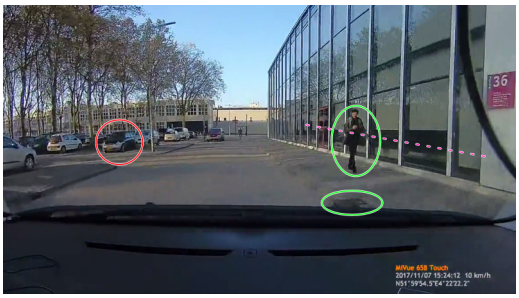

(a)

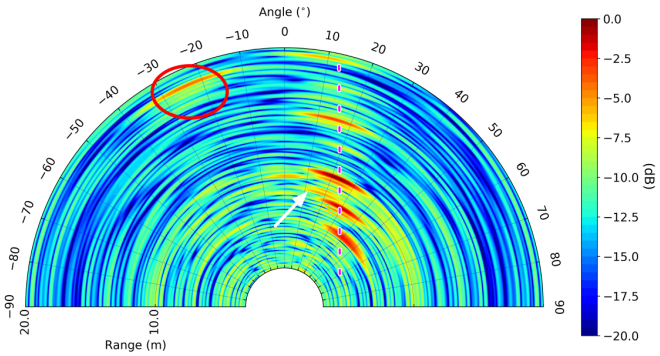

(b)

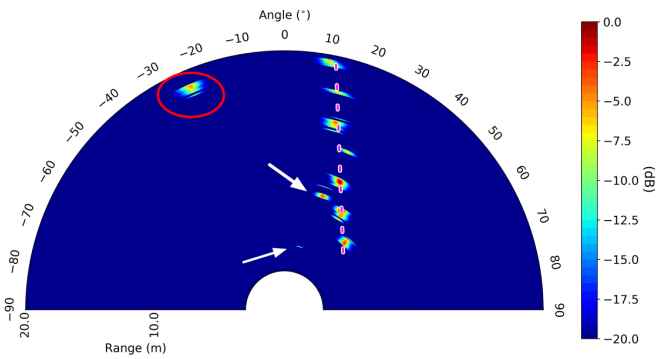

(c)

Figure 6.2: Scenario 1: (a) the scenario captured by camera; (b) the results of FFT-BF method; (c) the results of FFT-MUSIC method

(a)

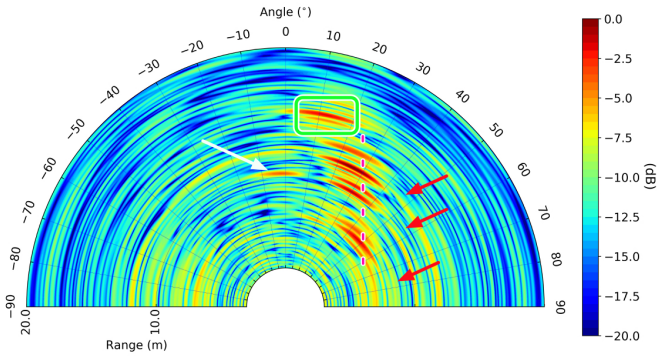

(b)

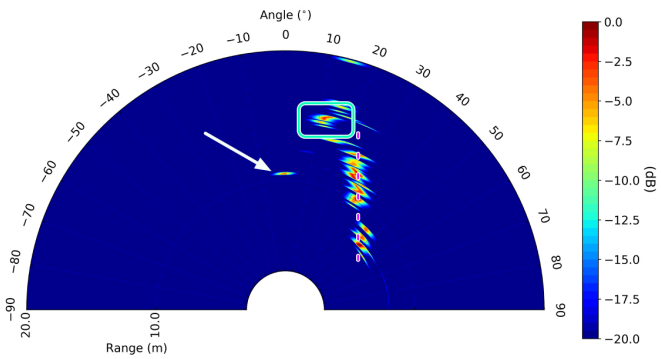

(c)

Figure 6.3: Scenario 2: (a) the scenario captured by camera; (b) the results of FFT-BF method; (c) the results of FFT-MUSIC method

7

CONCLUSIONS

7.1. CONCLUSIONS

The work described in this dissertation addresses the major problems and challenges of joint parameters estimation, namely the ranges, radial velocities, and azimuths, for multiple moving objects using (ultra-)wideband signals. Target movement results in target migration over the range cells during the CPI. Algorithms were developed which compensate target movements or even use it to improve target parameter estimation has been performed in this thesis for several major MIMO radar problems.

For the FMCW signal, which is the main waveform used in this thesis, the established signal model takes both the wideband DOA and range migration problems into account. It differs from the narrowband case by two extra mutual coupling terms in the signal model. One is introduced by the wideband DOA as coupling component between element indices and slow-time indices. Another one presented as mutual coupling component between fast-time samples and slow-time indices which is caused by range migration. Conventional multi-dimensional frequency estimators can only be applied to the estimation of the parameters when each point-like source is present as a rank-one component (Fourier basis or another Hilbert basis). However, in the established signal model of moving targets, the spectrum spreads due to the mutual couplings introduced by the wideband signals and it cannot be represented as a mixture of multiple uncorrelated rank-one components. In this thesis, several algorithms have been proposed to address the joint multiple parameters estimation (such as range, Doppler and azimuth) in the presence of such couplings.

As a side study, bi-phase phase-modulated CW (PMCW) radar, which is low Doppler tolerance compared to FMCW, is also investigated separately in the ap-

pendix. The Doppler frequency shift degrades orthogonality between the transmitted binary codes and the reflected binary codes from the moving target. This degradation introduces the energy loss of the main lobe and strong sidelobes. The main lobe and sidelobes levels of PMCW in the presence of Doppler shift and low-pass filter are analysed. The Doppler correction technique is presented and validated with experimental data. However, the study of PMCW is preliminary and there are opportunities for deeper investigation which would be discussed in 7.2

The major novelties and achievements are summarised as follow.

- *A Novel Compensated MUSIC algorithm:* For the established UWB FMCW model, the conventional 2D MUSIC algorithm is applied to the joint estimation of DOA and Doppler. To eliminate the influences of the coupling terms, an original compensation method is proposed. The compensation algorithm precisely adjusts the phase for each scanning grid and the dynamic noise subspace is used to formulate the MUSIC algorithm. To alleviate the computational load of the multiple eigendecompositions of large matrices, two efficient implementations are introduced, i.e., Lanczos algorithm and Rayleigh-Ritz step.

  By comparing RMSEs and CRB of classical MUSIC, Keystone MUSIC and proposed algorithm (for the bandwidths of 1 GHz and 4 GHz) via numerical simulations, it is demonstrated that the phase compensation algorithm improves the accuracies of both Doppler and DOA estimation over the classical and Keystone MUSIC and the accuracies of the proposed algorithm improve with SNR. For example, the accuracies of both Doppler and DOA estimations are improved more than 20 dB for SNR = 20 dB as shown in Fig. 3.7. Although for SNR below -10 dB Keystone MUSIC has an accuracy similar to the proposed method, the resolution and overall contrast of the MUSIC pseudo-spectrum is worse than by the algorithm proposed. Due to the phase compensation, the algorithm proposed also resolves targets closely spaced in the velocity-angular domain, which are not resolvable both with a classical and Keystone MUSIC algorithms as shown in Fig. 3.10. Further, it is demonstrated that the proposed Lanczos algorithm and Rayleigh-Ritz are more robust than the inverse algorithm in the simulations in Fig. 3.11. In addition, the Rayleigh-Ritz step shows superiority with respect to computation time consumption when the number of targets is much smaller than the dimension of the signal covariance matrix (see Fig 3.2) and has a high tolerance for overestimating the dimension of the signal subspace (see Fig. 3.13).

  It is demonstrated that the phase adjustment approach is further applicable to 3D MUSIC algorithm for 3D parameters estimation (see Fig. 3.14)

- *Novel spectral norm-based algorithm:* The proposed compensated MUSIC greatly increases the accuracy of parameter estimations. However, it fails to provide an efficient way to resolve the Doppler ambiguity for fast-moving targets. The state-of-art algorithms to address the ambiguous Doppler are based on coherent integration, which suffers from the off-grid problems for Doppler fold number estimation when the data size is limited. Therefore, a novel algorithm is then proposed to address the joint estimation of ranges, ambiguously radial velocities and azimuths for multiple point-like targets. The kernel of the algorithm combines several parts: a spectral norm-based parameters extraction from the coupling components and an alternative parameter refinement method are introduced for a single target, then the Greedy algorithm for initialization and RELAX algorithm for optimization of the results are applied for multiple targets. An efficient implementation of the proposed algorithm is further introduced using the power iteration algorithm. The performance of the algorithm proposed is validated by numerical simulations.

  According to the results of the simulation, the algorithm proposed avoids the off-grid problem and is more than 16 times faster than FFT based algorithm (with 3 times zero-padding) for Greedy algorithm and around 7 times faster for RELAX iteration. On top of that, the RMSEs results also suggest that signals with wider bandwidth should be used to resolve the Doppler ambiguity at lower SNR conditions (see Fig. 4.6(b), the RMSE of 1 GHz signal reaches the CRB around 5 dB while that of 4 GHz signal arrives at the CRB at -2.5 dB). It is also proved that the algorithm proposed holds the super-resolution ability of the RELAX at the expense of the slight loss of the accuracy and larger number of iterations (see in Fig. 4.7).

- *Entropy of eigenspectrum for auto-focusing of clusters of point-like targets:* Both above-mentioned algorithms, compensated MUSIC and spectral-norm based algorithm, are based on the assumptions of sparsely point-like targets. However, the distributed targets are usually presented as clusters of point sources. It is a waste of time to extract the point targets in the same cluster one by one using the RELAX algorithm. Since each cluster of point targets has similar range migration couplings and Doppler ambiguities, the range alignment could be performed for all point targets in one cluster at the same time using some auto-focusing techniques.

  For point targets, the focusing criterion is easily chosen for the maximum coherent integration energy. While for a cluster of point targets, the Shannon entropy of the range-Doppler map is widely applied to the focusing judgement. However, the Shannon entropy of the range-Doppler spectrum also

suffers the off-grid problem and sidelobes interference. Inspiring from the proposed spectral-norm based algorithm, a criterion based on the entropy of the eigenspectrum was proposed. To combine the advantages of the entropies of both spectra, a simple combination method is presented.

The simulation shows that two cars with the same accelerations and slightly different velocities cannot be resolved in the conventional entropy of the Fourier spectrum while they are clearly separated in the entropy of the eigenspectrum. With the combined entropy map, the motion parameters are estimated and subsequently, the range-Doppler map is reconstructed.

- *FFT-MUSIC algorithm for automotive radar imaging:*

  The previous chapters address the fast-moving objects, while we also proposed the fast imaging algorithm for a slow-moving scenario which combines fast Fourier transform and MUSIC algorithm. However, since the MUSIC algorithm generates a so-called pseudo-spectrum and cannot be comparable for different range cells, a new normalisation technique is proposed by us based on the spectral norm of the covariance matrix of different range cells. By comparing the processing results by the proposed FFT-MUSIC and the conventional FFT-BF algorithm, the proposed algorithm provides much cleaner image without strong sidelobes and with higher azimuthal resolution than conventional FFT-BF method at the expense of slightly higher computational load.

- *Study on Doppler influence for bi-phase PMCW waveform:*

  The behaviour of PMCW for moving objects is quite different from FMCW and we provide the investigations on bi-phase PMCW in the presence of Doppler shift and low-pass filter as a side study in the appendix. The main lobe and sidelobe levels are analysed in the presence of Doppler shift and a Doppler correction technique is presented which preserves the correlation patterns of the codes. Then the experimental data are collected with PARSAX and processed with the Doppler compensation. Compared to the conventional range-Doppler process for PMCW, the main lobe level is enhanced in line with the analytical results and the sidelobe levels are suppressed almost to the noise level with the proposed Doppler compensation technique.

7.2. RECOMMENDATIONS FOR FUTURE WORK

- Efficient implementation of tensor decomposition

  Tensor decomposition is a powerful tool and is intensively studied in the academic area. Despite that the tool is time-consuming, it provides an alternative

tool in higher-dimensional data processing analogous to the principal component analysis by SVD.

- Joint parameters estimation in the presence of non-Gaussian noise

  All the algorithms presented in this thesis are based on the assumption of Gaussian noise. It is recommended to test the performance of the algorithms for joint parameters estimation in the presence of non-Gaussian noises and strong clutters.

- Near-field scenarios and angular velocity estimation

  The far-field scenario is considered in the thesis, while when the target is sufficiently close to phased array radar or using array/MIMO with a much larger aperture, the near-field problem should be addressed. Moreover, when the targets are close, the fast-moving targets may migrate both in range cells and angular cells, and such angular velocity would provide additional components in the signal model. Therefore, some advanced algorithm should be introduced to address such problems.

- Perturbation of eigenspectrum

  Although the current divide-and-conquer algorithm can compute eigenspectrum of large matrix efficiently by using parallel processing, the time consumptions of computing eigenspectrum are much heavier than that of computing Fourier spectrum. Fortunately, the perturbation theory of the matrix eigenspectrum is a hot topic in mathematics. The specific perturbation pattern is clear in the proposed algorithms. There might exist a favourable algorithm for efficient implementation of eigenspectrum computation.

- Range migration problem of the PMCW signals

  The interference of the Doppler shift on the code has been studied in this thesis. However, the range migration problem may also happen to the PMCW signals, which would cause the code mismatch problem. This problem would also directly decrease the range resolution. What worse is that most of the current DOA algorithm would be invalid. Further, the Doppler ambiguity presented in the PMCW signals differently and the proposed spectral norm would fail to estimate the ambiguity fold number. Such study will bring the PMCW a wider application.

A

CRB DERIVATION

To formulate CRB matrix, we first reshape the raw data (2.16) into the vector form $\mathbf{y} \in \mathbb{C}^{LMK\times 1}$ as

$$\mathbf{y} = \sum_{i=1}^{I} \alpha_i(\mathbf{a}(\theta_i) \otimes \mathbf{f}_d(v_i) \otimes \mathbf{f}_r(r_i)) \odot \boldsymbol{\omega}_{dr}(v_i) \odot \boldsymbol{\omega}_{\theta r}(\theta_i) + \mathbf{n}, \tag{A.1}$$

where all the Doppler velocities are considered as ambiguous, $\boldsymbol{\omega}_{dr}(v_i) \in \mathbb{C}^{LMK\times 1}$ and $\boldsymbol{\omega}_{\theta r}(\theta_i) \in \mathbb{C}^{LMK\times 1}$ are

$$\boldsymbol{\omega}_{dr}(v_i) = \mathbf{1}_L \otimes \begin{pmatrix} \mathbf{g}_0(v_i) \\ \mathbf{g}_1(v_i) \\ \vdots \\ \mathbf{g}_{M-1}(v_i) \end{pmatrix}; \boldsymbol{\omega}_{\theta r}(\theta_i) = \begin{pmatrix} \mathbf{1}_M \otimes \mathbf{h}_0(\theta_i) \\ \mathbf{1}_M \otimes \mathbf{h}_1(\theta_i) \\ \vdots \\ \mathbf{1}_M \otimes \mathbf{h}_{L-1}(\theta_i) \end{pmatrix} \tag{A.2}$$

Let $\mathbf{Q} \in \mathbb{C}^{LMK\times 1}$ be the noise covariance matrix, which is

$$\mathbf{Q} = E(\mathbf{n}\mathbf{n}^H) = \sigma^2 \mathbf{I}_{MLK} \tag{A.3}$$

with σ^2 being the variances of the noise. According to the extended Slepian-Bangs' formula [101], the ijth element of the fisher information matrix (FIM) has the form:

$$\{\text{FIM}\}_{ij} = \text{Tr}\left(\mathbf{Q}^{-1}\frac{\partial \mathbf{Q}}{\partial \boldsymbol{\eta}_i}\mathbf{Q}^{-1}\frac{\partial \mathbf{Q}}{\partial \boldsymbol{\eta}_j}\right) + 2\Re\left[\left(\frac{\partial \mathbf{y}}{\partial \boldsymbol{\eta}_i}\right)^H \mathbf{Q}^{-1}\left(\frac{\partial \mathbf{y}}{\partial \boldsymbol{\eta}_j}\right)\right] \tag{A.4}$$

where

$$\boldsymbol{\eta} = [\boldsymbol{\theta}, \mathbf{v}, \mathbf{r}, \Re(\boldsymbol{\alpha}), \Im(\boldsymbol{\alpha})]^T \tag{A.5}$$

A

with $\boldsymbol{\theta}$ and $\mathbf{v}$ being the vectors consisting of the DOAs and Doppler frequencies, respectively. $\partial \mathbf{y}/\partial \boldsymbol{\eta}_i$ denotes the derivative of $\mathbf{y}$ with respect to the ith parameter of $\boldsymbol{\eta}$. Note that the FIM is block diagonal since the parameters in $\mathbf{Q}$ are independent of those in $\boldsymbol{\eta}$ and vice versa. Thus, the CRB matrix for the motion parameters can be calculated from the second term on the right side of (A.4). The derivations of each parameters are given as follow, where for simplicity the parameters denotions are neglected.

$$\begin{aligned}
\boldsymbol{\chi}_i^{\theta} &= j\xi_{1,i}(\mathbf{d}_L \odot \mathbf{a}) \otimes \mathbf{f}_d \otimes \mathbf{f}_r \odot \boldsymbol{\omega}_{dr} \odot \boldsymbol{\omega}_{\theta r} \\
&\quad + j\xi_{2,i}\mathbf{a} \otimes \mathbf{f}_d \otimes \mathbf{f}_r \odot \boldsymbol{\omega}_{dr} \odot [\boldsymbol{\omega}_{\theta r} \odot (\mathbf{d}_L \otimes \mathbf{1}_M \otimes \mathbf{d}_K)] \\
\boldsymbol{\chi}_i^{\mathbf{v}} &= j\zeta_{1,i}\mathbf{a} \otimes (\mathbf{d}_M \odot \mathbf{f}_d) \otimes \mathbf{f}_r \odot \boldsymbol{\omega}_{dr} \odot \boldsymbol{\omega}_{\theta r} \\
&\quad + j\zeta_{2,i}\mathbf{a} \otimes \mathbf{f}_d \otimes \mathbf{f}_r \odot [(\mathbf{1}_L \otimes \mathbf{d}_M \otimes \mathbf{d}_K) \odot \boldsymbol{\omega}_{dr}] \odot \boldsymbol{\omega}_{\theta r}, \\
\boldsymbol{\chi}_i^{\mathbf{r}} &= j\nu\mathbf{a} \otimes \mathbf{f}_d \otimes (\mathbf{d}_K \odot \mathbf{f}_r) \odot \boldsymbol{\omega}_{dr} \odot \boldsymbol{\omega}_{\theta r}, \\
\boldsymbol{\alpha}_i^{\mathbf{R}} &= \mathbf{a} \otimes \mathbf{f}_d \otimes \mathbf{f}_r \odot \boldsymbol{\omega}_{dr} \odot \boldsymbol{\omega}_{\theta r}, \\
\boldsymbol{\alpha}_i^{\mathbf{I}} &= j\mathbf{a} \otimes \mathbf{f}_d \otimes \mathbf{f}_r \odot \boldsymbol{\omega}_{dr} \odot \boldsymbol{\omega}_{\theta r},
\end{aligned} \tag{A.6}$$

where the coefficients are $\xi_{1,i} = 2\pi\alpha_i f_c \dfrac{d}{c}\cos\theta_i$, $\xi_{2,i} = 2\pi\alpha_i\mu\dfrac{d}{cf_s}\cos\theta_i$, $\zeta_{1,i} = -4\pi\alpha_i T\dfrac{f_c}{c}$, $\zeta_{2,i} = -4\pi\alpha_i T\dfrac{\mu}{cf_s}$, $\nu = 4\pi\dfrac{\mu}{cf_s}$.
For joint all parameters estimation in chapter 4, let

$$\mathbf{G} = [\boldsymbol{\chi}_1^{\theta} \ldots \boldsymbol{\chi}_I^{\theta}, \boldsymbol{\chi}_1^{\mathbf{v}} \ldots \boldsymbol{\chi}_I^{\mathbf{v}}, \boldsymbol{\chi}_1^{\mathbf{r}}, \ldots \boldsymbol{\chi}_I^{\mathbf{r}}, \boldsymbol{\alpha}_1^{\mathbf{R}} \ldots \boldsymbol{\alpha}_I^{\mathbf{R}}, \boldsymbol{\alpha}_1^{\mathbf{I}} \ldots \boldsymbol{\alpha}_I^{\mathbf{I}}]. \tag{A.7}$$

while for just joint DOA and Doppler in chapter 3, then let

$$\mathbf{G} = [\boldsymbol{\chi}_1^{\theta} \ldots \boldsymbol{\chi}_I^{\theta}, \boldsymbol{\chi}_1^{\mathbf{v}} \ldots \boldsymbol{\chi}_I^{\mathbf{v}}]. \tag{A.8}$$

Then the CRB matrix for the parameter vector $\boldsymbol{\eta}$ is given by

$$CRB(\boldsymbol{\eta}) = [2\Re(\mathbf{G}^H\mathbf{Q}^{-1}\mathbf{G})]^{-1}. \tag{A.9}$$

There are two terms in $\boldsymbol{\chi}_i^{\mathbf{v}}$ (A.6), where the first term is the derivation of folded velocity from the sinusoids and the second term is the derivation of unambiguous velocity from the coupling terms. Therefore, the corresponding CRBs can be calculated separately. Let $\hat{\boldsymbol{\chi}}_i^{\mathbf{v}} = j\zeta_{1,i}\mathbf{a} \otimes (\mathbf{d}_M \odot \mathbf{f}_d) \otimes \mathbf{f}_r \odot \boldsymbol{\omega}_{dr} \odot \boldsymbol{\omega}_{\theta r}$ and $\check{\boldsymbol{\chi}}_i^{\mathbf{v}} = j\zeta_{2,i}\mathbf{a} \otimes \mathbf{f}_d \otimes \mathbf{f}_r \odot [(\mathbf{1}_L \otimes \mathbf{d}_M \otimes \mathbf{d}_K) \odot \boldsymbol{\omega}_{dr}] \odot \boldsymbol{\omega}_{\theta r}$. Then set $\mathbf{G} = [\hat{\boldsymbol{\chi}}_1^{\mathbf{v}}, ..., \hat{\boldsymbol{\chi}}_I^{\mathbf{v}}]$ or $\mathbf{G} = [\check{\boldsymbol{\chi}}_1^{\mathbf{v}}, ..., \check{\boldsymbol{\chi}}_I^{\mathbf{v}}]$, the corresponding CRBs can be calculated according to (A.9) for $\hat{\mathbf{v}}$ or $\check{\mathbf{v}}$.

Using the same system setting from Section 4.5.3, and set one target as $\alpha = 1$, $v = 50$m/s, $r = 30$m and $\theta = 30°$, the corresponding CRBs for $\hat{v}$ and $\check{v}$ are plotted in Fig. A.1.

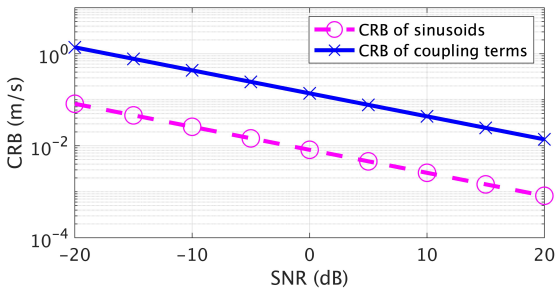

Figure A.1: CRB comparison of folded velocity from sinusoids and the unambiguous velocity from the coupling terms

B

Study on Doppler Influence for bi-phase PMCW Signals

The bi-phase PMCW waveform properties for moving targets sensing are studied in this appendix. The accurate signal model using PMCW waveform observing multiple moving objects is established. The main lobe and sidelobe level of the code autocorrelation are analysed in the presence of Doppler shifts and low-pass filter. Then a compensation algorithm to mitigate the influence of the Doppler shift on the orthogonality of the codes is presented. Furthermore, an experiment with PARSAX radar is performed by observing multiple moving vehicles on the street and the corresponding range-Doppler results using the conventional algorithm and the compensation algorithm are compared. The processing results demonstrate that the main lobe level decreases as expected due to the Doppler shift and the compensation method can recover the correct level of the main lobe and suppress the sidelobe level simultaneously.

B.1. INTRODUCTION

Automotive radar plays an important role in driver assisting systems aiming to both on road safety and driver comfort improvement and many modern vehicles are already equipped with different systems. To increase the azimuthal angular resolution and simultaneously restrict the aperture size and the cost, the MIMO technique is widely applied in the current generation of the automotive radars [102]. To achieve simultaneous transmission from all transmit channels and reduce the mutual interference between multiple channels in MIMO, the orthogonality of the transmitted waveforms has to be achieved. In FMCW MIMO systems, time-division multiple access (TDMA) or frequency-division multiple access (FDMA) has to be applied to realize simultaneous transmission and avoid cross-correlation among the transmitted waveforms [103]. An alternative to FMCW, called phase-modulated continuous-wave (PMCW), has attracted more considerations in automotive application due to its performance and implementation simplicity [104].

PMCW waveform, however, is also suffering from relatively high-level sidelobes in the range profile, and different dedicated approaches have been suggested to reduce them [105–119]. The first kind of sidelobe is introduced by imperfect correlation properties of the code itself. Although this is inevitable when designing the waveform, many kinds of code families are proposed and provide different sidelobe pattern [105–110, 114]. Welch bound provides a lower bound for sidelobe level and usually is used as a criterion to evaluate the performance in codes design [111].

Phase coding of the CW signal spreads the power of the signal over a large bandwidth. To fit the PMCW signal spectrum to the spectral usage regulations and limit the bandwidth requirements to the ADC, PMCW waveform undergoes low-pass filtering. This filtering leads to another kind of sidelobe or increases the level of the first kind of sidelobe.

Doppler frequency shift, which is caused by target movement, results in the code orthogonality loss in the reflected signal and introduces the last kind of sidelobe. Many techniques have been proposed to suppress such sidelobes. For the single pulse PMCW waveform, 2D matched filter with multiple Doppler compensation can be applied and the thresholding method is used to estimate the Doppler frequency [112, 113]. In addition to the bi-phase PMCW waveform, poly-phase coded waveform has higher Doppler tolerance where such sidelobes are almost negligible [114, 115]. However, digital integrated circuit (IC) implementations with respect to these poly-phase codes require very high-performance DACs and ADCs and will probably be more affected by IQ imbalance and other circuitry impacts. Moreover, the mismatched filter provides lower sidelobe level than the matched filter in the presence of Doppler shift at the expense of decreased SNR [116, 117]. For multi-pulses PMCW, Doppler correction can be performed on each Doppler channel [118, 119]. This can be performed by applying the matched filter to each

Doppler channel with the replica of the desired signal, which is the subpulse with corresponding Doppler offset. An alternative way for Doppler correction is bit-inversion by applying 1-bit sampling and reverse the bit value when the phase changed more than 180 degrees [118].

In this appendix, the main lobe level of the PMCW waveform autocorrelation function is studied in the presence of the Doppler shift and the low-pass filter. According to the signal model established, the main lobe level will decrease with the increase of the velocity within the unambiguous velocity domain. We show that the maximum decrease of main lobe level due to the Doppler shift is 1.961 dB when the velocity approaches the maximum unambiguous velocity regardless of the code family, bandwidth or carrier frequency. Furthermore, a compensation algorithm is presented to recover the orthogonality of the codes and mitigate the influence of the Doppler shift on the main lobe and sidelobe level. To validate the influence of the Doppler shift on PMCW waveform by observing moving targets, an experimental study has been performed PARSAX radar. The range-Doppler maps are obtained with the conventional algorithm and the proposed compensation method.

The rest of the appendix is organised as follows. The signal model of the PMCW waveform is established in Section B.2. Based on the signal model, the properties of the autocorrelation of the codes on main-lobe and sidelobes are analysed in Section B.3. Then the Doppler shifts compensation method is introduced in Section B.4. Furthermore, the experimental study is described and the results are provided in Section B.5. The conclusions are drawn in Section B.6.

B.2. PMCW SIGNAL MODEL

The bi-phase PMCW radars use sequences of binary symbols or chips that are mapped onto 0 and 180 degree phase shifts of a continuous radiofrequency carrier [104]. Assuming availablility of P mutual orthogonal code series, the chip series can be presented as

$$\phi_k^p = \{-1, 1, -1, ..., -1, 1, -1\}, \tag{B.1}$$

where $p = 0, 1, ..., P-1$ indicates the index of the code series, $k = 0, 1, ..., K-1$ is the binary chip indices and K is the code length. According to the properties of PMCW, it is assumed that the code set hold (here we assume the $i, j < K$)

$$\text{corr}[\phi_{k-i}^p,\ \phi_{k-j}^q] = \begin{cases} 0 & \text{if } p \neq q \text{ or } \quad i \neq j, \\ K\delta(k-i) & \text{if } p = q \text{ and } i = j. \end{cases} \tag{B.2}$$

where corr denotes the correlation operation, ϕ_{k-i}^p and ϕ_{k-j}^p are the circular shifted code of ϕ_k with i and j chips and $\delta(\cdot)$ is the Kronecker delta function. With the

code, the normalised phase modulated signal of one pulse with pth code can be formed as

$$s^p(t) = \sum_{k=0}^{K-1} \phi_k^p \,\text{rect}\left(\frac{t - kT_c}{T_c}\right) \quad t \in [0, T), \tag{B.3}$$

where T_c is the binary chip duration, $T = KT_c$ is the pulse duration and

$$\text{rect}(x) = \begin{cases} 1 & |x| \leq 0.5, \\ 0 & |x| > 0.5. \end{cases} \tag{B.4}$$

The chip series can be easily recovered from Eq. (B.3) by sampling with interval T_c. Multiple pulses with all code series are

$$S(t) = \sum_{p=0}^{P-1} \sum_{m=0}^{M-1} s^p(t - mT) \quad t \in [0, MT), \tag{B.5}$$

where $m = 0, 1, ..., M-1$ denotes the index of the pulses, M denotes the total number of pulses. Mixed with the carrier wave, the transmitted signals for the transmitters are given as

$$S_T(t) = S(t)e^{j2\pi f_c t}, \tag{B.6}$$

where f_c is the carrier frequency.

Let assume I moving targets are presented in the observation domain. Then the round trip delay of ith target is

$$\tau_i(t) = \frac{2(R_i + v_i t)}{c} = \gamma_i + \frac{2v_i}{c}t, \tag{B.7}$$

where R_i, $\gamma_i = \dfrac{2R_i}{c}$ and v_i denote, respectively, the initial range, initial round trip delay and the radial velocity of ith target, and c denotes the speed of the light.

Here, we assume the radial velocities of all targets are within the maximum unambiguous velocity of the system. Moreover, another important assumption is that the targets will not migrate more than one range resolution cell $\delta_r = \dfrac{cT_c}{2}$. The received signal of qth receiver is

$$\begin{aligned} S_R(t) &= \sum_{i=1}^{I} \alpha_i S_T[t - \tau_i(t)] \\ &= \sum_{i=1}^{I} \alpha_i e^{j2\pi f_c(t - \gamma_i - \frac{2v_i}{c}t)} S\left(t - \gamma_i - \frac{2v_i}{c}t\right) \\ &\approx \sum_{i=1}^{I} \alpha_i e^{j2\pi f_c t} e^{-j2\pi f_c \gamma_i} e^{-j2\pi \frac{2v_i}{c} f_c t} S(t - \gamma_i), \end{aligned} \tag{B.8}$$

where α_i denotes the complex amplitude of the ith target. Here we assume $v_i \ll c$ and t is short, then the term $\frac{2v_i}{c}$ in $S\left(t-\gamma_i-\frac{2v_i}{c}t\right)$ is omitted. To keep the formulas simple, we neglected the noise term since the additive noise is independent of our method. Noting that when the velocities are so large that the targets would move several range cells within $T_{frame}=MT$, this term then cannot be neglected directly and the code mismatch problem has to be considered. This case will be studied in the future.

Let $f_{d,i}=\frac{2v_i}{c}f_c$ denotes the Doppler frequency of ith target and the constant term $e^{-j2\pi f_c\gamma_i}$ is absorbed into α_i (for simplicity, α_i is still used in the following). Then the received signal is mixed with conjugate of the carrier wave and we obtain

$$\hat{S}_R(t)=\sum_{i=1}^{I}\alpha_i e^{-j2\pi f_d(v_i)t}S(t-\gamma_i). \tag{B.9}$$

To jointly estimate the range and the Doppler information, the time t is split into fast-time t' and slow-time index m with time interval T as

$$t=t'+mT \qquad t'\in[0,T). \tag{B.10}$$

The received data are sampled with the sampling interval T_c in the fast-time domain and the discrete data are obtained as

$$\begin{aligned}X(k,m)&=\sum_{i=1}^{I}\Big\{\alpha_i\exp(-j2\pi f_d(v_i)(kT_c+mT))\\&\qquad\times S(kT_c+mT-\gamma_i)\Big\}\\&=\sum_{i=1}^{I}\Big\{\alpha_i\exp(-j2\pi f_d(v_i)kT_c)\\&\qquad\times\exp(-j2\pi f_d(v_i)mT)\times\sum_{p=0}^{P-1}\phi_{k-n_i}^{p}\Big\},\end{aligned} \tag{B.11}$$

where $k=0,1,...,K-1$ and K, respectively, denote the fast-time indices $k=\left\lfloor\frac{t}{T_c}\right\rfloor$ and the total samples in each pulse, and $n_i=\left\lfloor\frac{\gamma_i}{T_c}\right\rfloor$ denotes the number of the code shift of ith target where $\lfloor x\rfloor$ gives the nearest integer less than or equal to x. In FMCW radar, the term $\exp(-j2\pi f_d(v_i)kT_c)$ is omitted because of Doppler tolerance of LFM waveform. However, in the PMCW signal model, the term will add a redundant phase shift on the binary code, which decreases the orthogonality and brings high-level sidelobes in range profile. Without any phase adjustment,

the performance of the range profile by correlation operation will be dramatically degraded, especially with a high Doppler frequency shift.

B

B.3. MAIN LOBE AND SIDELOBES LEVEL ANALYSIS

B.3.1. DOPPLER INTERFERENCE

In this section, the influence of the Doppler shifts on the orthogonality of the codes will be analysed and the energy loss of the main lobe is presented.

According to the signa model (B.11), the maximum unambiguous velocity is determined by the pulse repetition interval (PRI) T as $v_{\max} = \dfrac{c}{4Tf_c}$. Assume a point-like target with velocity $|v| \leq v_{\max}$, the Doppler frequency is obtained as

$$f_d(v) = \frac{2v}{c} f_c = \frac{v}{v_{\max}} \frac{2v_{\max}}{c} f_c = \frac{1}{2T} \frac{v}{v_{\max}}.$$

According to (B.11), the phase variation remaining in the fast-time will be

$$\varphi = -2\pi f_d(v) k T_c = -\frac{v}{v_{\max}} \frac{kT_c}{T} \pi. \tag{B.12}$$

Since $\left|\dfrac{v}{v_{\max}}\right| \leq 1$ and $\dfrac{kT_c}{T} = \dfrac{k}{K} \leq 1$, we get $|\varphi| \leq \pi$. Let $\nu = \dfrac{v}{2v_{\max}}$, and we have the coherent intergration energy of the target as

$$\begin{aligned} E(\nu) &= \left| \text{corr} \left[\phi^p_{k-n},\ \phi^p_{k-n} \exp\left(-j2\pi\nu \frac{k}{K}\right) \right] \right| \\ &= \left| \sum_{k=0}^{K-1} \exp\left(-j2\pi\nu \frac{k}{K}\right) \right| \\ &= \begin{cases} K & \nu = 0, \\ \dfrac{K}{2\pi|\nu|} \sqrt{2 - 2\cos(2\pi\nu)} & 0 < |\nu| \leq 0.5. \end{cases} \end{aligned} \tag{B.13}$$

Because:

if $\nu = 0$, $\left| \sum_{k=0}^{K-1} \exp\left(-j2\pi\nu \frac{k}{K}\right) \right| = K$;

else if $|\nu| \leq 0.5$,

$$\begin{aligned}
&\left|\sum_{k=0}^{K-1} \exp\left(-j2\pi\nu\frac{k}{K}\right)\right| \\
&\quad= \left|\sum_{k=0}^{K-1}\left[-j\sin\left(2\pi\nu\frac{k}{K}\right)+\cos\left(2\pi\nu\frac{k}{K}\right)\right]\right| \\
&\quad= \left|-j\sum_{k=0}^{K-1}\sin\left(2\pi\nu\frac{k}{K}\right)+\sum_{k=0}^{K-1}\cos\left(2\pi\nu\frac{k}{K}\right)\right| \\
&\quad\xrightarrow{\text{K is sufficiently large}} \\
&\quad\approx \frac{K}{2\pi|\nu|}\left|-j\int_0^{2\pi\nu}\sin x dx+\int_0^{2\pi\nu}\cos x dx\right| \\
&\quad= \frac{K}{2\pi|\nu|}\sqrt{2-2\cos(2\pi\nu)}.
\end{aligned} \tag{B.14}$$

Accordingly, the main lobe energy E of the correlation result for $|\nu| \leq 0.5$ corresponding to the target has

$$\frac{2K}{\pi} = E(0.5) \leq E(\nu) \leq E(0) = K, \tag{B.15}$$

or in dB level

$$\text{dB}(\frac{2K}{\pi}) = \text{dB}(K) - 1.961\ \text{dB} \leq \text{dB}(E(\nu)) \leq \text{dB}(K). \tag{B.16}$$

According to (B.16), the energy of the main lobe of the correlation results does not depend on the code family and the code length but the ratio of $\frac{v}{v_{\max}}$. Furthermore, regardless of the code family and code length, the maximum peak energy loss for a single target is 1.961 dB, which is achieved when $|v| = v_{\max}$. It is indicated in (B.13) that the main lobe energy loss can be calculated according to the value ν, which determines how much improvement can be achieved by Doppler shifts correction.

At the same time, the sidelobe level variation is much more complicated and depends on the code family and code length. The simulation results of the maximum sidelobes energy variation of different code family and length are shown in Fig. B.1, where ZCZ2048, APAS1020, Rand1024, and Rand2048 denote the zero correlation zone (ZCZ) code with the length of 2048, almost perfect autocorrelation sequences (APAS) code with the length of 1020, random code with length 1024 and 2048, respectively.

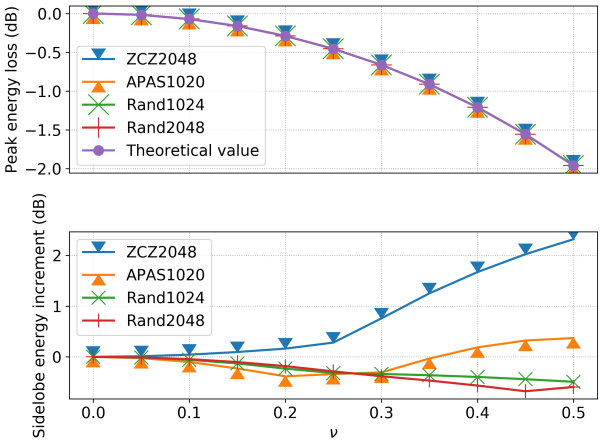

Figure B.1: Energy variation of different codes

B.3.2. LIMITED BANDWIDTH

In addition to the Doppler shifts, removing frequency components by low-pass filter also brings some side effects on the autocorrelation performance of the phase-coded waveforms.

In [120], antenna power transmission limits have been set up by the federal communications commission (FCC) for the United States of America to prevent out-of-band interference and avoid the spectrum from becoming too crowded. The European telecommunications standards institute (ETSI) spectral mask is considered in this appendix, which is for mid-range radar (MRR) and long-range radar (LRR) systems defined by 3 dBm/MHz within the system defined receiver bandwidth B, while outside the receiver bandwidth power spectral density is limited to -30 dBm/MHz.

Since the filter is applied to PMCW waveform in the waveform generator digitally, the perfect rectangular windowing function is performed to simulate the influence of the limited bandwidth. Here the 50 MHz ZCZ code vector $\boldsymbol{\phi}$ with a length of $K = 32768$ is used to simulate the performance and the data are sampled with 400 MHz sampling frequency to observe the main lobe of autocorrelation clearly. Therefore, the real number code is set as $\boldsymbol{\phi} \otimes \mathbf{1}_{16}$, where the vector $\mathbf{1}_{16} = [1, 1, ..., 1] \in \mathbb{R}^{16}$. The spectrum of the codes is plotted in Fig. B.2(a) and two rectangular filters are shown in green line for 100 MHz and red line for 50MHz.

The autocorrelation results are presented in Fig. B.2(b), and the main lobe region is zoomed and shown in Fig. B.2(c), where for better visualization the results are normalised with the 400 MHz data. Although the sidelobe energy for the mid-range of the zero correlation zone is increased when the low-pass filter is applied,

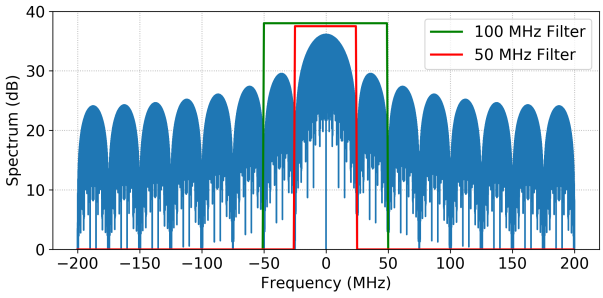

(a)

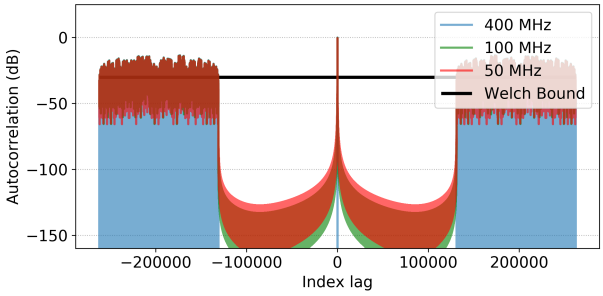

(b)

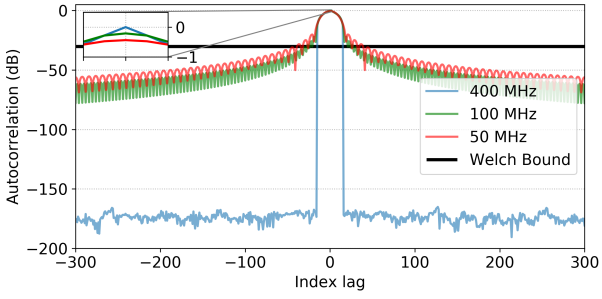

(c)

Figure B.2: Limit bandwidth influence: (a) rectangular filters, (b) autocorrelation results and (c) main lobes and nearby sidelobes

the level is around 100 dB lower than the main lobe and 70 dB lower than Welch bound. Therefore, the long-range sidelobe can be ignored for the low-pass filter. However, the short-range sidelobes shown in Fig. B.2(c) are much stronger when low-pass filter applied. The first sidelobe level for 100 MHz filter is 21.83 dB lower than the main lobe, while that for 50 MHz the sidelobe level is only 19.74 dB lower.

B.4. DOPPLER SHIFTS COMPENSATION

In this section, the Doppler shifts compensation method is presented. There are two ways to perform the Doppler correction, i.e., the direct matched filter suggested in [118] where the replica of the desired signal with Doppler offset for each Doppler channel is applied to the matched filter, and the Doppler compensation for all Doppler channels before the matched filter. The latter will be described in following, while the comparison with the former will be presented at the end of this section. The traditional approach to locate the targets in the range-Doppler domain is applying correlation on the fast-time domain for range profile at first, and then performing FFT on the slow-time domain for Doppler profile. However, without knowing the Doppler information, the term $\exp(-j2\pi f_d(v_i)kT_c)$ cannot be removed for multiple targets. The proposed solution is that the FFT is performed on the slow-time domain firstly to distribute the signals into different Doppler channels as

$$\begin{aligned}\mathcal{X}(k,\xi) &= \sum_{m=0}^{M-1} X(k,m)\exp(-j2\pi\frac{\xi}{M}m)\\ &= \sum_{i=1}^{I}\Big\{\sum_{m=0}^{M-1}\exp\left(j2\pi\frac{-f_d(v_i)MT-\xi}{M}m\right)\\ &\qquad\times\alpha_i\exp\left(-j2\pi f_d(v_i)kT_c\right)\times\sum_{p=0}^{P-1}\phi_{k-n_i}^{p}\Big\}\\ &= \sum_{i=1}^{I}\Big\{\alpha_i\text{sinc}(f_d(v_i)MT+\xi)\\ &\qquad\times\exp(-j2\pi f_d(v_i)kT_c)\times\sum_{p=0}^{P-1}\phi_{k-n_i}^{p}\Big\},\end{aligned} \tag{B.17}$$

where the constant term is absorbed into α_i. Here, usually, windowing function, such as Hann, needs to be applied to suppress the sidelobes, while we neglect this in our formulas to make neat formulas . From Eq. (B.17), in the frequency distribution of the slow-time domain, the peaks appear at the Doppler channel where

$$\hat{\xi}_i = -f_d(v_i)MT. \tag{B.18}$$

The integrated energy in the slow-time domain usually may not be sufficient for target detection. Therefore, we perform the phase compensation blindly for all Doppler frequency channels. For each Doppler frequency channel $\hat{\xi}$, the compensation term is formulated as

$$c(k,\hat{\xi}) = \exp\left(-j2\pi\frac{\hat{\xi}T_c k}{MT}\right). \tag{B.19}$$

Now it is possible to adjust the phase in the fast-time domain for the $\hat{\xi}$th Doppler channel as

$$\begin{aligned}\mathcal{Y}(k,\hat{\xi}) &= \mathcal{X}(k,\hat{\xi}) \times c(k,\hat{\xi}) \\ &= \sum_{i=1}^{I}\Big\{\alpha_i \text{sinc}(f_d(v_i)MT+\hat{\xi})\sum_{p=0}^{P-1}\phi^p_{k-n_i}\Big\}.\end{aligned} \tag{B.20}$$

Although the noise term is not shown here, we note that the compensation is just a phase shift, it will not affect the noise level. Since the phase is adjusted, the correlation process with qth code and with the chip shift $\hat{k}$ is performed to extract the range profile. According to properties in Eq. (B.2), we obtain the results as

$$\begin{aligned}\mathcal{P}(n,\hat{\xi}) &= \text{corr}\left[\mathcal{Y}(k,\hat{\xi}),\ \phi^q_{k-n}\right] \\ &= \sum_{i=1}^{I}\Big[\alpha_i \text{sinc}(f_d(v_i)MT+\hat{\xi})\delta(k-n_i)\Big]\end{aligned} \tag{B.21}$$

Observe the Eq. (B.21), the peaks appear when $f_d(v_i)T = -\dfrac{\hat{\xi}}{M}$ and $k = n_i$. Then the range and Doppler information can be extracted simultaneously.

In fact, since the compensation for each slow-time is fixed, the compensation matrix with entries as (B.19) can be formulated and pre-stored according to the data size to save time.

Compared to the direct matched filter, the correlation patterns of the codes are preserved using Doppler compensation since the additional Doppler shifts on the codes are non-linear operation (element-wise product). Fig. B.3 shows the numerical result of the autocorrelation patterns with the codes from the previous section using the direct matched filter and Doppler compensation, respectively. It is observed that the autocorrelation pattern of ZCZ code is perfectly preserved while direct matched filter introduce high-level sidelobes close to the main lobe.

B.5. EXPERIMENTAL RESUTLS

In this section, the experimental setup is described and the radar system parameters are provided. Due to the hardware limitation, here the single-input and single-

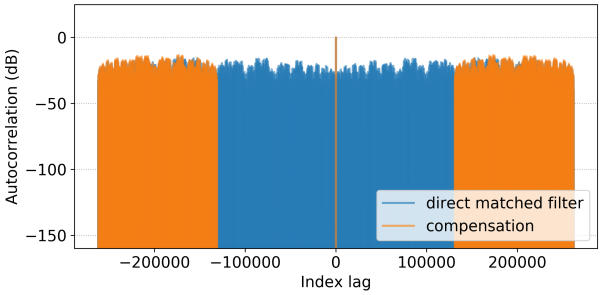

Figure B.3: Comparison between Doppler compensation and direct matched filter

output (SISO) system is used to analyse the correlation properties of the PMCW signal.

B.5.1. PARSAX RADAR

The PARSAX radar on the roof of EWI building is used to observe the vehicles on the Schoenmakerstraat in Delft [121]. The radar working bandwidth is $B = 50$ MHz with the carrier frequency of $f_c = 3.315$ GHz and the sampling frequency is synchronised with the arbitrary waveform generator (AWG). The AWG is applied to generate the PMCW signals with the intermediate frequency of $f_i = 125$ MHz for the real part of data and the sampling clock is $f_s = 400$ MHz.

According to the parameters of the hardware and since only real part of the signal is recorded, the binary chip duration is given as $T_c = \frac{2}{B} = 40$ ns. It means that each binary chip has to digitally repeat $\lfloor T_c f_s \rceil = 16$ times.

The real part of the data is recorded for both transmitted and received waveform by the radar. The PARSAX has four polarization channels, namely HH, HV, VH and VV channels. In the measurements, the VV channel transmits PMCW waveform while the HH channel transmits the reference waveform. The reference waveform has the same PRI with a single pulse at the beginning of PRI so it can be used to label the starting position of the continuous waves.

B.5.2. PMCW SIGNAL

In the experiment, the ZCZ is applied to generate the PMCW signals [122] since it has almost perfect autocorrelation property in the short-range in Fig. B.2(b).

Since the ZCZ code length should be the power of 2, the code length is set to $K = 2^{15} \times 16 = 524288$. Therefore, we obtain the PRI $T = \frac{K}{f_s} = 1.311$ ms and the maximum unambiguous velocity is $v_{\max} = 17.245$ m/s. It is sufficient to observe the vehicles on Schoenmakerstraat whose speed limit is 50 km/h and the

velocity component in the direction to the Radar is even less.

The code series is generated by the Python script and mixed with the intermediate frequency for one PRI waveform. Then the real part of the waveform in intermediate frequency is imported to the AWG.

B.5.3. DATA COLLECTION

According to the setup of the measurement, the procedure is shown as the flowchart in Fig. B.4.

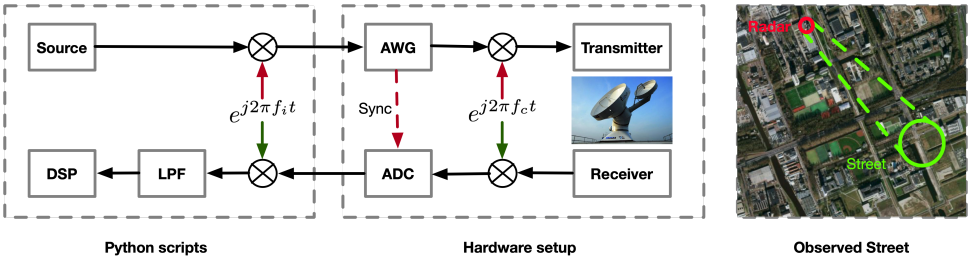

Figure B.4: Flowchart of the measurement

The waveform in intermediate frequency is mixed with the carrier frequency and transmitted by the PARSAX direction to the Schoemarkerstraat. The received analogue data by PARSAX are then mixed with the conjugate of the carrier wave. Then the real part of the discretized data in the intermediate frequency is recorded from sampling on the analogue data with the AWG clock.

To obtain the I/Q channel data and remove the intermediate wave, the spectrum of the received signal is shifted by mixing the conjugate of the intermediate wave and the 100 MHz rectangular windowing function is applied to filter out high-frequency components as Fig. B.5. Then the inverse-FFT (iFFT) is applied to recover the data to the time domain. According to the clock and PRI, the received data are split into fast-time and slow-time domain and ready to be processed.

B.5.4. RESULTS ANALYSIS

In this subsection, the data are processed with the conventional method and the proposed compensation method.

The conventional method applies the code correlation for each fast-time to extract the range information first, and then the Doppler frequency is obtained by performing FFT on the slow-time. The proposed algorithm performs FFT on the slow-time first and formulates the compensation matrix with the entries as (B.19) to remove the Doppler shift residual in each Doppler channel, then applies the fast-time code correlation.

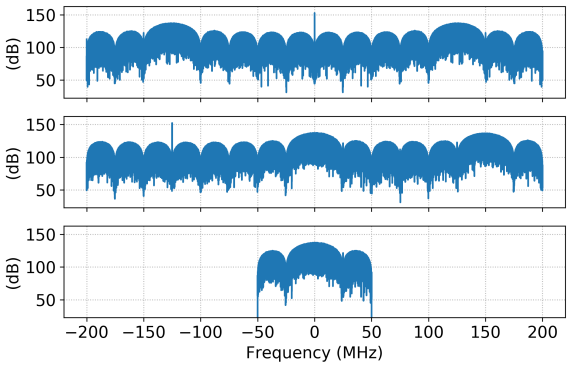

Figure B.5: Spectrum of original data (top), after mixing with intermediate wave (middle), after the low-pass filter (bottom)

Table B.1: Main lobe energies

Target	Target1	Target2
v	-15.65 m/s	14.28 m/s
$\|\nu\|$	0.454	0.414
Theoritical increment	1.59 dB	1.30 dB
Experimental increment	1.94 dB	1.15 dB
Differece	-0.35 dB	0.15 dB

The processing results are shown in Fig. B.6, where the fast-time correlations are performed with the transmitted code itself as autocorrelation and with the orthogonal code as cross-correlation.

Two moving targets are observed at range around 0.9 km with opposite moving directions from the range-Doppler map. The main lobe energies are summarised as Table B.1, where the theoretical values are calculated according to (B.13). The differences between theoretical values and experimental values are -0.35 dB and 0.15 dB, respectively, which are acceptable due to the influences of the noises and clutters.

The sidelobes appearing beyond the range of the targets are much stronger than that appearing before the targets. This is probably due to strong clutters received from the environment at the time after the wavefront hits the ground. Therefore, the sidelobes before the targets (shown in the red boxes) are used to analyse the performance of the compensation method. It is seen in both autocorrelation and cross-correlation results, the sidelobes levels are much lower with the proposed compensation method and almost close to the noise level.

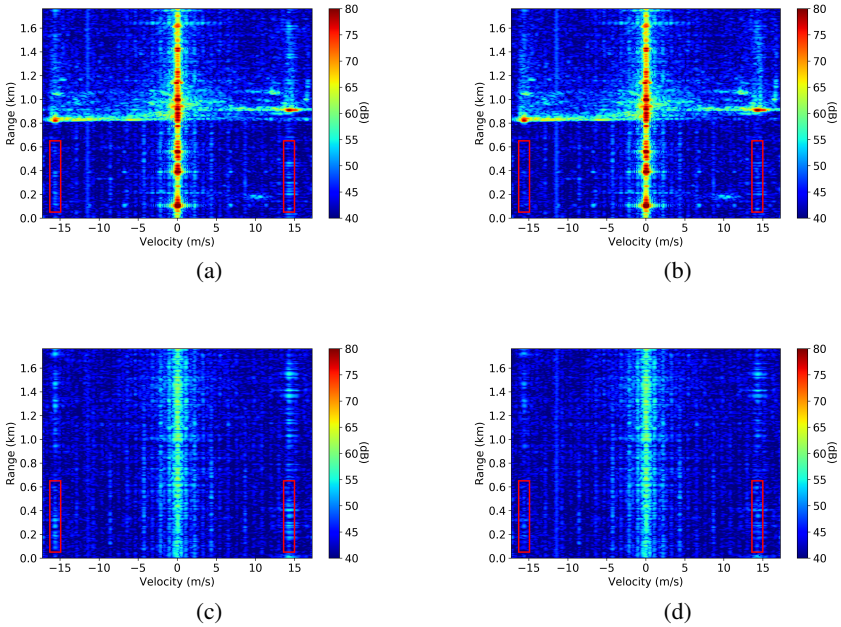

Figure B.6: Range-Doppler map of (a) contiontional autocorrelation, (b) compensational autocorrelation, (c) conventional cross-correlation and (d) compensated cross-correlation

To observe the main lobe enhancement and sidelobe suppression clearly, the sliced range-Doppler maps for the first target at the velocity of -15.65 m/s are plotted in Fig. B.7. For both autocorrelation and cross-correlation, it is seen that the sidelobe suppression is up to 5 dB and most of the sidelobes are suppressed to the noise level.

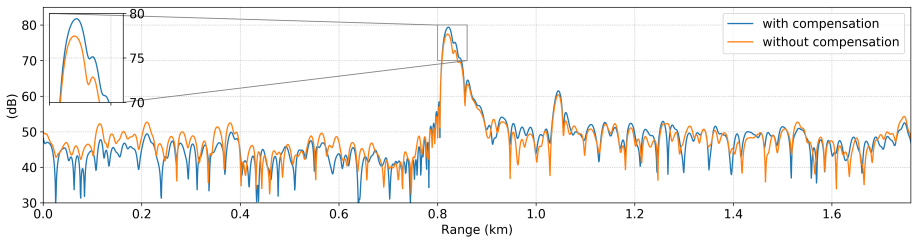

(a)

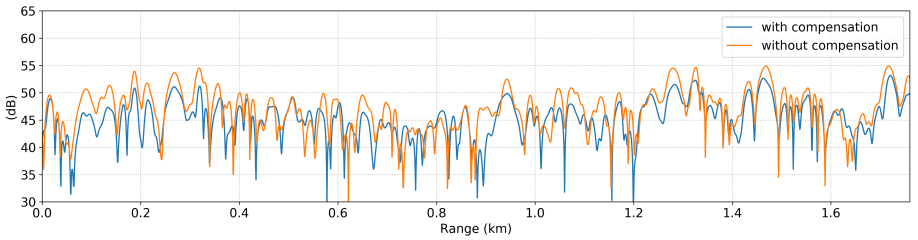

(b)

Figure B.7: Range-Doppler map slicings at $v = -15.65$ m/s of (a) autocorrelation and (b) cross-correlation.

The time consumption for proposed Doppler compensation method, however, is around 50 seconds with one-time zero-padding for FFT on the slow-time, while the computational cost for the conventional method on the same computer is only 12 seconds. When we remove such zero-padding, the time consumptions for the proposed method and the conventional method are 20 seconds and 10 seconds, respectively. Moreover, if the compensation matrix is pre-stored, the time consumption of the Doppler compensation method will be more comparable to the conventional method.

B.5.5. DISCUSSION

The computational complexity of the compensation method is relatively higher than the conventional algorithm. If there are no zero-padding for FFT on slow-time, one extra matrix multiplication is needed for Doppler compensation and the time is usually negligible. However, when n times zero-paddings are applied for FFT on

the slow-time, the time consumption for the fast-time correlation is also n times.

One of the main disadvantages of PMCW compared to FMCW is that the full bandwidth sampling frequency is required for the code recovery while much lower sampling frequency for FMCW is sufficient after deramping. However, PMCW signal needs much less sampling dynamic range than FMCW, even 1-bit sampling is applicable, which, in another way, reduces the hardware requirement [118, 123].

B.6. CONCLUSION

Doppler shift influence on bi-phase PMCW waveform is investigated in this appendix. The signal of the staggered PMCW signal model is established with the fast-time and the slow-time domains. Then the influence of the Doppler shifts and the limited bandwidth on the main lobe and sidelobes are analysed for a single moving target, where the Doppler shift influence on the main lobe can be expressed as a function of the velocity. Moreover, a Doppler shift compensation method is introduced to mitigate the Doppler shift on the fast-time. Last, the measurements using the waveform agile radar PARSAX are performed to validate the performance of PMCW with and without the proposed compensation method. The main lobe enhancement is achieved according to the analysis and the sidelobes level is suppressed up to 5 dB with Doppler shift compensation method proposed.

BIBLIOGRAPHY

[1] V. Winkler, "Range Doppler detection for automotive FMCW radars," in *Microwave Conference, 2007. European*, Oct 2007, pp. 1445–1448.

[2] N. Jiang, R. Wu, and J. Li, "Super resolution feature extraction of moving targets," *IEEE Transactions on Aerospace and Electronic Systems*, vol. 37, no. 3, pp. 781–793, Jul 2001.

[3] B. Xerri, J.-F. Cavassilas, and B. Borloz, "Passive tracking in underwater acoustic," *Signal processing*, vol. 82, no. 8, pp. 1067–1085, 2002.

[4] S. Liu, Z. Zeng, Y. D. Zhang, T. Fan, T. Shan, and R. Tao, "Automatic human fall detection in fractional Fourier domain for assisted living," in *2016 IEEE International Conference on Acoustics, Speech and Signal Processing (ICASSP)*. IEEE, 2016, pp. 799–803.

[5] K. Yamaguchi, M. Saito, K. Miyasaka, and H. Matsue, "Design and performance of a 24 GHz band FMCW radar system and its application," in *2014 IEEE Asia Pacific Conference on Wireless and Mobile*, Aug 2014, pp. 226–231.

[6] F. Belfiori, W. van Rossum, and P. Hoogeboom, "Application of 2D MUSIC algorithm to range-azimuth FMCW radar data," in *Radar Conference (EuRAD), 2012 9th European*, Oct 2012, pp. 242–245.

[7] M. D. Zoltowski and K. T. Wong, "ESPRIT-based 2-D direction finding with a sparse uniform array of electromagnetic vector sensors," *Signal Processing, IEEE Transactions on*, vol. 48, no. 8, pp. 2195–2204, 2000.

[8] H. Al-Tous, I. Barhumi, and N. Al-Dhahir, "Atomic-norm for joint data recovery and narrow-band interference mitigation in OFDM systems," in *2016 IEEE 27th Annual International Symposium on Personal, Indoor, and Mobile Radio Communications (PIMRC)*, Sept 2016, pp. 1–5.

[9] L. Zheng and X. Wang, "Super-resolution delay-Doppler estimation for OFDM passive radar," *IEEE Transactions on Signal Processing*, vol. 65, no. 9, pp. 2197–2210, May 2017.

[10] J. Yu, J. Xu, Y. N. Peng, and X. G. Xia, "Radon-Fourier transform for radar target detection (iii): Optimality and fast implementations," *IEEE Transactions on Aerospace and Electronic Systems*, vol. 48, no. 2, pp. 991–1004, APRIL 2012.

[11] F. Roos, D. Ellenrieder, N. Appenrodt, J. Dickmann, and C. Waldschmidt, "Range migration compensation for chirp-sequence based radar," in *2016 German Microwave Conference (GeMiC)*, March 2016, pp. 317–320.

[12] Z. Sun, X. Li, W. Yi, G. Cui, and L. Kong, "Detection of weak maneuvering target based on Keystone transform and matched filtering process," *Signal Processing*, vol. 140, pp. 127 – 138, 2017. [Online]. Available: http://www.sciencedirect.com/science/article/pii/S0165168417301846

[13] N. Jiang and J. Li, "Multiple moving target feature extraction for airborne HRR radar," *IEEE Transactions on Aerospace and Electronic Systems*, vol. 37, no. 4, pp. 1254–1266, Oct 2001.

[14] J. Li, G. Liu, N. Jiang, and P. Stoica, "Moving target feature extraction for airborne high-range resolution phased-array radar," *IEEE Transactions on Signal Processing*, vol. 49, no. 2, pp. 277–289, Feb 2001.

[15] W. Roberts, P. Stoica, J. Li, T. Yardibi, and F. A. Sadjadi, "Iterative adaptive approaches to MIMO radar imaging," *IEEE Journal of Selected Topics in Signal Processing*, vol. 4, no. 1, pp. 5–20, Feb 2010.

[16] N. Petrov and F. L. Chevalier, "Iterative adaptive approach for unambiguous wideband radar target detection," in *Radar Conference (EuRAD), 2015 European*, Sept 2015, pp. 45–48.

[17] ——, "Fast implementation of iterative adaptive approach for wideband unambiguous radar detection," in *Signal Processing Conference (EUSIPCO), 2015 23rd European*, Aug 2015, pp. 1207–1211.

[18] T. Shan, S. Liu, Y. D. Zhang, M. G. Amin, R. Tao, and Y. Feng, "Efficient architecture and hardware implementation of coherent integration processor for digital video broadcast-based passive bistatic radar," *IET Radar, Sonar & Navigation*, vol. 10, no. 1, pp. 97–106, 2016.

[19] J. Xu, J. Yu, Y. N. Peng, and X. G. Xia, "Radon-Fourier transform for radar target detection (ii): Blind speed sidelobe suppression," *IEEE Transactions on Aerospace and Electronic Systems*, vol. 47, no. 4, pp. 2473–2489, OCTOBER 2011.

[20] I. Shapir, I. Bilik, and G. Barkan, "Doppler ambiguity resolving in TDMA automotive MIMO radar via digital multiple PRF," in *2018 IEEE Radar Conference (RadarConf18)*. IEEE, 2018, pp. 0175–0180.

[21] H. Rohling and M.-M. Meinecke, "Waveform design principles for automotive radar systems," in *Radar, 2001 CIE International Conference on, Proceedings*, vol. 4, 2001, p. 1.

[22] S. Bidon, J.-Y. Tourneret, L. Savy, and F. Le Chevalier, "Bayesian sparse estimation of migrating targets for wideband radar," *IEEE Transactions on Aerospace and Electronic Systems*, vol. 50, no. 2, pp. 871–886, 2014.

[23] S. Bidon, O. Besson, J. Y. Tourneret, and F. L. Chevalier, "Bayesian sparse estimation of migrating targets in autoregressive noise for wideband radar," in *2014 IEEE Radar Conference*, May 2014, pp. 0579–0584.

[24] S. Bidon, A. Tamalet, and J. Y. Tourneret, "Variational bayesian inference for sparse representation of migrating targets in wideband radar," in *2013 IEEE Radar Conference (RadarCon13)*, April 2013, pp. 1–5.

[25] B. D. Carlson, E. D. Evans, and S. L. Wilson, "Search radar detection and track with the Hough transform. i. system concept," *IEEE Transactions on Aerospace and Electronic Systems*, vol. 30, no. 1, pp. 102–108, Jan 1994.

[26] F. Deudon, S. Bidon, O. Besson, and J.-Y. Tourneret, "Velocity dealiased spectral estimators of range migrating targets using a single low-PRF wideband waveform," *IEEE Transactions on Aerospace and Electronic Systems*, vol. 49, no. 1, pp. 244–265, 2013.

[27] X. Li, G. Cui, W. Yi, and L. Kong, "Sequence-reversing transform-based coherent integration for high-speed target detection," *IEEE Transactions on Aerospace and Electronic Systems*, vol. 53, no. 3, pp. 1573–1580, June 2017.

[28] X. Li, G. Cui, W. Yi, and L. Kong, "Radar maneuvering target detection and motion parameter estimation based on TRT-SGRFT," *Signal Processing*, vol. 133, pp. 107–116, 2017.

[29] J. Zheng, T. Su, W. Zhu, X. He, and Q. H. Liu, "Radar high-speed target detection based on the scaled inverse Fourier transform," *IEEE Journal of Selected Topics in Applied Earth Observations and Remote Sensing*, vol. 8, no. 3, pp. 1108–1119, March 2015.

[30] Z. Sun, X. Li, W. Yi, G. Cui, and L. Kong, "A coherent detection and velocity estimation algorithm for the high-speed target based on the modified location

rotation transform," *IEEE Journal of Selected Topics in Applied Earth Observations and Remote Sensing*, vol. 11, no. 7, pp. 2346–2361, July 2018.

[31] Z. Dai, X. Zhang, H. Fang, and Y. Bai, "High accuracy velocity measurement based on Keystone transform using entropy minimization," *Chinese Journal of Electronics*, vol. 25, no. 4, pp. 774–778, 2016.

[32] Z. Sun, X. Li, W. Yi, G. Cui, and L. Kong, "Detection of weak maneuvering target based on KT-MFP," in *2017 IEEE Radar Conference (RadarConf)*. IEEE, 2017, pp. 1488–1492.

[33] J. Zheng, T. Su, H. Liu, G. Liao, Z. Liu, and Q. H. Liu, "Radar high-speed target detection based on the frequency-domain deramp-Keystone transform," *IEEE Journal of Selected Topics in Applied Earth Observations and Remote Sensing*, vol. 9, no. 1, pp. 285–294, Jan 2016.

[34] J. Xu, X.-G. Xia, S.-B. Peng, J. Yu, Y.-N. Peng, and L.-C. Qian, "Radar maneuvering target motion estimation based on generalized Radon-Fourier transform," *IEEE Transactions on Signal Processing*, vol. 60, no. 12, pp. 6190–6201, 2012.

[35] J. Xu, L. Yan, X. Zhou, T. Long, X. Xia, Y. Wang, and A. Farina, "Adaptive radon–Fourier transform for weak radar target detection," *IEEE Transactions on Aerospace and Electronic Systems*, vol. 54, no. 4, pp. 1641–1663, Aug 2018.

[36] D. Xiao, F. Su, and J. Wu, "Multi-target ISAR imaging based on image segmentation and short-time Fourier transform," in *2012 5th International Congress on Image and Signal Processing*, Oct 2012, pp. 1832–1836.

[37] C. Ozdemir, *Inverse synthetic aperture radar imaging with MATLAB algorithms*. John Wiley & Sons, 2012, vol. 210.

[38] T. Itoh, H. Sueda, and Y. Watanabe, "Motion compensation for ISAR via centroid tracking," *IEEE Transactions on Aerospace and Electronic Systems*, vol. 32, no. 3, pp. 1191–1197, 1996.

[39] L. Xi, L. Guosui, and J. Ni, "Autofocusing of ISAR images based on entropy minimization," *IEEE Transactions on Aerospace and Electronic Systems*, vol. 35, no. 4, pp. 1240–1252, 1999.

[40] D. E. Wahl, P. Eichel, D. Ghiglia, and C. Jakowatz, "Phase gradient autofocus-a robust tool for high resolution SAR phase correction," *IEEE*

Transactions on Aerospace and Electronic Systems, vol. 30, no. 3, pp. 827–835, 1994.

[41] M. Martorella, F. Berizzi, and B. Haywood, "Contrast maximisation based technique for 2-D ISAR autofocusing," *IEE Proceedings-Radar, Sonar and Navigation*, vol. 152, no. 4, pp. 253–262, 2005.

[42] J. Munoz-Ferreras, F. Perez-Martinez, and M. Datcu, "Generalisation of inverse synthetic aperture radar autofocusing methods based on the minimisation of the Rényi entropy," *IET radar, sonar & navigation*, vol. 4, no. 4, pp. 586–594, 2010.

[43] M.-S. Kang, J.-H. Bae, S.-H. Lee, and K.-T. Kim, "Efficient ISAR autofocus via minimization of Tsallis entropy," *IEEE Transactions on Aerospace and Electronic Systems*, vol. 52, no. 6, pp. 2950–2960, 2016.

[44] J. Wang, X. Liu, and Z. Zhou, "Minimum-entropy phase adjustment for ISAR," *IEE Proceedings-Radar, Sonar and Navigation*, vol. 151, no. 4, pp. 203–209, 2004.

[45] S. Zhang, Y. Liu, and X. Li, "Fast entropy minimization based autofocusing technique for ISAR imaging," *IEEE Transactions on Signal Processing*, vol. 63, no. 13, pp. 3425–3434, 2015.

[46] X. Bai, F. Zhou, M. Xing, and Z. Bao, "A novel method for imaging of group targets moving in a formation," *IEEE Transactions on Geoscience and Remote Sensing*, vol. 50, no. 1, pp. 221–231, 2011.

[47] D. Xiao, F. Su, and J. Wu, "Multi-target ISAR imaging based on image segmentation and short-time Fourier transform," in *2012 5th international congress on image and signal processing*. IEEE, 2012, pp. 1832–1836.

[48] X. Dong, Y. Zhang, X. Gu, and W. Zhai, "ISAR imaging of multiple targets based on sparse representations," in *2015 IEEE International Conference on Microwaves, Communications, Antennas and Electronic Systems (COMCAS)*. IEEE, 2015, pp. 1–4.

[49] A. Wang, Y. Mao, and Z. Chen, "Imaging of multitargets with ISAR based on the time-frequency distribution," in *Proceedings of ICASSP'94. IEEE International Conference on Acoustics, Speech and Signal Processing*. IEEE, 1994, pp. V–173.

[50] FanLuhong, P. Yiming, and H. Shunji, "Multi-target imaging processing algorithms of ISAR based on time-frequency analysis," in *2006 CIE International Conference on Radar*, Oct 2006, pp. 1–4.

[51] J. Zhao, Y.-Q. Zhang, X. Wang, S. Wang, and F. Shang, "A novel method for isar imaging of multiple maneuvering targets," *Progress In Electromagnetics Research*, vol. 81, pp. 43–54, 2019.

[52] Y. Li, Y. Fu, X. Li, and L.-W. Li, "An isar imaging method for multiple moving targets based on fractional Fourier transformation," in *2009 IEEE Radar Conference*. IEEE, 2009, pp. 1–6.

[53] J. Zhao, M. Zhang, X. Wang, and D. Nie, "Parameters estimation and ISAR imaging of multiple maneuvering targets based on an order reduction method for cubic chirps," *Journal of ElEctromagnEtic WavEs and applications*, vol. 31, no. 16, pp. 1658–1675, 2017.

[54] X. Fu and M. Gao, "ISAR imaging for multiple targets based on randomized Hough transform," in *2008 Congress on Image and Signal Processing*, vol. 5. IEEE, 2008, pp. 238–241.

[55] K. Yamamoto, M. Iwamoto, T. Fujisaka, and T. Kirimoto, "An ISAR imaging algorithm for multiple targets of different radial velocity," *Electronics and Communications in Japan (Part I: Communications)*, vol. 86, no. 7, pp. 1–10, 2003.

[56] L. Liu, F. Zhou, M. Tao, and Z. Zhang, "A novel method for multi-targets ISAR imaging based on particle swarm optimization and modified CLEAN technique," *IEEE Sensors Journal*, vol. 16, no. 1, pp. 97–108, 2015.

[57] E. Giusti and M. Martorella, "Range Doppler and image autofocusing for FMCW inverse synthetic aperture radar," *IEEE Transactions on Aerospace and Electronic Systems*, vol. 47, no. 4, pp. 2807–2823, 2011.

[58] J. Zhao, M. Zhang, and X. Wang, "ISAR imaging algorithm of multiple targets with complex motions based on the fractional tap length Keystone transform," *IEEE Transactions on Aerospace and Electronic Systems*, vol. 54, no. 1, pp. 64–76, 2017.

[59] D. Zoeke and A. Ziroff, "Phase migration effects in moving target localization using switched MIMO arrays," in *2015 European Radar Conference (EuRAD)*, Sep. 2015, pp. 85–88.

[60] H. Wang and M. Kaveh, "Coherent signal-subspace processing for the detection and estimation of angles of arrival of multiple wide-band sources," *IEEE Transactions on Acoustics, Speech, and Signal Processing*, vol. 33, no. 4, pp. 823–831, August 1985.

[61] H. Hung and M. Kaveh, "Focussing matrices for coherent signal-subspace processing," *IEEE Transactions on Acoustics, Speech, and Signal Processing*, vol. 36, no. 8, pp. 1272–1281, Aug 1988.

[62] A. Belouchrani and M. G. Amin, "Time-frequency MUSIC," *IEEE Signal Processing Letters*, vol. 6, no. 5, pp. 109–110, 1999.

[63] Y. Zhang and M. G. Amin, "Blind separation of nonstationary sources based on spatial time-frequency distributions," *EURASIP Journal on Applied Signal Processing*, vol. 2006, pp. 198–198, 2006.

[64] A. B. Gershman and M. G. Amin, "Wideband direction-of-arrival estimation of multiple chirp signals using spatial time-frequency distributions," *IEEE Signal processing letters*, vol. 7, no. 6, pp. 152–155, 2000.

[65] M. A. Richards, J. Scheer, W. A. Holm, and W. L. Melvin, *Principles of modern radar*. Citeseer, 2010.

[66] D. Oh and J. H. Lee, "Low-complexity range-azimuth FMCW radar sensor using joint angle and delay estimation without SVD and EVD," *IEEE Sensors Journal*, vol. 15, no. 9, pp. 4799–4811, Sept 2015.

[67] S. Kim, D. Oh, and J. Lee, "Joint DFT-ESPRIT estimation for TOA and DOA in vehicle FMCW radars," *IEEE Antennas and Wireless Propagation Letters*, vol. 14, pp. 1710–1713, 2015.

[68] S. Hong, X. Wan, and H. Ke, "Spatial difference smoothing for coherent sources location in MIMO radar," *Signal Processing*, vol. 109, pp. 69 – 83, 2015. [Online]. Available: http://www.sciencedirect.com/science/article/pii/S0165168414004642

[69] M. Haardt, F. Roemer, and G. Del Galdo, "Higher-order SVD-based subspace estimation to improve the parameter estimation accuracy in multidimensional harmonic retrieval problems," *IEEE Transactions on Signal Processing*, vol. 56, no. 7, pp. 3198–3213, 2008.

[70] M. A. Richards, "The Keystone transformation for correcting range migration in range-doppler processing," *pulse*, vol. 1000, p. 1, 2014.

[71] Y. Saad, *Iterative methods for sparse linear systems*. siam, 2003, vol. 82.

[72] B. N. Parlett, *The symmetric eigenvalue problem*. SIAM, 1998.

[73] M. Steiner and K. Gerlach, "Fast converging adaptive processor or a structured covariance matrix," *IEEE Transactions on Aerospace and Electronic Systems*, vol. 36, no. 4, pp. 1115–1126, Oct 2000.

[74] C. L. Liu and P. P. Vaidyanathan, "Tensor music in multidimensional sparse arrays," in *2015 49th Asilomar Conference on Signals, Systems and Computers*, Nov 2015, pp. 1783–1787.

[75] N. Vervliet, O. Debals, and L. D. Lathauwer, "Tensorlab 3.0 — numerical optimization strategies for large-scale constrained and coupled matrix/tensor factorization," in *2016 50th Asilomar Conference on Signals, Systems and Computers*, Nov 2016, pp. 1733–1738.

[76] R. A. Horn, R. A. Horn, and C. R. Johnson, *Matrix analysis*. Cambridge university press, 1990.

[77] S. Xu, B. J. Kooij, and A. Yarovoy, "Joint Doppler and DOA estimation using (ultra-)wideband FMCW signals," *Signal Processing*, p. 107259, 2019. [Online]. Available: http://www.sciencedirect.com/science/article/pii/S0165168419303111

[78] T. G. Kolda and B. W. Bader, "Tensor decompositions and applications," *SIAM review*, vol. 51, no. 3, pp. 455–500, 2009.

[79] J. A. Nelder and R. Mead, "A simplex method for function minimization," *The computer journal*, vol. 7, no. 4, pp. 308–313, 1965.

[80] and, "Implementation of the RELAX algorithm," *IEEE Transactions on Aerospace and Electronic Systems*, vol. 34, no. 2, pp. 657–664, April 1998.

[81] Y. Jiao, J. Yu, and R. Che, "Application of RELAX algorithm to ISAR superresolution imaging," in *2006 CIE International Conference on Radar*, Oct 2006, pp. 1–4.

[82] Jian Li, P. Stoica, and Dumin Zheng, "Angle and waveform estimation in the presence of colored noise via RELAX," in *Conference Record of The Twenty-Ninth Asilomar Conference on Signals, Systems and Computers*, vol. 1, Oct 1995, pp. 433–437 vol.1.

[83] S. Lin, Y. Rong, X. Sun, and Z. Xu, "Learning capability of relaxed greedy algorithms," *IEEE transactions on neural networks and learning systems*, vol. 24, no. 10, pp. 1598–1608, Oct 2013.

[84] Y. Zhang, "Super-resolution passive ISAR imaging via the RELAX algorithm," in *2016 9th International Symposium on Computational Intelligence and Design (ISCID)*, vol. 2, Dec 2016, pp. 65–68.

[85] G. H. Golub and C. F. Van Loan, *Matrix computations*. JHU press, 2012, vol. 3.

[86] Y. Li, Y. Fu, X. Li, and L. Le-Wei, "ISAR imaging of multiple targets using particle swarm optimisation–adaptive joint time frequency approach," *IET signal processing*, vol. 4, no. 4, pp. 343–351, 2010.

[87] A. Chambolle, "An algorithm for total variation minimization and applications," *Journal of Mathematical imaging and vision*, vol. 20, no. 1-2, pp. 89–97, 2004.

[88] I. Shapir, I. Bilik, and G. Barkan, "Doppler ambiguity resolving in TDMA automotive MIMO radar via digital multiple PRF," in *2018 IEEE Radar Conference (RadarConf18)*, April 2018, pp. 0175–0180.

[89] M. Klotz and H. Rohling, "24 GHz radar sensors for automotive applications," in *13th International Conference on Microwaves, Radar and Wireless Communications. MIKON-2000. Conference Proceedings (IEEE Cat. No. 00EX428)*, vol. 1. IEEE, 2000, pp. 359–362.

[90] D. M. Grimes and T. O. Jones, "Automotive radar: A brief review," *Proceedings of the IEEE*, vol. 62, no. 6, pp. 804–822, 1974.

[91] J. Hasch, E. Topak, R. Schnabel, T. Zwick, R. Weigel, and C. Waldschmidt, "Millimeter-wave technology for automotive radar sensors in the 77 GHz frequency band," *IEEE Transactions on Microwave Theory and Techniques*, vol. 60, no. 3, pp. 845–860, 2012.

[92] M. Schneider, "Automotive radar-status and trends," in *German microwave conference*, 2005, pp. 144–147.

[93] H. Shinoda, T. Nagasaku, and H. Kondoh, "Automotive radar," Nov. 7 2006, uS Patent 7,132,976.

[94] S. T. Nicolson, K. H. Yau, S. Pruvost, V. Danelon, P. Chevalier, P. Garcia, A. Chantre, B. Sautreuil, and S. P. Voinigescu, "A low-voltage SiGe BiCMOS 77-GHz automotive radar chipset," *IEEE Transactions on Microwave Theory and Techniques*, vol. 56, no. 5, pp. 1092–1104, 2008.

[95] W. Menzel and A. Moebius, "Antenna concepts for millimeter-wave automotive radar sensors," *Proceedings of the IEEE*, vol. 100, no. 7, pp. 2372–2379, 2012.

[96] S. Xu and A. Yarovoy, "Joint Doppler and DOA estimation using 2D MUSIC in presence of phase residual," in *2017 European Radar Conference (EURAD)*, Oct 2017, pp. 203–206.

[97] Y. Gürcan and A. Yarovoy, "Super-resolution algorithm for joint range-azimuth-Doppler estimation in automotive radars," in *2017 European Radar Conference (EURAD)*, Oct 2017, pp. 73–76.

[98] Nxp homepage. [Online]. Available: https://www.nxp.com/

[99] T.-J. Shan, M. Wax, and T. Kailath, "On spatial smoothing for direction-of-arrival estimation of coherent signals," *IEEE Transactions on Acoustics, Speech, and Signal Processing*, vol. 33, no. 4, pp. 806–811, 1985.

[100] F. Belfiori, W. van Rossum, and P. Hoogeboom, "2D-MUSIC technique applied to a coherent FMCW MIMO radar," in *IET International Conference on Radar Systems (Radar 2012)*, Oct 2012, pp. 1–6.

[101] P. Stoica and R. L. Moses, *Spectral analysis of signals*. Pearson/Prentice Hall Upper Saddle River, NJ, 2005.

[102] S. Xu, J. Wang, and A. Yarovoy, "Super resolution DOA for FMCW automotive radar imaging," in *2018 IEEE Conference on Antenna Measurements Applications (CAMA)*, Sep. 2018, pp. 1–4.

[103] J. Overdevest, F. Jansen, F. Uysal, and A. Yarovoy, "Doppler influence on waveform orthogonality in 79 GHz MIMO phase-coded automotive radar," *IEEE Transactions on Vehicular Technology*, vol. 69, no. 1, pp. 16–25, Jan 2020.

[104] A. Bourdoux, U. Ahmad, D. Guermandi, S. Brebels, A. Dewilde, and W. Van Thillo, "PMCW waveform and MIMO technique for a 79 GHz CMOS automotive radar," *2016 IEEE Radar Conference, RadarConf 2016*, pp. 1–5, 2016.

[105] A. M. D. Turkmani and U. S. Goni, "Performance evaluation of maximal-length, gold and kasami codes as spreading sequences in CDMA systems," in *Proceedings of 2nd IEEE International Conference on Universal Personal Communications*, vol. 2, 1993, pp. 970–974 vol.2.

[106] M. Golay, "Complementary series," *IRE Transactions on Information Theory*, vol. 7, no. 2, pp. 82–87, 1961.

[107] H. Haderer, R. Feger, and A. Stelzer, "A comparison of phase-coded CW radar modulation schemes for integrated radar sensors," in *2014 44th European Microwave Conference*. IEEE, 2014, pp. 1896–1899.

[108] K. R. Griep, J. A. Ritcey, and J. J. Burlingame, "Poly-phase codes and optimal filters for multiple user ranging," *IEEE Transactions on Aerospace and Electronic Systems*, vol. 31, no. 2, pp. 752–767, 1995.

[109] S. W. Golomb, "Two-valued sequences with perfect periodic autocorrelation," *IEEE Transactions on Aerospace and Electronic Systems*, vol. 28, no. 2, pp. 383–386, 1992.

[110] K. R. Griep, J. A. Ritcey, and J. J. Burlingame, "Poly-phase codes and optimal filters for multiple user ranging," *IEEE Transactions on Aerospace and Electronic Systems*, vol. 31, no. 2, pp. 752–767, 1995.

[111] L. Welch, "Lower bounds on the maximum cross correlation of signals (corresp.)," *IEEE Transactions on Information theory*, vol. 20, no. 3, pp. 397–399, 1974.

[112] T. J. Riedl and A. C. Singer, "Broadband Doppler compensation: Principles and new results," in *2011 Conference Record of the Forty Fifth Asilomar Conference on Signals, Systems and Computers (ASILOMAR)*. IEEE, 2011, pp. 944–946.

[113] Z. Matousek, J. Ochodnicky, M. Babjak, and J. Puttera, "Doppler compensation for binary phase-coded radar signals in presence of noise jamming," in *2016 17th International Radar Symposium (IRS)*. IEEE, 2016, pp. 1–4.

[114] R. Frank, "Polyphase complementary codes," *IEEE Transactions on Information theory*, vol. 26, no. 6, pp. 641–647, 1980.

[115] ——, "Polyphase codes with good nonperiodic correlation properties," *IEEE Transactions on Information Theory*, vol. 9, no. 1, pp. 43–45, 1963.

[116] M. S. Rashed, M. Meijer, and P. D. Teal, "Mismatched filtering of Doppler tolerant codes for multi-code sonar systems," in *OCEANS 2019 MTS/IEEE SEATTLE*, 2019, pp. 1–10.

[117] M. H. Ackroyd and F. Ghani, "Optimum mismatched filters for sidelobe suppression," *IEEE Transactions on Aerospace and Electronic Systems*, no. 2, pp. 214–218, 1973.

[118] M. I. Skolnik, "Radar handbook second edition," *McGrawHill*, 1990.

[119] C. F. le, *Principles of radar and sonar signal processing*. Artech House, 2002.

[120] FCC, "FCC FACT SHEET radar services in the 76-81 GHz band." [Online]. Available: https://docs.fcc.gov/public/attachments/DOC-348982A1.pdf

[121] Z. Wang, O. A. Krasnov, L. P. Ligthart, and F. van der Zwan, "FPGA based IF digital receiver for the PARSAX - polarimetric agile radar," in *18-th INTERNATIONAL CONFERENCE ON MICROWAVES, RADAR AND WIRELESS COMMUNICATIONS*, June 2010, pp. 1–4.

[122] X. H. Tang, P. Z. Fan, and S. Matsufuji, "Lower bounds on correlation of spreading sequence set with low or zero correlation zone," *Electronics Letters*, vol. 36, no. 6, pp. 551–552, March 2000.

[123] W. Van Thillo, V. Giannini, D. Guermandi, S. Brebels, and A. Bourdoux, "Impact of ADC clipping and quantization on phase-modulated 79 GHz CMOS radar," in *2014 11th European Radar Conference*, 2014, pp. 285–288.

List of Acronyms

ADC	analog-to-digital convertor
AWG	arbitrary waveform generator
APAS	almost perfect autocorrelation sequences
BF	beamforming
CPI	coherent processing interval
CRB	Cramér-Rao bounds
CRT	Chinese remaider theroem
CSSM	coherent signal subspace method
DAC	digital-analog convertor
DOA	direction-of-arrival
EM	entropy minimisation
ESPRIT	estimation of signal parameters via rotation invariance techniques
ETSI	European telecommunications standards institute
FCC	federal communications commission
FDMA	frequency-division multiple access
FFT	fast Fourier transform
FMCW	frequnecy-modulated continuous-wave
FrFT	fractional Fourier transform
GAIC	generalized Akaike information criterion
GMTI	ground moving target indication
HOSVD	high-order singular value decomposition
HT	Hough transform
IAA	iterative adaptive algorithm
IC	integrated circuit
ISAR	inverse synthetic aperture radar
ISSM	incoherent signal subspace method
LOS	line-of-sight
LRR	long-range radar
EM	entropy minimisation
MF	Mathced filter
MIMO	multiple-input multiple output
MRR	mid-range radar

MUSIC	multiple signal classification
NLS	non-linear least square square
PMCW	phase-modulated continuous wave
PRF	pulse repetition interval
PRI	pulse repetition interval
RMSE	root-mean-square-error
RFT	Radon Fourier transform
RWT	Radon-Wigner transform
SNR	signal-to-noise ratio
STFT	short-time Fourier transform
TD	tensor decomposition
TDMA	time-division multiple access
TOA	time-of-arrival
TF	time-frequency
TV	total variation
ULA	uniformly distributed array
USCM	universal spatial covariance matrix
UWB	ultra-wideband
WVD	Wigner-Ville distribution
ZCZ	zero correlation zone

ACKNOWLEDGEMENTS

After four years of happy PhD life, I saw my development and improvement in many aspects. I gained not only the intensive knowledge and advanced skills, but also cares and friendships from the people I met. Therefore, I would like to express my most sincere gratitude to those who have helped me during my PhD life.

Foremost, I would like to express my highest gratitude to my promotor, Prof. A. Yarovoy. Thank you for offering me an opportunity to study overseas and to be a member of MS3 group. I feel so lucky to have your guidance in my research topics, your efforts and patience in training and developing my soft skills, your support and encouragement in my life. I sincerely thank you for the financial support with which I can participate in many conference and summer school in these years.

It is my great honour to have Prof. A. Stelzer, Prof. D. M. Gavrila, Prof. F.M.J. Willems, Prof. F. le Chevalier and Prof. G.J.T. Leus to be my committee members. Thank you for your time and constructive suggestions to make the thesis better. Special gratitude for Prof. G.J.T. Leus, who gave me a lot of comments and suggestions on my yearly progress meetings.

I would also like to express my appreciations to my current and former colleagues who have made my PhD life enjoyable and unforgettable. I would like to thank Mink van der Put, Minaksie Ramsoekh and Esther. You are so nice and patient. Thank you for helping me with all the administrative problem and for organising so many fun activities. Thank you, Oleg, Faruk, Francesco, Hans, Bert Jan and Xinliang for many excellent suggestions for my work. Thank Nikita and Jianping for your time to read my papers and your advice to improve them. Special thanks to Bert Jan who helps to translate the summary of this thesis. Thank Rossisz, Nannan, Stefano and Jan for bringing me a relaxed and pleasant office atmosphere and I really enjoy the time when we work in the same room. Thank Shilong, Xuan, Zhenhai for sharing the most pleasant holidays on the trips. Thank Ozan, Ronny, Max, Sharef, Yanki, Utku, Yun, Iraklis, Arun for the daily talking and sharing of the different cultures. Thank Fred, Peter, Etienne, Pascal, Dinh and Antoine for helping me arrange and perform the experiments and all the technical supports. I gained so much knowledge from you which are inaccessible from the book. Thank the master students Yefeng, Min, Jiadi, Yuqing, Saravanan, Prithvi, Guigeng, Shheeraz, Ruoyu, Yalin, Jeroen. I really miss the prime time when we have fun together.

Next, I would like to convey my thanks to my domestic supervisor, Prof. Yi and Prof. Huang for your supports and cares.

I would also like to show my appreciations to my current and former flatmates. Thank Yutian, Yudong, Yinzheng, Xiang, Yue, Tiantian, Jian, Jianping, Peng, Zhoujiang for your company and patience. I really enjoy the time preparing the dinner with you.

Then I would like to show my gratitude to my dear friends in the Netherlands and in China. Renfei, Guanliang, Ding, Han, Jitang, Ling, Yande, Ruxin, Da, Lingling, Yunlong, Haoyuan, Qiang, Yiting, Jing, Jiefang, Sihang, Yajie, Huan, Li, Xiaohui, Liangfu, Yu, Jiapeng, Jintao, Tingyu, Hong, Weiyuan, Feng, Baozhou, Hongjuan, Xing, Linyu, Min, Guangyu, Chunjiang, Qihua, Jialu, Tianzhu, Xiaoxiang, Tao, Xiaoji, Xinyi, Yangyueye. Special thanks to Tiantian Du, who helps me to design the cover.

My deepest gratitude goes to my family. You give me unconditional love and support me to accomplish my goals. My brother Shengpei, thank you for taking care of our parents when I am not with them.

I am also grateful to China Scholarship Council which provides the fund for my PhD. There are so many people who have helped me during my PhD life, but I cannot list them all. The text is sometimes so pale that I cannot express all my gratitude.

LIST OF PUBLICATIONS

JOUNAL PAPERS

1) S. Xu, B. J. Kooij and A. Yarovoy. "Joint Doppler and DOA estimation using (Ultra-) Wideband FMCW signals," *Signal Processing* 168 (2020): 107259.

2) S. Xu, and A. Yarovoy, "Joint Features Extraction for Multiple Moving Targets Using (Ultra-)Wideband FMCW Signals in presence of Doppler Ambiguity," *IEEE Transactions on Signal Processing*, under review after revision.

3) S. Xu, and A. Yarovoy, "Motion-based Separation and Imaging of Closely-Spaced Extended Targets," *IEEE Sensors Journal*, under review.

4) S. Xu, F. van der Zwan and A. Yaroovy, "Study on Doppler Influence for bi-phase PMCW Signals,", *IEEE Transactions on Microwave Theory and Techniques*, to be submitted.

CONFERENCE PAPERS

1) S. Xu and A. Yarovoy, "Joint Doppler and DOA estimation using 2D MUSIC in presence of phase residual," *2017 European Radar Conference (EURAD)*, Nuremberg, 2017, pp. 203-206.
doi: 10.23919/EURAD.2017.8249182

2) S. Xu, J. Wang and A. Yarovoy, "Super Resolution DOA for FMCW Automotive Radar Imaging," *2018 IEEE Conference on Antenna Measurements & Applications (CAMA)*, Vasteras, 2018, pp. 1-4.
doi: 10.1109/CAMA.2018.8530609

3) S. Xu and A. Yarovoy, "Joint Parameters Estimation Using 3D Tensor MUSIC in the Presence of Phase Residual," *2018 International Conference on Radar (RADAR)*, Brisbane, QLD, 2018, pp. 1-4.
doi: 10.1109/RADAR.2018.8557322

4) S. Xu, and A. Yarovoy, "Doppler Shifts Mitigation for PMCW Signals," *2019 International Conference on Radar (RADAR)*, Toulon, 2019, pp. 1-4.

CURRICULUM VITÆ

Shengzhi XU

22-03-1991 Born in Hefei, China.

EDUCATION

2009-2013 Undergraduate, School of Electronic and Optical Engineering
Nanjing University of Science and Technology, Nanjing, China

2013-2015 Graduate, Department of Electronic Science and Engineering
National University of Defence Technology, Changsha, China

2015-2020 PhD, MS3
Delft University of Technology, Delft, the Netherlands